




Universitetet
i Stavanger

FACULTY OF SCIENCE AND TECHNOLOGY

MASTER'S THESIS

Study programme/specialisation: Engineering Structures and Materials - Machine constructions	Spring semester, 2018 Open
Author: Ninni Sofie Brun	 (signature of author)
Programme coordinator: Professor Dimitrios G. Pavlou Supervisor: Christoffer Lie Syversen	
Title of master's thesis: Preliminary design of a fuel cell - battery hybrid propulsion system for a small VTOL UAV	
Credits: 30	
Keywords: <i>Fuel Cells</i> <i>UAV</i> <i>VTOL</i> <i>Hybridization</i> <i>Hydrogen storage</i> <i>Composite pressure vessel</i> <i>Aerial propulsion system</i> <i>Long endurance</i>	Number of pages: 81 + supplemental material/other: 30 Stavanger, 14.06.2018

ABSTRACT

Over the past decade, utilization of unmanned aerial vehicles (UAVs) in military and commercial applications has increased significantly. The vertical take-off and landing (VTOL) UAV is appreciated for its easy launch and versatile operation capability, but the missions are limited due to low endurance. Hybrid fuel cell systems have the potential to increase the endurance significantly. Until now, the use of fuel cell systems in VTOL UAVs have been limited to demonstrations, but as new and lightweight fuel cell systems have been developed, the technology seems to have reached the maturity level needed to realize fuel cell powered VTOL UAVs for more widespread use. This paper considers the implementation of a hybrid fuel cell – battery system on an existing VTOL UAV with maximum take-off weight (MTOW) of 25 kg. The available technology for fuel cells and hydrogen storage are investigated with the aim of determining the best solution for this UAV, and a preliminary design of the entire propulsion system is done. The selection of different components is based on power estimation from momentum theory. The hydrogen storage is a customized spherical composite pressure vessel. A comparison between cylindrical and spherical pressure vessels are performed to justify the use of a spherical pressure vessel. The calculations are based on classical lamination theory. The results indicate that a spherical pressure vessel gives weight savings of 15 %. The estimated endurance of the proposed system is 3.2 hours at MTOW with a custom spherical pressure of 21 liters. This is a 7-fold improvement compared to the current installed batteries.

PREFACE

This thesis completes my Master of Science education in Engineering Structures and Materials with specialization in Mechanical systems at the University of Stavanger. The work has been done in collaboration with Nordic Unmanned, a local company which specialize in unmanned systems.

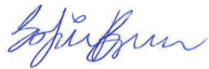
The last six months have been challenging, instructive and entertaining. The task has let me use knowledge across many subjects from the education. I will like to thank Knut Roar Wiig CEO at Nordic Unmanned for the opportunity, and the rest of the crew for support, interesting discussions and inputs.

A special thanks to my supervisor, Professor Dimitrios G. Pavlou, for expert assistance in composite materials, and for pointing me in right direction at dead ends.

At last I will thank my children and family for bringing joy into my life.

To the reader; I hope you find this thesis interesting and useful.

Ninni Sofie Brun



Stavanger, June 14, 2018

LIST OF ABBREVIATIONS

BOP	Balance of plant
CFD	Computational fluid dynamics
CLT	Classical lamination theory
COPV	Composite overwrapped pressure vessel
COTS	Commercial of the shelf
COV	Coefficient of variance
DC	Direct current
DMFC	Direct methanol fuel cell
ESC	Electric speed controllers
FAA	Federal Aviation Administration
HDPE	High density polyethylene
HHV	Higher heating value
LH ₂	Liquid hydrogen
LHV	Lower heating value
LIDAR	Light detection and ranging
LiPo	Lithium Polymer
MEA	Membrane electrode assembly
MTOW	Maximum take-off weight
PEMFC	Polymer electrolyte membrane fuel cell
RANS	Reynolds-Avaraged Navier-Stokes
RPA	Remotely piloted aircraft
SOFC	Solid-oxide fuel cell
UAS	Unmanned aerial system
UAV	Unmanned aerial vehicle
VTOL	Vertical take-off and landing

LIST OF SYMBOLS

A_{cell}	Cell active area
C_d	Drag coefficient
E^0	Reversible voltage
I_{dis}	Discharge current
K_v	Motor voltage constant
P_0	Profile power
P_{climb}	Power consumption in climb
P_{cruise}	Power consumption in forward flight
$P_{i,hover}$	Induced power in hover
$P_{i,coaxial}$	Induced power with coaxial configuration
P_i	Induced power
P_{ideal}	Ideal power
P_p	Parasitic power
R_i	Internal resistance
V_0	Induced velocity in hover
V_2	Velocity far downstream
V_c	Climb velocity
V_{cell}	Cell voltage
V_{dis}	Discharge voltage
V_i	Induced velocity
V_{mot}	Motor voltage
V_{oc}	Open circuit voltage
V_{st}	Stack voltage
W_{elec}	Useful work
k_{int}	Interference induced power factor
\dot{m}	Mass flow
rpm_{mot}	Rotation per minute of motor shaft
v_{fuel}	Supplied fuel
ϵ_{fuel}	Fuel utilization efficiency
ϵ_{thermo}	Thermodynamic efficiency
$\epsilon_{voltage}$	Voltage efficiency

Δg	Gibbs free energy
Δh	Enthalpy of reaction
A	Area
D	Drag force
E	Voltage/Modulus of elasticity
F	Faradays constant
FM	Figure of merit
I	Current
P	Power
Q	Charge
R	Universal gas constant/Radius
S	Reference area
T	Thrust/Temperature
U	Resultant velocity
V	Relative velocity/Volume
Z	Compressibility factor
f	Equivalent flat plate area
i	Current density
n	Number of moles
p	Pressure
ρ	Air density
$[\bar{Q}]$	Reduced transformed stiffness matrix
$[C]$	Lamina stiffness matrix
G_{ij}	Shear modulus
$M_{composite}$	Weight of composite overwrap
M_{liner}	Weight of liner
$[S]$	Lamina compliance matrix
$[T]$	Transformation matrix
$V_{composite}$	Volume of composite overwrap
V_{liner}	Volume of liner
p_{burst}	Burst pressure
p_{design}	Design pressure
γ	Shear strain

ε^o	Midplane strains
ν_{ij}	Poisson's ratio
ρ_{HDPE}	Density of HDPE liner
$\rho_{carbon/epoxy}$	Density of carbon/epoxy material
σ^C	Compressive strength
σ^T	Tensile strength
τ	Shear stress
τ^F	Shear strength
$[Q_{ij}]$	Reduced stiffness matrix
[A]	Extensional stiffness matrix
[B]	Coupling stiffness matrix
[D]	Bending stiffness matrix
L	Length
M	Moment per unit length
N	Force per unit length
t	Thickness
u	Deformation in x-direction
v	Deformation in y-direction
ε	Strain
κ	Curvature
σ	Stress

LIST OF FIGURES

FIGURE 2-1: FLOW THROUGH A ROTOR DISC IN HOVER [7] .	5
FIGURE 2-2: FLOW THROUGH A ROTOR DISC IN VERTICAL CLIMB [7].	6
FIGURE 2-3: FLOW MODEL FOR MOMENTUM ANALYSIS OF A ROTOR DISC IN FORWARD FLIGHT [9].	7
FIGURE 2-4: VELOCITY COMPONENTS.	8
FIGURE 2-5: PREDICTIONS OF THE MAIN ROTOR POWER OF A HELICOPTER IN FORWARD FLIGHT [9].	9
FIGURE 2-6: ROTOR DISCS IN COAXIAL CONFIGURATION.	10
FIGURE 2-7: SHOWS THE DISCHARGE CURVE FOR AN IDEAL SECONDARY BATTERY AND TWO CURVES (CURVE 1 AND CURVE 2) FOR AN ACTUAL SECONDARY BATTERY [14].	12
FIGURE 3-1: A BASIC FUEL CELL [17].	13
FIGURE 3-2: PLANAR STRUCTURE OF A FUEL CELL.	14
FIGURE 3-3: COMBINED CURRENT-VOLTAGE DIAGRAM(I-V CURVE) AND POWER DENSITY CURVE. MODIFIED FROM REF. [17].	16
FIGURE 3-4: MEMBRANE ELECTRODE ASSEMBLY OF PEMFC [17].	18
FIGURE 3-5: DIFFERENT FACTORS THAT INFLUENCE FUEL CELL EFFICIENCY [26].	20
FIGURE 3-6: COMPRESSIBILITY FACTOR FOR HYDROGEN AT DIFFERENT PRESSURES AND TEMPERATURES [35].	23
FIGURE 3-7: COMPRESSION WORK AND COMPRESSION ENERGY AS PERCENTAGE OF LHV FOR ADIABATIC, MULTISTAGE AND ISOTHERMAL PROCESSES. THE PROCESS INVOLVES PRESSURIZING HYDROGEN FROM 1 BAR UP TO REQUIRED PRESSURE [36].	24
FIGURE 3-8: CONVENTIONAL HYBRID SYSTEM [39].	24
FIGURE 4-1: REPRESENTATION OF THE DIFFERENT TYPES OF PRESSURE VESSELS [33].	25
FIGURE 4-2: SHOWS THE NORMALIZED COST VERSUS WEIGHT FOR THE DIFFERENT TYPES OF PRESSURE VESSELS [40].	25
FIGURE 4-3: REQUIREMENTS FOR CONSTRUCTION OF A PRESSURE VESSEL [41].	26
FIGURE 4-4: A THIN-WALLED SPHERICAL PRESSURE VESSEL (LEFT) Σ AND CROSS-SECTIONAL VIEW(RIGHT).	27
FIGURE 4-5: FREE BODY DIAGRAM OF A SPHERICAL PRESSURE VESSEL.	27
FIGURE 4-6: FREE BODY DIAGRAM OF A CYLINDRICAL PRESSURE VESSEL IN LONGITUDINAL DIRECTION.	28
FIGURE 4-7: FREE BODY DIAGRAM OF A CYLINDRICAL PRESSURE VESSEL IN CIRCUMFERENTIAL DIRECTION.	28
FIGURE 4-8: UNIDIRECTIONAL LAMINA WITH PRINCIPAL (123) AND GLOBAL (XYZ) COORDINATE SYSTEMS [43].	30
FIGURE 4-9: 3D-STATE OF STRESS.	30
FIGURE 4-10: DEFORMATION OF A LAMINATED PLATE IN THE X-Z PLANE	33
FIGURE 4-11: NUMBERING SYSTEM USED IN ANALYSIS OF LAMINATE [43].	34
FIGURE 4-12: APPLIED FORCES AND MOMENTS PER UNIT METER IN GLOBAL COORDINATE SYSTEM [43].	36
FIGURE 5-1: CAMFLIGHT FX8HL MULTIROTOR UAV.	42
FIGURE 5-2: CONCEPT TREE OF PROPULSION SYSTEM.	44
FIGURE 5-3: MISSION PROFILE.	45
FIGURE 5-4: MOTOR PERFORMANCE - THRUST VS. POWER.	46
FIGURE 5-5: THRUST VS. THROTTLE.	47
FIGURE 5-6: THEORETICAL POWER AS A FUNCTION OF DIAMETER AT MTOW OF 25 KG.	48
FIGURE 5-7: THRUST OUTPUT VS. POWER INPUT FOR THE KDE 7215 MOTOR.	49
FIGURE 5-8: POWER REQUIRED IN CLIMB AS A FUNCTION OF CLIMB SPEED.	49
FIGURE 5-9: SIMPLIFIED MODEL OF THE UAV USED AS A BASIS FOR ESTIMATION OF DRAG COEFFICIENT, THE DIFFERENT COMPONENTS ARE TO SCALE.	50
FIGURE 5-10: FORCES ACTING ON A ROTOR DISC IN FORWARD FLIGHT.	51
FIGURE 5-11: POWER CONSUMPTION AS A FUNCTION OF FORWARD SPEED	51
FIGURE 5-12: TYPICAL I-V CURVE FOR A PEMFC [18].	53
FIGURE 6-1: GEOMETRY OF SPHERICAL PRESSURE VESSEL.	59
FIGURE 6-2: SHOWS THE TSAI-WU FAILURE CRITERION VALUE FOR DIFFERENT PLY ORIENTATIONS FOR SPHERICAL PRESSURE VESSEL, AND HENCE THE OPTIMUM WINDING ANGLE.	60
FIGURE 6-3: TWO UNIDIRECTIONAL LAYERS WITH 90 DEGREES RELATIVE ROTATION MAKE UP A CROSS-PLY LAYER.	60
FIGURE 6-4: GEOMETRY OF CYLINDRICAL PRESSURE VESSEL.	61
FIGURE 6-5: SHOWS THE TSAI-WU FAILURE CRITERION VALUE FOR DIFFERENT PLY ORIENTATIONS FOR A CYLINDRICAL PRESSURE VESSEL, AND HENCE THE OPTIMUM WINDING ANGLE.	62
FIGURE 6-6: TOTAL WEIGHT OF SPHERICAL AND CYLINDRICAL PRESSURE VESSELS OF DIFFERENT INTERNAL VOLUMES.	63

FIGURE 6-7: RATIO R BETWEEN THE WEIGHT OF CYLINDRICAL AND SPHERICAL PRESSURE VESSELS FOR DIFFERENT INTERNAL VOLUMES	63
FIGURE 6-8: WEIGHT OF SPHERICAL PRESSURE VESSEL FOR DIFFERENT VOLUMES.	66
FIGURE 6-9: FORCE PER UNIT METER ACTING ON AN ELEMENT.	67
FIGURE 7-1: BLOCK DIAGRAM OF THE PROPULSION SYSTEM.....	70
FIGURE 7-2: ESTIMATED ENDURANCE FOR DIFFERENT PAYLOADS.	72
FIGURE 7-3: ESTIMATED ENDURANCE FOR PRESSURE VESSELS OF VARYING SIZE.	72

LIST OF TABLES

TABLE 2-1: METRICS OF DIFFERENT BATTERY TYPES [5].	11
TABLE 3-1: FUEL CELL TYPES USED IN SMALL UAV APPLICATIONS[16, 19, 21].....	17
TABLE 3-2: PROPERTIES OF PEMFC.	18
TABLE 3-3: COMPARISON OF HYDROGEN STORAGE SYSTEMS. THE MASS AND VOLUME USED IN THESE DATA INCLUDES TANK, VALVES, TUBING AND REGULATORS [17] [26].....	21
TABLE 4-1: CHARACTERISTICS OF TYPE III AND TYPE IV PRESSURE VESSELS [40].....	26
TABLE 4-2: SAFETY FACTORS FOR COPV PRESSURE VESSELS IN DIFFERENT STANDARDS	38
TABLE 4-3: SAFETY FACTORS FOR DIFFERENT VALUES OF COV, WITH AN ANNUAL PROBABILITY OF FAILURE OF 10^{-7}	39
TABLE 5-1: TARGET SPECIFICATIONS.	42
TABLE 5-2: CONCEPT SCORING-MATRIX FOR HYDROGEN STORAGE. THE CRITERIA ARE WEIGHTED WITH RELATIVE IMPORTANCE.....	43
TABLE 5-3: SPECIFICATIONS OF THE CONSIDERED BRUSHLESS DC MOTORS	46
TABLE 5-4: EFFICIENCY IN HOVER AT THRUST OF 3125 G PER MOTOR.	47
TABLE 5-5: SPECIFICATIONS OF KDEXF-UAS95HVC ESC	47
TABLE 5-6: DRAG COEFFICIENTS FOR THE COMPONENTS THAT MAKE UP THE UAV	50
TABLE 5-7: SUMMARY OF POWER REQUIREMENTS ACCORDING TO THE MISSION PROFILE	52
TABLE 5-8: PRELIMINARY FUEL CELL SIZING.	53
TABLE 5-9: FUEL CELL SYSTEMS IN THE 2000 W RANGE	54
TABLE 5-10: SPECIFICATIONS OF MAXAMPS LIPO BATTERY.	56
TABLE 6-1: ELASTIC PROPERTIES OF CARBON/EPOXY COMPOSITE MATERIAL [55].....	58
TABLE 6-2: STRENGTH OF CARBON/EPOXY COMPOSITE MATERIAL [55]	58
TABLE 6-3: PROPERTIES OF HDPE LINER [56]	59
TABLE 6-4: STRENGTH OF A CROSS-PLY LAMINA WITH FIBER VOLUME FRACTION V_f OF 0.6, IN THE GLOBAL COORDINATE SYSTEM.....	61
TABLE 6-5: PROPERTIES OF TWO 9 L COTS CYLINDRICAL PRESSURE VESSELS TOGETHER WITH A 9 L CALCULATED CYLINDRICAL PRESSURE VESSEL.....	64
TABLE 6-6: PROPERTIES OF IM6/3501-6 CARBON/EPOXY LAMINA WITH CARBON FIBER VOLUME FRACTION V_f OF 63.5 % [61]. ...	65
TABLE 6-7: BIAXIAL STRENGTH OF IM6/3501-6 CROSS-PLY LAMINATE [60].....	66
TABLE 6-8: 21 L SPHERICAL PRESSURE VESSEL PARAMETERS.	67
TABLE 6-9: SPHERICAL PRESSURE VESSEL PARAMETERS.....	69
TABLE 7-1: PROPULSION SYSTEM COMPONENTS, SEE THE OTHER TABLES FOR DETAILED INFORMATION.	70
TABLE 7-2: PERFORMANCE OF THE DESIGNED PROPULSION SYSTEM	71

CONTENTS

ABSTRACT	I
PREFACE	V
LIST OF ABBREVIATIONS	VI
LIST OF SYMBOLS	VII
LIST OF FIGURES	X
LIST OF TABLES	XI
1 INTRODUCTION	1
2 THEORY	3
2.1 UNMANNED AERIAL VEHICLES.....	3
2.2 POWER CONSUMPTION – MOMENTUM THEORY.....	4
2.3 BRUSHLESS DC MOTOR.....	11
2.4 BATTERY TECHNOLOGY	11
3 FUEL CELL TECHNOLOGY	13
3.1 THE BASICS	13
3.2 BENEFITS AND LIMITATIONS.....	16
3.3 TYPES OF FUEL CELLS FOR SMALL UAV APPLICATIONS	17
3.4 POLYMER ELECTROLYTE MEMBRANE FUEL CELL (PEMFC)	17
3.5 FUEL CELL STACK SIZING	18
3.6 FUEL CELL COMPONENTS AND DESIGN	19
3.7 HYDROGEN STORAGE SYSTEMS	21
3.8 HYDROGEN SAFETY	22
3.9 COMPRESSION OF HYDROGEN GAS.....	23
3.10 FUEL CELL BATTERY HYBRIDIZATION.....	24
4 COMPOSITE HIGH PRESSURE VESSEL	25
4.1 PRESSURE VESSEL TYPES	25
4.2 SPHERICAL VS. CYLINDRICAL PRESSURE VESSEL	26
4.3 CLASSICAL LAMINATION THEORY	29
4.4 TSAI-WU FAILURE CRITERION	37
4.5 SAFETY FACTOR	38
4.6 FAILURE MECHANISMS	39
4.7 LINER	39
5 FUEL CELL – BATTERY HYBRID SYSTEM COMPONENT SIZING AND SELECTION	41
5.1 EXISTING SYSTEM.....	41
5.2 PROPULSION SYSTEM COMPONENTS	42
5.3 MISSION PROFILE.....	45
5.4 SELECTION OF MOTORS	45
5.5 POWER REQUIREMENT CALCULATIONS.....	48
5.6 PRELIMINARY FUEL CELL SIZING	52
5.7 SELECTION OF COTS FUEL CELL SYSTEM.....	53

5.8	AEROSTAK 2000 DETAILS.....	54
5.9	POWER CONTROL.....	55
5.10	SELECTION OF BATTERY	55
6	HYDROGEN STORAGE ANALYSIS: COMPOSITE PRESSURE VESSELS	57
6.1	SIZING OF HYDROGEN STORAGE	57
6.2	COPV PRESSURE VESSEL DESIGN CONSIDERATIONS	57
6.3	COMPARISON OF SPHERICAL AND CYLINDRICAL PRESSURE VESSEL.....	59
6.4	COMPARISON TO COTS PRESSURE VESSELS	64
6.5	DESIGN OF SPHERICAL PRESSURE VESSEL.....	65
7	RESULTS: SYSTEM PERFORMANCE AND ENDURANCE ESTIMATES.....	70
8	DISCUSSION	73
9	CONCLUSION.....	75
10	REFERENCES.....	77
	APPENDIX.....	81
	APPENDIX A: MATLAB CODES.....	81
	APPENDIX B: LAMINA PROPERTIES AND STRENGTH.....	104
	APPENDIX C: COMPARISON OF SPHERICAL AND CYLINDRICAL PRESSURE VESSELS, RESULTS DATA	108
	APPENDIX D: CONSTANTS USED IN CALCULATIONS.....	109

1 INTRODUCTION

We are said to be in the golden era of unmanned aerial vehicles (UAVs) and over the past decade the application has gone from being almost exclusively military to extensive civil and commercial use. UAVs offers low operating cost, high efficiency and safe operations. Small UAVs with maximum takeoff weight (MTOW) of 25 kg or less dominates the commercial market, with applications such as inspection, terrain mapping, surveying and monitoring. Most small UAVs have electric propulsion with the advantages of high efficiency, little noise and reliable operation. The big limitation is the endurance resulting from the energy source. The current battery technology offers low specific energy, where current lithium polymer batteries have upper limit of about 200 Wh/kg, resulting in a typical endurance of 15-60 min for a vertical take-off and landing (VTOL) UAV.

Over the recent years a growing interest of using fuel cells as energy source for UAVs has emerged. The first implementation was in a military fixed wing UAV. Hydrogen has energy density of 33410 Wh/kg giving a huge potential for improvement of endurance. With current fuel cell and hydrogen storage technology, the endurance of a VTOL UAV will typically increase at least three times compared to batteries. Fuel cells have the same advantages as batteries comprising safe and silent operation, but the system is much more complex and expensive. Fuel cells electrochemically convert the hydrogen fuel and the oxygen in the air into electricity, water and heat. A fuel cell system consists of a number of cells making up the fuel cell stack, working within a balance of plant (BOP) which consists of cooling devices, humidifiers, flow fields and control system.

Many demonstrations of fuel cell systems in fixed wing UAVs have been seen since the first was launched in 2003, and the current world record for endurance is 48 h. Several companies are in the race of developing lightweight and efficient fuel cells and the systems are now beginning to reach the maturity for commercial use. It is first in the last few years we have seen fuel cell systems been implemented to VTOL UAVs. A major challenge is the high and fluctuating power demand. Fuel cells have relatively low specific power and slow response compared to batteries. For VTOL UAV applications, the fuel cell is hybridized with a battery to get the advantages from both systems. The world's first fuel cell driven VTOL UAV was demonstrated by EnergyOr Technologies in 2015, where the multirotor UAV reached a flight time of 2 h and 12 min [1]. Later the same year, HES Energy Systems represented their Hycopter, a multirotor UAV which reached an endurance of 4 h. This was 8-10 times longer than an equivalent system using batteries [2]. In 2016 Micro Multi Copters Aero Technology Co (MMC) launched Hycopter, a fuel cell powered multirotor UAV. The demonstrated flight time was 4 h which was an 8-fold improvement compared to batteries. Special about this system is that it also can operate in low-temperature areas [3]. In 2017 Wirth Research unveiled a tilt-rotor VTOL UAV driven by a fuel cell system provided by HES. This system is intended for varying and heavy payload including infrared sensors and light detection and ranging (LIDAR) imagers, and the goal is to reach 6 h endurance [4].

This paper is focused on the preliminary design of a fuel cell – battery hybrid solution for an existing UAV currently driven by LiPo batteries. The available technology for the fuel cells and hydrogen storage are examined with the goal of finding the most suited technology for this application. Furthermore, the different parts composing the propulsion system are sized and selected from commercial off the shelf (COTS) products. The power demand, which is the basis for sizing of the fuel cell and the battery, is estimated with momentum theory in three flight regimes; hover, climb and forward flight. The hydrogen storage is a custom spherical pressure vessel, designed with aid of classical lamination theory.

The investigated VTOL UAV is the Camflight FX8 with MTOW of 25 kg, which is an octocopter with the propellers arranged in four coaxial pairs. This UAV can operate with a range of payloads, but the calculations are made with the primary mission payload, which is a LIDAR intended for terrain

mapping. The goal is to design a fuel cell – battery hybrid system of maximum 10 kg capable of powering a 3 h flight.

Chapter 2 through 4 contains relevant the background theory needed to do a preliminary design of the propulsion system. The review of fuel cell technology (chapter 3) and the background theory needed to design a composite pressure vessel (chapter 4) are represented in separate chapters, as both constitute a major part of the work. In chapter 5 the selection of the different components composing the propulsion system takes place. The calculations of the composite pressure vessel are represented in chapter 6. The performance and endurance estimates of the proposed system is found in chapter 7, followed by a discussion of the results and a conclusion at the end.

2 THEORY

2.1 UNMANNED AERIAL VEHICLES

An unmanned aerial vehicle (UAV) is defined as a powered vehicle which is not carrying a human operator but are controlled either remotely or autonomously. Several other names are also used instead of UAV, such as unmanned aerial system (UAS), remotely piloted aircraft (RPA) or popularly as drone.

UAVs have many advantages over manned aircrafts, such as the capability to carry out dangerous missions without the risk of human life and the size of the vehicle are usually much smaller compared to manned aircrafts which makes the take-off and landing much easier. The cost and the development time of the aircraft is also significantly reduced with the size. The design of a UAV typically takes 2-4 years versus 10-20 years for a manned aircraft. The operational costs are also usually much lower as the maintenance and fuel consumption are significantly less [5].

These advantages together with the maturing of electronics, GPS and satellite communications technologies through the 1980's and 1990's have led to an explosion of new civil and commercial application areas[5]. The small UAV market still seems to be in an early stage, and Federal Aviation Administration (FAA) forecasts that the commercial small UAV fleet will grow from 42000 units in 2016 to 420000 in 2021[6].

UAVs comes in many forms and shapes dependent on the application area and are often classified by size, range or endurance, or combinations of these. The UAV that is the basis for this thesis is known as a small UAV. Small UAVs are recognized by MTOW of less than 25 kg. Furthermore, there are other categories such as fixed wing and VTOL UAVs. A fixed wing UAV has rigid wings and the shape is usually similar to a conventional airplane. Typically, fixed wing UAVs will have longer endurance and travel at higher speeds than VTOL UAVs. VTOL UAVs are recognized by their rotary wings which enables hovering. These UAVs are often categorized by the number of propellers. Common configurations are tricopter (3 propellers), quadcopter (4 propellers), hexacopter (6 propellers) and octocopter (8 propellers). The multirotor UAVs are easy to fly and maneuver, and are highly versatile as they can take off and land from a single point. The major drawback is the endurance. Typical commercial applications for small UAVs are

- Aerial photography; pictures and movies
- Agriculture; inspection of crops and livestock
- Inspection of high-voltage power transmission lines
- Inspection of gas and oil pipelines
- Delivery of goods and medicines to remote areas
- Search and rescue
- Border patrol
- Coastal surveillance
- Sampling and analysis of atmosphere

2.2 POWER CONSUMPTION – MOMENTUM THEORY

Momentum theory (also called actuator disk theory) is the simplest method to describe a lifting rotor and is based on that a lifting force is generated because of change in momentum. The assumptions for the theory are as follows:

- The fluid is incompressible and inviscid
- The flow remains in the same direction
- Existence of a streamtube which is an axially symmetric surface that isolates the flow through the motor.
- The rotor disc has zero thickness

Figure 2-1 shows the flow through the rotor disc in hover. The flow enters the streamtube, and is accelerated through the rotor disc. The generated thrust is found by change in momentum. The vertical flow velocity far upstream must tend to zero. Since the air is assumed to be incompressible, continuity can be used to establish a relationship between the induced velocity V_i and the velocity increase downstream of the rotor V_2 [7]:

$$\rho AV_i = \rho A_2 V_2 \quad (2.1)$$

where A is the area of the rotor disc, A_2 is the area of the stream tube far downstream and ρ is the air density.

The conservation of momentum gives the rotor thrust T as:

$$T = \rho AV_i V_2 \quad (2.2)$$

The rotor thrust can also be expressed by the difference in air pressure over and under the rotor disk:

$$T = \rho A(p_L - p_U) \quad (2.3)$$

where p_L and p_U is the pressure below and above the rotor disc, respectively. Finally, Bernoulli's equation is used above and below the rotor disc:

$$p_\infty = p_U + \frac{1}{2}\rho V_i^2 \quad (\text{above}) \quad (2.4)$$

$$p_L + \frac{1}{2}\rho V_i^2 = p_\infty + \frac{1}{2}\rho V_2^2 \quad (\text{below}) \quad (2.5)$$

Using equation (2.2) - (2.5) it can be shown that:

$$V_2 = 2V_i \quad (2.6)$$

Now combining equation (2.2) and (2.6) the induced velocity can be expressed as:

$$V_i = \sqrt{\frac{T}{2\rho A}} \quad (2.7)$$

The induced power in hover $P_{i,hover}$ is then given by:

$$P_{i,hover} = T \cdot V_i = \frac{T^{\frac{3}{2}}}{\sqrt{2\rho A}} \quad (2.8)$$

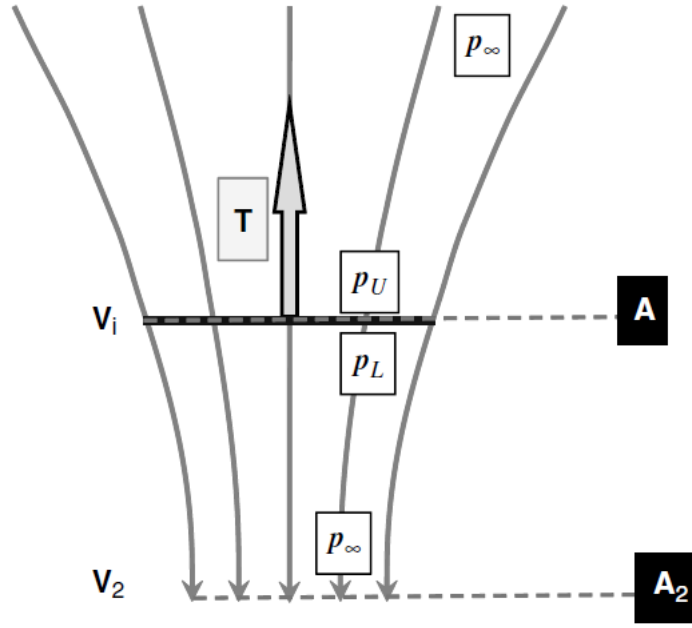


Figure 2-1: Flow through a rotor disc in hover [7].

2.2.1 Power in climb

The same arguments that have been used to calculate the required power in hover, can also be used to calculate the required power in vertical climb. The flow through the rotor in vertical climb is shown in Figure 2-2. The difference between the two cases is that the far upstream velocity does not tend to zero as in hover. The continuity equation gives:

$$\rho A_1 V_c = \rho A (V_c + V_i) = \rho A_2 (V_c + V_2) \quad (2.9)$$

where V_c is the vertical climb velocity of the UAV, V_i is the induced velocity, and V_2 is the velocity far downstream.

The conservation of momentum gives:

$$T = \rho A (V_c + V_i) V_2 \quad (2.10)$$

Applying the Bernoulli's equation on both sides of the rotor disc in Figure 2-2, and combining the results with the above equation, it can be shown that V_2 is twice as large as V_i :

$$V_2 = 2V_i \quad (2.11)$$

Substituting this into equation (2.10), the thrust can be expressed as follows:

$$T = 2\rho A (V_c + V_i) V_i \quad (2.12)$$

The induced velocity in hover for the same thrust is defined as:

$$V_0 = \sqrt{\frac{T}{2\rho A}} \quad (2.13)$$

The induced velocity is always positive for positive thrust, and by substituting (2.13) into (2.12), the solution for the induced velocity in climb is as follows:

$$V_i = -\frac{V_c}{2} + \sqrt{\left(\frac{V_c}{2}\right)^2 + V_0^2} \quad (2.14)$$

The power consumed in climb P_{climb} is given by the product of the thrust and the total velocity through the rotor disc:

$$P_{climb} = T(V_c + V_i) \quad (2.15)$$

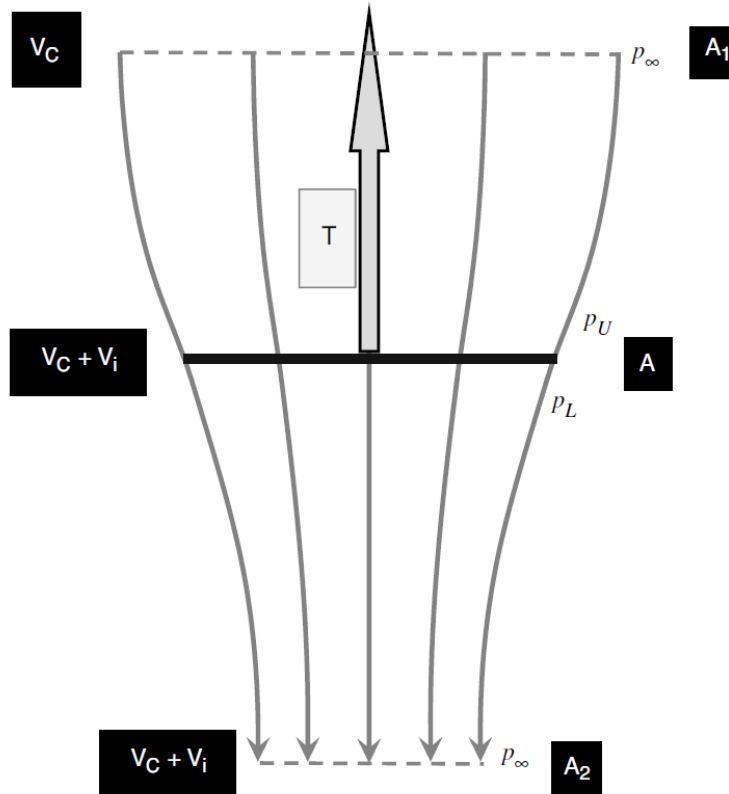


Figure 2-2: Flow through a rotor disc in vertical climb [7].

2.2.2 Performance

The induced power makes up most of the power needed for hovering, but some additional power is required to overcome the aerodynamic drag of the blades, and there are also other losses due to non-uniform flow, swirl in the wake, and tip losses due to the discreteness and periodicity in the wake because the number of blades is finite. Figure of merit is a measure of the rotor hovering efficiency as it compares the actual rotor performance P with the performance of an ideal rotor P_{ideal} :

$$FM = \frac{P_{ideal}}{P} \quad (2.16)$$

where the ideal power is given by equation (2.8). The ideal figure of merit is $FM=1$, but for current well-designed rotors, the maximum figure of merit is typically between $FM=0.74$ to 0.78 [8].

2.2.3 Power in forward flight

The aerodynamics in forward flight is complex, and are normally evaluated by numerical methods. Momentum theory is principally a theory for hover and axial flight, but it is a fast and reasonably accurate method that can be used for power estimates in forward flight for conceptual design. The required power in forward flight is given by:

$$P_{cruise} = P_i + P_0 + P_p + P_{climb}, \quad (2.17)$$

where P_i is the induced power required to produce rotor thrust, P_0 is the profile power required to turn the rotor through the air, P_p is the parasitic power required to move the aircraft through the air, and P_{climb} is the climb power required to change the gravitational energy [9].

In forward flight the rotor needs to provide a lifting force to balance the gravitational pull and a propulsive force to overcome the aerodynamic drag and to move the aircraft forward through the air. Because of these forces, the rotor needs to be tilted forward, and hence the axisymmetry of the flow through the rotor disc is lost. Figure 2-3 shows the forces on a helicopter in forward flight, together with an illustration of the flow model. Note that the figure shows a helicopter that is in a state of both forward flight and climb. To use momentum theory in forward flight, some assumptions are made:

- The streamtube is adopted
- The induced velocity far downstream is two times the induced velocity, as in axial flight
- The induced velocity is normal to the disc plane
- The airflow is horizontal far upstream

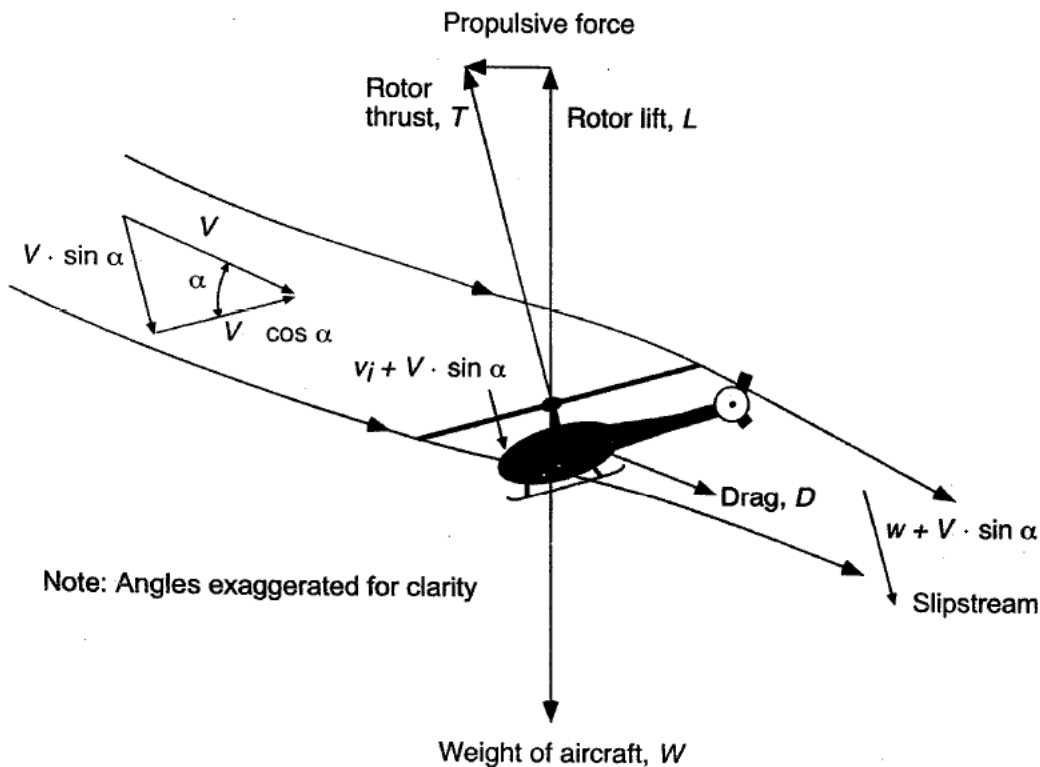


Figure 2-3: Flow model for momentum analysis of a rotor disc in forward flight [9].

Furthermore, the analysis is done with respect to an axis aligned with rotor disc. The mass flow rate through the rotor disc is $\dot{m} = \rho AU$, and momentum conservation gives the rotor thrust T as:

$$T = \dot{m}2V_i = 2\rho AU V_i, \quad (2.18)$$

where U are the resultant velocity through the through the rotor disc, and V_i is the induced velocity. The resultant velocity is found by vectorially adding the induced velocity and the relative velocity V, as shown on Figure 2-4, given by this expression:

$$U^2 = (V\cos\alpha)^2 + (V\sin\alpha + V_i)^2, \quad (2.19)$$

where α is the angle between the relative velocity V and the rotor disc. The relative velocity is the velocity experienced by the propeller caused by the movement through the air, and equals the forward velocity of the UAV.

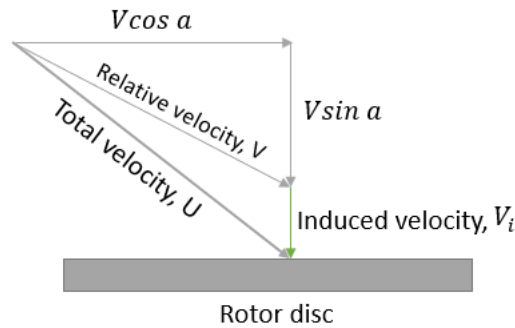


Figure 2-4: Velocity components.

By equation (2.18) and (2.19) the rotor thrust can be expressed as

$$T = 2\rho AV_i \sqrt{V^2 + 2VV_i\sin\alpha + V_i^2} \quad (2.20)$$

The rotor power can be found with energy conservation:

$$P = \rho AU \left(\frac{1}{2} [(V\cos\alpha)^2 + (V\sin\alpha + V_i)^2] - \frac{1}{2} V^2 \right) = T(V\sin\alpha + V_i) \quad (2.21)$$

The term Tv_i is the induced power and $TV\sin\alpha$ is the parasitic power. The expression above is the ideal power needed in forward flight. The induced power decreases with increasing forward speed, and the parasitic power increases until it is dominant at high speeds. The profile power is approximately 10-20 % of the total power and increases slightly with increasing forward speed. Figure 2-5 shows the behavior of the different power components as functions of forward speeds for a helicopter. It shows that there is a minimum power consumption at a certain forward speed.

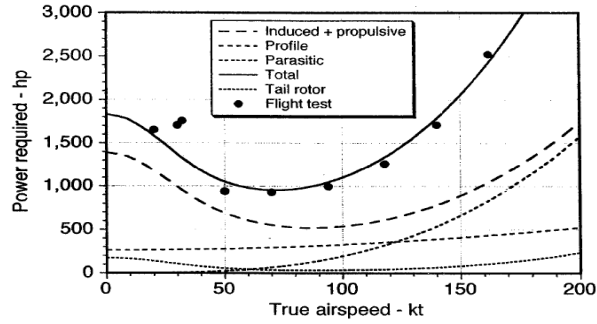


Figure 2-5: Predictions of the main rotor power of a helicopter in forward flight [9].

2.2.4 Coaxial propulsion performance

The UAV considered in this thesis, the Camflight XF8, is actuated by 8 propellers arranged in 4 coaxial pairs. The propellers are rotating in opposite directions to equalize the momentum of the platform. The main advantage with this configuration is increased lift while the volume is kept reasonable. However, coaxial configuration (see Figure 2-6) suffers from lower thrust compared to two isolated propellers due to interference between the two coaxial propellers. The performance of coaxial propulsion can be predicted by momentum theory. The assumptions are that the two rotors operate sufficiently close and that each provides an equal fraction of the total thrust, $2T$, where $T=W/2$ and W is the weight of the aerial vehicle. The induced velocity of the rotor system is then:

$$V_i = \sqrt{\frac{2T}{2\rho A}} \quad (2.22)$$

The total induced power of the coaxial rotor system is given by:

$$P_{i,coaxial} = 2TV_i = \frac{(2T)^{\frac{3}{2}}}{\sqrt{2\rho A}} \quad (2.23)$$

If the rotors are considered separately, the induced power is given by:

$$P_{i,hover} = 2 \frac{T^{\frac{3}{2}}}{\sqrt{2\rho A}} \quad (2.24)$$

By comparing these results, the interference-induced power factor can be calculated:

$$k_{int} = \frac{P_{i,coaxial}}{P_{i,hover}} = \sqrt{2} \quad (2.25)$$

This yields 41 % increase in induced power for coaxial rotors compared to two isolated rotors. Anyhow, experiments of closely spaced coaxial rotors have shown that this result is overly pessimistic. The main reason is due to the actual spacing between the rotors [9].

A number of studies have examined the performance of coaxial propulsion, but most of them are for relatively large rotor diameters [10]. In a study performed by Bondyra et al. [11] they found that coaxial propulsion requires between 17 to 29 % more power to produce the same thrust as two separated propellers. The experiments were performed with propellers of diameters of 10", 16" and 26", and the smaller propellers showed the best performance. Another study by Sharft et al. [12] estimates that the thrust of an octocopter would be reduced by 14 % relative to eight independent propellers. This translates to about 20 % increased power requirement for a 27" propeller generating 3000 g of thrust. In a paper by Simoes [13] the performance of coaxial propulsion was predicted by Glauert's theory, which is based upon actuator-disk theory. The estimates shows increased power

requirements of 22 % when the two propellers are operated at the same power, and the lower propeller is in the “far wake” of the upper propeller.

Based on these articles, an additional power requirement of 22 % is assumed in the calculations of required power in this thesis.

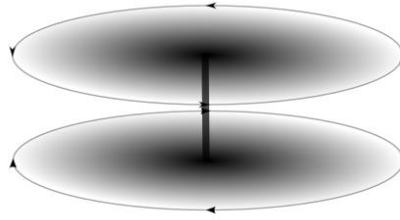


Figure 2-6: Rotor discs in coaxial configuration.

2.2.5 Effects of drag

Parasitic drag influences the cruise speed and the fuel consumption of any vehicle and is hence an important aspect in design of the vehicle. Drag is the resistance an object experience when moving through a fluid, such as air or water. The drag coefficient is a dimensionless quantity used to describe the magnitude of this resistance, where a high number yields larger resistance. The drag coefficient C_d is given by:

$$C_d = \frac{D}{\frac{1}{2}\rho V^2 S} \quad (2.26)$$

where D is the drag force, ρ is the air density, V is the relative velocity of the fluid, and S is the reference area which may either be the wetted area or the projected area of the object. The drag coefficient is not a constant, but is affected by Reynolds number. The geometry of the object has large effect on the drag coefficient; large or sharp angles can result in flow separation and the formation of strong trailing vortices. The drag coefficient is difficult to predict for any object other than simple ones such as spheres, rectangles, cylinders etc. All the components of a drone such as the fuselage, rotor shafts, and extra equipment, together with the fact that the fuselage operates in the rotor wakes makes it difficult to predict the drag. Numerical methods in computational fluid dynamics (CFD) such as Navier-Stokes and Reynolds-Avaraged Navier-Stokes(RANS) are frequently used to predict the drag. These models do not necessary give the correct result, and to supplement or verify the results, wind-tunnel testing of subscale models is used.

Another method that has been frequently used in the helicopter industry to supplement predictions from CFD-analysis, is a semi-empirical drag prediction method, which is based on wind tunnel-testing of the various components that makes up the helicopter. Knowledge of the drag coefficients of the parts that make up the helicopter is used to estimate the fuselage parasitic equivalent wetted or flat plate area, f :

$$f = \sum_n C_{d,n} S_n \quad (2.27)$$

where S_n is the area on which C_d is based. Now equation (2.26) can be expressed as:

$$f = \frac{D}{\frac{1}{2}\rho V^2} \quad (2.28)$$

This method has shown to give reasonable initial estimation of the fuselage drag, even though the interference effects between the different components is not taken into account [9].

2.3 BRUSHLESS DC MOTOR

The electric energy from the energy storage is transformed to mechanical energy through an electric motor. Electric motors are easy to design and built for a UAV and requires low maintenance, which makes them popular choice for propulsion of small UAVs. Most frequently used is the brushless DC motor, which offers high reliability (the motor is purely inductive, so the motor life is primarily limited by the bearings), high performance (efficiency up to 85-95 %), smooth operation which reduces the dynamic load on the propeller, and quiet operation. The electric motor operates with constant voltage, while the current varies dependent on the load. For a steady voltage, the rotational rate will remain constant regardless of load, as shown by the following relationship [5]:

$$rpm_{mot} = K_v V_{mot} \quad (2.29)$$

where rpm_{mot} is the rotational speed per minute of the motor shaft, K_v is the motor voltage constant, and V_{mot} is the voltage across the leads.

2.4 BATTERY TECHNOLOGY

A battery is an electrochemical device which generates electricity from stored chemical energy. As fuel cells, they consist of two electrodes separated by an electrolyte, where the electrons travel in an outer circuit. Batteries are classified in two types [14]:

- Primary battery: Disposable battery which cannot be recharged
- Secondary battery: Rechargeable battery. The battery is recharged by doing the reverse chemical reaction by supply of electricity.

For propulsion of small UAVs several secondary battery types have been used, namely Nickel cadmium (NiCd), Nickel metal hydride (NiMH), Lithium-ion(Li-ion) and Lithium polymer (LiPo). Table 2-1 gives an overview of the metrics for the different battery types. From the table it is seen that Lithium sulfur batteries has the best theoretical and practical specific energy, but the cells that are currently available suffers from poor charge/discharge cycles. The battery with the second best metrics is the LiPo battery which also is the most frequently used battery in UAV applications [5]. LiPo batteries offer relatively high specific energy (~150 Wh/kg) and high energy density (~400 Wh/L), and hence make them well suited for weight and volume sensitive applications. Additionally LiPo batteries have long life cycles (more than 1000 cycles) [15].

Table 2-1: Metrics of different battery types [5].

Battery type	Theoretical Specific Energy, Wh/kg	Practical Specific Energy, Wh/kg	Specific Power, W/kg	Cell Voltage, V
Nickel Cadmium(NiCd)	240	60	150	1.2
Nickel metal hydrid(NiMH)	470	23-85	200-400	0.94-1.2
Lithium Ion(Li-ion)	700	100-135	250-340	3.6
Lithuim polymer(LiPo)	735	50.7-220	200-1900	3.7
Lithium sulfur(LiS)	2550	350	600-700	2.5

As seen from Table 2-1 the cell voltage (also known as the open circuit voltage) is quite low for all the battery types, and to get desired voltage and current output the cells are arranged in series or parallel, or a in a combination. The theoretical energy is the maximum energy that can be delivered by a specific electrochemical system:

$$Energy (Wh) = Voltage(V) \cdot Capacity(Ah) \quad (2.30)$$

Under discharge, batteries as fuel cells suffers from different losses, where the major contributors are cell resistance and polarization of active materials. Figure 2-7 illustrates typical discharge curves. The ideal curve shows that the battery operates at the open circuit voltage and can utilize all the capacity. Curve 1 and curve 2 represent typical real discharge curves, where the discharge voltage is lower than the theoretical voltage. This is because the voltage drops due to accumulation of discharge products which is continually increasing the resistance as time lapses. Curve 2 has a higher discharge rate than curve 1, which is recognized by that the voltage drops faster and less of the capacity is utilized [14].

The voltage during discharge V_{dis} is given by [14]:

$$V_{dis} = V_{oc} - I_{dis}R_i \quad (2.31)$$

Where V_{oc} is the open circuit voltage, I_{dis} is the discharge current and R_i is the internal resistance.

A parameter frequently used to compare batteries with different capacities is the C-rate. The C-rate is a measure of the rate of charge or discharge relative to the battery capacity C. A 1C rate means that the battery will be entirely discharged in one hour at the specified discharge current. This means that a battery with capacity of 10000mAh will be fully discharged in one hour at a discharge current of 10 A at a 1C rate. At a 2C rate the discharge current would be 20 A, and the battery would be fully discharged in 30 minutes [15].

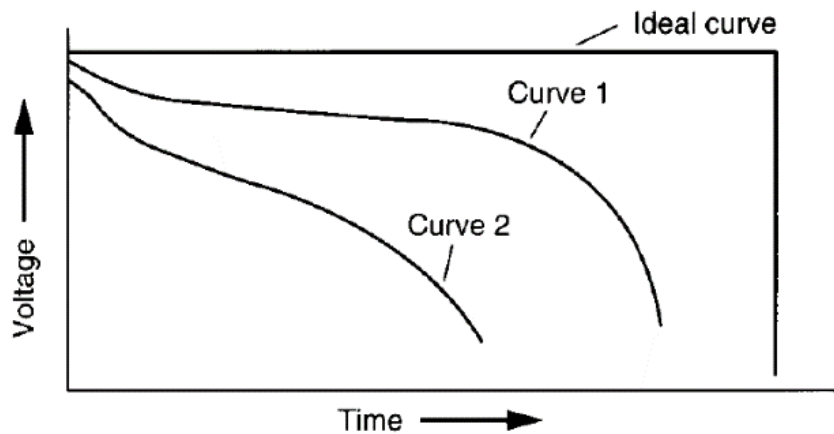


Figure 2-7: Shows the discharge curve for an ideal secondary battery and two curves (Curve 1 and Curve 2) for an actual secondary battery [14].

3 FUEL CELL TECHNOLOGY

The first fuel cell was invented by William Grove in 1839, but the technology first began to flourish after the 1950s when a fuel cell was used to supply electricity and water in a spacecraft. Over the last decade the research and development of fuel cells have had a massive growth as the world are looking for replacement for fossil fuels. New markets are discovered, and current applications range from laptops to large power plants. Fuel cells can theoretically be used for any device requiring energy [16]. This chapter will provide the fundamental principles of fuel cells and an overview of different types of fuel cells relevant for UAV applications. Furthermore, there will be a closer look at different hydrogen storage methods.

3.1 THE BASICS

Fuel cell and batteries relies on the same principles from electrochemistry, but are different because fuel cells continue to provide electricity as long fuel is supplied, whereas batteries get used up, and are thrown away or recharged. The combustion of hydrogen involves that hydrogen-hydrogen and oxygen-oxygen bonds are broken by the transfer of electrons, and new hydrogen-oxygen bonds are formed. The hydrogen-oxygen product has a lower energy level than the reactants, and the energy difference is released as heat. This heat is difficult to utilize, and a better option is to make use of the electrons involved in the reaction. This is exactly what a fuel cell does by spatially separating the hydrogen and oxygen reactants with the use of an electrolyte. An electrolyte is a material that allows ions to pass through, but not electrons. In this way, the electrons are forced to travel in an outer circuit to complete the reaction, and by applying an external load we can make use of the energy of the electrons. An illustration of a simple fuel cell is shown in Figure 3-1 [17].

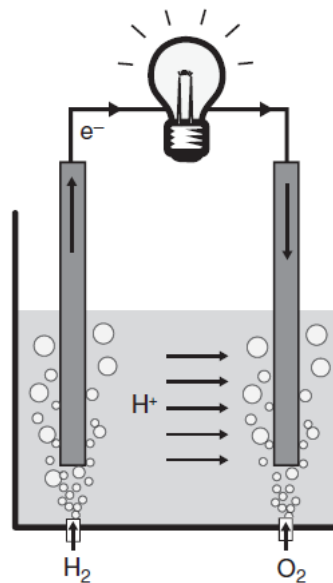
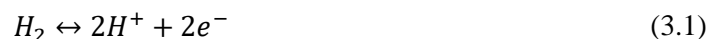


Figure 3-1: A basic fuel cell [17].

The half reactions in a hydrogen fuel cell are as follows:



In contrast to Figure 3-1 fuel cells are most often configured as shown in Figure 3-2, where the electrodes are thin planar structures. This is because the produced electricity scales with the reaction area. Increasing the area result in greater currents. The reason is that the half reactions has a finite rate and must occur at the reaction surface. The electrodes are made of porous material for further increase of the reaction area.

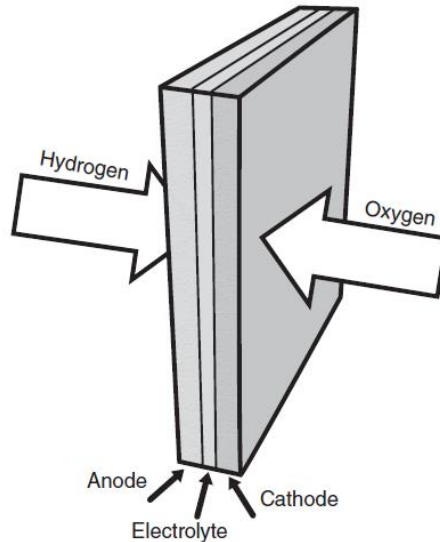


Figure 3-2: Planar structure of a fuel cell.

The main steps involved in producing electricity in a fuel cell are as follows:

1. Transport of fuel(reactants) into the fuel cell
2. Electrochemical reaction at both reaction areas
3. Transfer of electrons through the external circuit, and transfer of ions through the electrolyte
4. Removal of products from the fuel cell

The amount of energy an ideal fuel cell can produce is determined by thermodynamics, where one important equation is the differential expression for enthalpy:

$$dH = dU + dW \quad (3.3)$$

which states that the change in enthalpy (dH) equals the change in the internal energy (dU) and the work performed *by* the system (dW). The change in enthalpy is the amount of heat that can be generated by combustion of hydrogen, and is often called enthalpy of reaction when associated with a chemical reaction. The enthalpy of reaction is expressed in energy per mole. The enthalpy of reaction for combustion of hydrogen at standard state conditions (STP) is $\Delta h = -285.8$ kJ/mol. Equation (3.3) shows that in an ideal world, all the enthalpy could be used to perform useful work. Unfortunately, this is not the case, and the amount of energy created by the reaction that can perform useful work is given by Gibbs free energy. For a hydrogen-oxygen fuel cell at STP, Gibbs free energy is $\Delta g = -237.17$ kJ/mol. Now we can determine the theoretical maximum efficiency of a hydrogen-oxygen fuel cell, also called the reversible efficiency:

$$\epsilon_{thermo} = \frac{\text{useful energy}}{\text{total energy}} = \frac{\Delta g}{\Delta h} = \frac{-237.2}{-285.8} = 0.83 \quad (3.4)$$

Similarly, Gibbs free energy can be used to find the reversible voltage. The electrical work a system can perform is given by the potential (E) measured in volt, and the electrical charge (Q) carried by the electrons, measured in coulomb. The charge is given by the amount of electrons per mole (n) and Faraday's constant (F), which gives:

$$-\Delta g = W_{elec} = QE = nFE \quad (3.5)$$

Inserting values, and solving for the potential gives the reversible voltage of $E^0 = +1.23$ V. This is the maximum voltage a hydrogen-oxygen fuel cell can deliver, without any kind of irreversible losses. Real fuel cell efficiency is lower due to additional voltage losses and fuel utilization losses, given by the equation:

$$\varepsilon = \varepsilon_{thermo} \varepsilon_{voltage} \varepsilon_{fuel} \quad (3.6)$$

The voltage losses gives the characteristic shape of the current-voltage diagram (i-V diagram) associated with a fuel cell, shown in Figure 3-3. The i-V diagram shows the actual voltage and current output of a fuel cell. The current is expressed in terms of ampere per square centimeter to exclude the effect of the reaction area. An ideal fuel cell would produce any current and have constant voltage equal to the reversible voltage. The voltage losses are divided in three major types; activation losses, ohmic losses and concentration losses. The voltage efficiency is given by the ratio between actual voltage output and the reversible voltage:

$$\varepsilon_{voltage} = \frac{V}{E^0} \quad (3.7)$$

From this equation and the i-V diagram we see that the voltage efficiency is higher when the fuel cell is operating at low current densities. There is also a maximum limit of power that can be delivered, shown by the power density curve in the Figure 3-3. A fuel cell is designed to operate at or below the maximum power density. The power output from a fuel cell is calculated by the product of the voltage and the current:

$$P = iV \quad (3.8)$$

Not all the fuel are utilized to electrical work. Some of the fuel simply flows right through the fuel cell, and some undergoes other chemical reactions which does not produce electricity. The fuel utilization efficiency is given by the ratio between the fuel consumed and the fuel that is supplied to the fuel cell in moles per second:

$$\varepsilon_{fuel} = \frac{\text{fuel consumed}}{\text{fuel supplied}} = \frac{i/nF}{v_{fuel}} \quad (3.9)$$

The fuel utilization efficiency is typical 95 % for a well-designed PEMFC[18].

Note that the reversible efficiency and the reversible voltage calculated in the above paragraphs is based on the higher heating value of hydrogen. The higher heating value (HHV) of hydrogen is a measure of the amount of heat that can be generated by hydrogen combustion when liquid water is produced, whereas the lower heating value (LHV) is used when the reaction product is water vapor. It should always be stated whether the efficiency is based on HHV or LHV, because LHV gives a higher efficiency figure.

For comparing different fuel cells, measures like *power density* and *specific power* are often used:

$$\text{Power density} = \frac{\text{Power}}{\text{Volume}} \quad (3.10)$$

where the volume is either given in cubic meters or liters, and:

$$\text{Specific power} = \frac{\text{Power}}{\text{Mass}} \quad (3.11)$$

where the mass is given in kilograms[19].

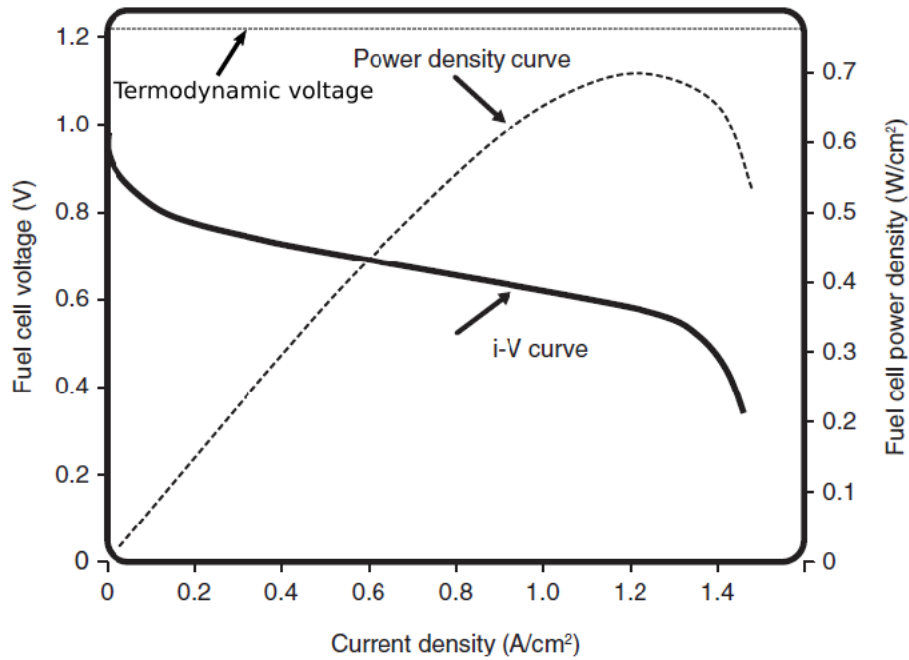


Figure 3-3: Combined current-voltage diagram(*i-V* curve) and power density curve. Modified from ref. [17].

3.2 BENEFITS AND LIMITATIONS

Fuel cells share many of the characteristics with combustion engines and batteries, and in some way, combine the advantages of both. Like combustion engines, fuel cells continue to produce energy as long as fuel is supplied. But fuel cells are often far more efficient than combustion engines because the energy is directly drawn from the chemical reaction, whereas combustion engines transform heat energy from the chemical reaction into mechanical work. Because there are no moving parts in fuel cells, they have potential to be highly reliable and silent. Compared to batteries, fuel cells often have larger specific energy, which in the case of small UAVs is a very important attribute to enhance the endurance. Current battery technology can provide Lithium polymer (LiPo) cells with specific energy on the order of 150-200 Wh/kg, where fuel cells in principle could provide any specific energy, because it is determined by the fuel storage size [20]. Another great advantage fuel cells have in relation to batteries, is that they are easy to scale, and the capacity (fuel storage) and power (fuel cell size) are scaled independently. In addition, fuel cells can be scaled from 1 W up to several MW, while batteries scale poorly at large sizes [17].

Even though the advantages are great and many, fuel cells also have some serious drawbacks. First of all, combustion engines and batteries outperform fuel cell when it comes to power density and specific power. Even though there have been great improvements over the last decade, more work must be done for fuel cells to compete in the market of automotive and portable devices. Another major drawback is the high cost of implementation of a fuel cell system due to the use of platinum-based catalysts, delicate membrane fabrication techniques, and other components such as fuel storage, pumps, compressors and control systems. Furthermore, there are issues with fuel availability and storage, which can lead to practical difficulties. Fuel cells also have operational temperature concerns, are susceptible to environmental issues, and have durability difficulties under start-stop cycles[16].

Because of this, fuel cells are still mostly used in niche markets (including small UAVs), but there are hope to overcome these obstacles as the interest for fuel cells continues to grow [16].

3.3 TYPES OF FUEL CELLS FOR SMALL UAV APPLICATIONS

There have been developed many types of fuel cells since the invention in 1839. The fuel cells are categorized based on which electrolyte they use. In this section three fuel cell types which are relevant for UAV applications will be discussed, namely polymer electrolyte membrane fuel cell (PEMFC), direct methanol fuel cell(DMFC) and solid-oxide fuel cell (SOFC). PEMFC and SOFC are the farthest most used fuel cells, and hence has the most mature technology. For portable devices both PEMFC and DMFC shows great promise due to their low operating temperature compared to other fuel cells. Table 3-1 shows a comparison of the three fuel cell types.

Table 3-1: Fuel cell types used in small UAV applications[16, 19, 21].

	Fuel	Efficiency (%)	Temp(°C)	Specific power (W/kg)	Capital cost(\$/kW)
PEMFC	Hydrogen	40-60	30-100	400-1000	100
DMFC	Methanol	20-30	20-90	50-200	200
SOFC	Hydrocarbon	25-50	500-1000	>800	-

All three of the fuel cell types listed in the table above have earlier been used in small fixed-wing UAVs. In 2008, the University of Michigan set a flight time record with their Endurance UAV, achieving 10 h and 15 min[22]. This was the first time a SOFC was used in a small UAV. A DMFC was implemented in a 11.5 kg conventionally configured UAV by University of Korea in 2013 [23], but the flight time only reached 11 min. The unofficial endurance record is currently hold by the Ion Tiger team, with flight time of 48 h, using a PEMFC and liquid hydrogen storage[24]. For VTOL UAVs on the other hand, the use of fuel cells have been limited to demonstrations, and with current technology, flight time is estimated to be 2-3 times longer than the best batteries[20]. VTOL UAVs requires far more power than fixed-wing small UAVs because they do not have passive lift. Small VTOL UAVs powered by batteries have usually flight times of less than 1 hour.

Because of the high power demand, the PEMFC is currently the most suited for small VTOL UAVs. A study performed by Bradly et al.[25] comparing five small-scale UAV propulsion system, including LiPo battery, internal combustion engine, SOFC and PEMFC, showed that the PEMFC with gaseous hydrogen has greatest potential with respect to both range and endurance. Furthermore, PEMFC this is the most efficient fuel cell of the three listed in Table 3-1, resulting in that the carriage of hydrogen fuel will be less than for the other two. It is also the most common commercial fuel cell for use in UAVs. For these reasons, a PEMFC fuel cell will be used in the system design process in this thesis, and further details about the PEMFC are discussed in the next section

3.4 POLYMER ELECTROLYTE MEMBRANE FUEL CELL (PEMFC)

By offering the highest specific power of all currently available fuel cells, the PEMFC are a good choice for many applications, and the automotive industry have almost exclusively used PEMFC. PEMFC runs on hydrogen fuel, and as stated by the name, has a polymer electrolyte membrane. The membrane is a proton-conductor, and hence the two half-reactions in the PEMFC are similar to those of a basic fuel cell (equation (3.1)-(3.2)), and the overall cell reaction is:



The thin (20-200 μm) polymer membrane together with two porous carbon electrodes coated with a platinum-based catalyst, make up what is called a membrane electrode assembly (MEA), shown in Figure 3-4. The thickness of MEA is less than 1 mm, which results in that PEMFC easy can be assembled to a stack, where sizing is determined by the required voltage and power (more about fuel cell stacks in section 3.5).

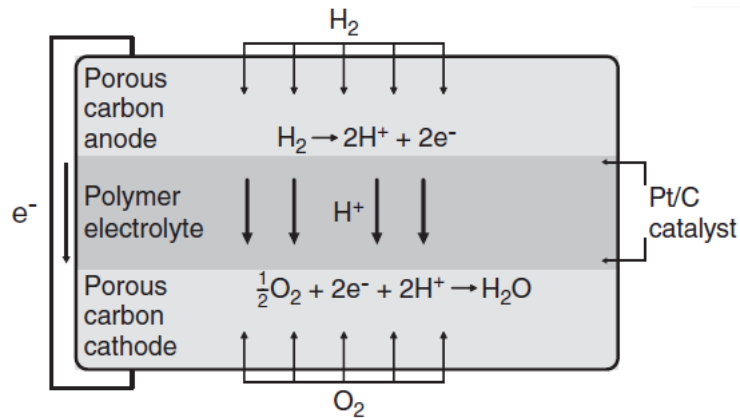


Figure 3-4: Membrane electrode assembly of PEMFC [17].

The membrane needs liquid water to maintain conductivity, so the working temperature is less than 90°C. Because of the low temperature, only platinum-based catalysts are currently available, but extensive research is done to find cheaper alternatives [16]. Anyhow, the low working temperature makes PEMFC well suited for portable applications such as UAVs, offering fast start, and good on-off cycling characteristics.

The fuel cell system requires water management to hydrate the membrane, which increase the complexity and cost of the system. In addition, there are issues with drying membrane at the anode side, and flooding membrane at the cathode side. Table 3-2 summarize the advantages and disadvantages of PEMFC [17, 26].

Table 3-2: Properties of PEMFC.

Advantages	Disadvantages
Highest power density of all fuel cell types	Needs very pure hydrogen
High efficiency	Water management
Compact	Expensive catalyst material
Fast start	Expensive membrane
Low-temperature operation	
Versatile	

3.5 FUEL CELL STACK SIZING

The power output of a single fuel cell is not enough in most applications. Consequently, the fuel cells are arranged in series to increase the power output. The most common configuration for a PEMFC is bipolar plate stacking, also called vertical stacking. This configuration uses a single conductive flow structure to connect the fuel cells. The flow structure is in contact with the fuel electrode of one cell, and the oxidant electrode of another, similar to how batteries are stacked in a flash light. This

configuration gives a robust fuel cell stack, with low ohmic losses due to the good conductivity of the flow structure. The cell voltage V_{cell} is a function of the current density, given by the i-V curve:

$$V_{cell} = f(i) \quad (3.13)$$

Normal operating point is between 0.6 and 0.7 V at nominal power. Fuel cell systems could also easily be made to operate at 0.8 V per cell if they are properly designed. The stack output voltage is simply the sum of the cell voltages:

$$V_{st} = \sum V_{cell} = V_{cell}N \quad (3.14)$$

where N is the number of cells in the stack. When designing a fuel cell stack, the number of cells is often determined by the required operating voltage and the maximum voltage. The stack current is equal to the cell current, which is given by:

$$I = iA_{cell} \quad (3.15)$$

where i is the current density and A_{cell} is the cell active area. The required current is obtained by varying the cell area. The power output of the fuel cell stack is the product of the stack voltage and the current:

$$P_{st} = V_{st}I \quad (3.16)$$

[27]

3.6 FUEL CELL COMPONENTS AND DESIGN

The heart of the fuel cell system is the fuel cell stack, but for the stack to function in a desired and stable manner, a set of subsystems is required. Proper design and sizing of the system as whole, based on available technology, is key to in order to achieve the advantages of fuel cell systems [28]. The subsystems required to operate a fuel cell can be categorized as follows:

- Fuel supply system
- Heat management system
- Water management system
- Power electronics

All these subsystems, frequently referred to as Balance of Plant (BOP), often takes up more space and cost than the fuel cell stack. The components that requires electricity themselves are called parasitic power devices. A brief description of the different subsystems will be given in the following sections. For successfully integrating a fuel cell system, all these subsystems need to work harmonically together. Materials of the different subsystems must also be compatible. The PEMFC would be contaminated and suffer from corrosion if the subsystems are not made of inert materials, such as stainless steel, titanium or different grades of rubber. Achieving high overall system efficiency yields a complex optimizing task, where many trad-offs must be made. Factors that influence system efficiency are, among others, operating voltage, operating pressure, temperature and fuel and oxidant composition and utilization. For example, operating the fuel cell at high voltage leads to high thermodynamic efficiency but the cell area has to be increased to give the same power output, resulting in a larger fuel cell stack. Figure 3-5 illustrates different factors that influence efficiency.

Operating the fuel cell at a higher temperature would reduce ohmic losses but increase the waste heat, but in portable PEMFC waste heat is difficult to utilize. The pressure can be increased to enhance the process performance and fuel cell output, at expenses of equipment that can withstand high pressure, and higher capital cost for the compressor. Fuel and oxidant utilization should be kept high to reduce the fuel carriage, but too high utilization can result in voltage drops [26].

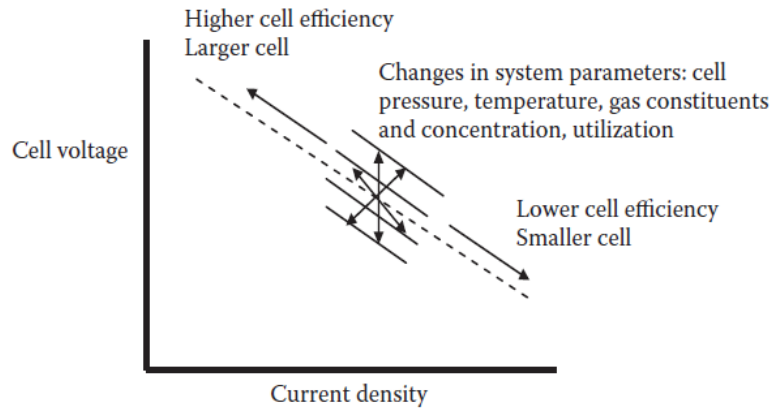


Figure 3-5: Different factors that influence fuel cell efficiency [26].

3.6.1 Fuel processing system

Fuel processing involves steps of transforming the fuel into a substance suited for the anode reaction. The complexity of the fuel processing system is highly dependent on which type of fuel is used. Pure hydrogen is often used in PEMFC and has the simplest fuel processing system, whereas SOFC often uses hydrocarbons as fuel which require a method to convert the fuel into a gas reformat. Fuel processing also includes cleaning of the fuel to get rid of impurities with detrimental effects on the fuel cell.

3.6.2 Heat management system

Thermal energy generated by the fuel cell stack is removed either by using air or a coolant fluid. In small PEMFCs, passive cooling via air that hits the outer surface of the fuel cell is often enough. But as the fuel cell stacks get larger, the surface-to-volume ratio decrease, and heat is not as easily transported out to the surface. Larger PEMFC (>1000 W) often needs active cooling which involves either air supplied by a blower, or a liquid coolant system.

3.6.3 Water management system

Water management is one of the most important subsystems for the PEMFC. Since water is created at the cathode side, a water removal system is required to prevent blockade of reaction sites. The PEMFC also needs humidification of the membrane to enhance proton transfer and efficiency. To achieve that, the fuel and the air is humidified before going into the fuel cell stack.

3.6.4 Power electronics system

The electric power of a fuel cell is not stable, and the voltage output can differ significantly, as seen from the i-V curve. Power regulation involves keeping the voltage constant over time, even when the load changes. This is achieved by using a DC-DC converter, which supply a fixed voltage to the load. It can either be a step-up converter or a step-down converter, which transform the fuel cell voltage to a higher or lower value, respectively[26]. In both cases the power must be conserved (minus some losses in the converter itself), meaning that using a step-up converter will result in lower current output. Efficiency of DC-DC converters are typically in the range of 85-98 % and is higher when the input voltage increase.

Monitoring the system involves using gauges and sensor to measure the state of the fuel cell, such as temperature, pressure, flow rates etc. For changing certain conditions in the system, actuators such as valves, pumps, switches and fans are used. A central control unit are used to control the interaction between the monitoring devices and the actuator devices. The control unit must ensure that the fuel cell is operating in a stable and desired manner.

When designing a portable fuel cell system, where mobility and specific energy are most important, the incentives are strong to keep the number of different BOP components low.

3.7 HYDROGEN STORAGE SYSTEMS

Hydrogen storage is one of the major barriers that must be solved for fuel cells to be commercialized. Hydrogen gas has low density (0.089 kg/m³ at STP) and low boiling point (-252.9 °C) which complicates the storage [26]. Different methods are used to improve the gravimetric and volumetric efficiency. In UAV applications current storage methods are [21]:

- Compressed hydrogen gas
- Liquid hydrogen
- Chemical hydrogen

Table 3-3 gives a comparison of state of the art metrics of these three methods, and the next sections provide further details.

Table 3-3: Comparison of hydrogen storage systems. The mass and volume used in these data includes tank, valves, tubing and regulators [17] [26].

Storage system	Mass Efficiency (% kg H ₂ /kg storage)	Volumetric Density (kg H ₂ /L storage)	Specific energy (Wh/kg)	Energy density (Wh/L)
Compressed H₂, 300 bars	3.1	0.014	1200	550
Compressed H₂, 700 bars	4.8	0.033	1900	1300
Cryogenic liquid H₂	14.2	0.043	5570	1680
Chemical Hydride Cartridge (HES)		-	560	390
SBH Cartridge (Protonex)		-	500-660	290-370

3.7.1 Compressed hydrogen

Storing the hydrogen as compressed gas is the simplest and most frequently used method. The hydrogen is stored at high pressures ranging from 30 MPa to 70 MPa to increase the density. Special material and design are required to withstand the high pressure and it is important with lightweight and reliable valves and pressure regulators to achieve high gravimetric efficiency, especially in small-scale pressure tanks [21]. The gravimetric efficiency is between 1-3 % for steel cylinders. Generally the gravimetric efficiency increases with the scale of the tank and increased pressurizing [17, 19], but high pressure can cause safety problems. Composite tanks can achieve higher efficiency, but the cost is approximately 3.5 times greater than steel cylinders [29]. Anyhow, the reduced weight is an important attribute in UAV applications. In 2011 the Ion Tiger team managed to get a hydrogen storage fraction of 13 % with the use of a custom carbon-wound tank with aluminum liner [30]. The tank had a mass of 3.8 kg and a storage capacity of 500 g H₂ at 35 MPa.

The use of compressed hydrogen gas has some practical issues, although the continuous growth of interest for fuel cells have led to abundantly of commercial suppliers of high-purity hydrogen stored in tanks. Still there are some locations where the hydrogen infrastructure is not easily accessible. One option is to use a hydrogen generator which produce hydrogen on-site through water electrolysis. For refueling at remote sites, EnergyOR has developed a hydrogen filling station which requires no electrical power [31], and HES Energy Systems are currently developing one [32].

3.7.2 Liquid hydrogen

Liquid hydrogen (LH_2) has the highest mass efficiency of the three storage methods discussed for UAV applications, but the temperature needed to form a hydrogen liquid is modest 20 K at 1 bar. A gas cooled to such low temperatures to form a liquid is called a cryogenic liquid [19]. LH_2 has density of 71 kg/m^3 at 1 bar and is the most efficient way to store hydrogen, and hence the most frequently used method to store large amounts of hydrogen. A major problem though, is that hydrogen is continuously evaporating and cannot be stored over long periods. It is therefore not a preferred method for on-board storage in vehicles [33]. Although, LH_2 is frequently used for rocket propulsion in space flights, where the gravimetric efficiency is of great importance. There have been a demonstration of a liquid hydrogen system used in a fixed-wing UAV by NRL [24]. The storage system reached a specific energy of 7600 Wh/kg and the UAV reached a flight-time of 48 h, setting a world record at that time. This shows that using liquid hydrogen has potential, but are currently not suited for widespread use because the infrastructure of LH_2 does not support delivery to where it is going to be used. Another major drawback is that unplanned flights are difficult to carry out because the preparation includes cooling of the cryogenic tank with liquid nitrogen, filling with it LH_2 , and then the tank must reach thermal equilibrium. Reaching thermal equilibrium took 4 hours for the system by NRL, and further development is needed before this method can be used in commercial UAV applications.

3.7.3 Chemical hydrogen

In chemical hydrogen storage by absorption, the hydrogen atoms are dissociated in the lattice of the host material. Since storing hydrogen both as gas and as liquid has major practical difficulties as well as other issues, there is intensive research of chemical hydrogen storage worldwide [33]. Chemical hydrogen offers relatively high energy densities and operation at low pressures and ambient temperatures, reducing the safety risks. In UAV applications materials such as sodium borohydride, ammonia borane and liquid hydrocarbons have been investigated [21]. Sodium borohydride ($NaBH_4$) is the most popular solution for chemical storage in UAVs and is also commercially available from HES energy which offers a cartridge system for easy handling. $NaBH_4$ undergoes a reaction to produce hydrogen fuel onsite. The advantages of $NaBH_4$ is high hydrogen storage capacity (10.8 wt%), relatively high energy density, easy control of hydrogen generation rate and high stability [34]. Additionally, they can contain large amounts of water vapor, which is favorable for PEMFC. The major drawbacks are the high price of approximately \$630 per kilogram and the relatively low specific energy [19].

3.8 HYDROGEN SAFETY

Hydrogen has the lowest molecular weight, viscosity and density of all gases. The storage of hydrogen is challenging because of leakage and that the hydrogen molecules easily diffuse into materials, which can cause embrittlement. Another factor that needs to be considered is the low ignition energy; a spark from a person can cause ignition if the concentration of hydrogen is high enough. Anyhow, hydrogen is generally not considered as more dangerous than other commonly used fuels.

Storing hydrogen at high pressures is associated with safety problems. A leak from a high pressurized tank would cause very large forces as the gas is propelled out. Additionally, the rupture of a pressure vessel would very likely cause ignition of the hydrogen and oxygen mixture, and the flame would last until the tank is empty. Even though, storing of hydrogen at high pressures is considered as safe, as the problems are handled by following correct procedures. In vehicles, relief valves and rupture disc are used to vent the gas in a potential accident.

Storing hydrogen as a cryogenic liquid imposes other safety considerations. The pressure is usually kept below 3 bar, but the pressure can easily rise if the temperature increases. A spring-loaded valve is usually used to vent the gas if the pressure gets too high, and then close again when the pressure drops.

Another issue is the handling as human skin easily can get frozen in contact with the low-temperature liquid hydrogen. Anyhow, storing hydrogen as a cryogenic liquid is considered somewhat less hazardous than storing hydrogen as compressed gas. In case of a tank failure, the gas will be kept in place, and slowly vent to the atmosphere [19].

3.9 COMPRESSION OF HYDROGEN GAS

To describe the state of a gas, the ideal gas law is frequently used, and is given by:

$$pV = nRT \quad (3.17)$$

where p is the pressure given in Pa, V is the volume of the gas, n is the number of moles, R is the universal gas constant ($R=8.314 \text{ J/Kmol}$) and T is the absolute temperature. For hydrogen gas, the ideal gas model can be used up to 100 bar. At higher pressures the ideal gas model significantly underestimates the volume occupied by the gas. To deal with this, numerous of real gas laws have been developed. Among these are the frequently used van der Waals method and the compressibility factor method. Both these methods yield the same results for compressed hydrogen up to 400 bar. The compressibility factor method introduces a parameter Z to correct the ideal gas law:

$$pV = nZRT \quad (3.18)$$

The parameter Z is experimentally determined, and Figure 3-6 shows Z for different pressures and temperatures for hydrogen.

Compression of hydrogen requires energy. The amount of energy can easily be calculated for an isothermal or adiabatic compression process, which gives the lower and upper limit for the compression energy, respectively. In real applications, most often a multistage compression process is performed. Then the heat gets time to dissipate through the wall, and one gets closer to the ideal isothermal process. Figure 3-7 shows the compression work and the compression energy as percentage of LHV for adiabatic, multistage and isothermal processes. The process involves pressurizing hydrogen from 1 bar up to required pressure.

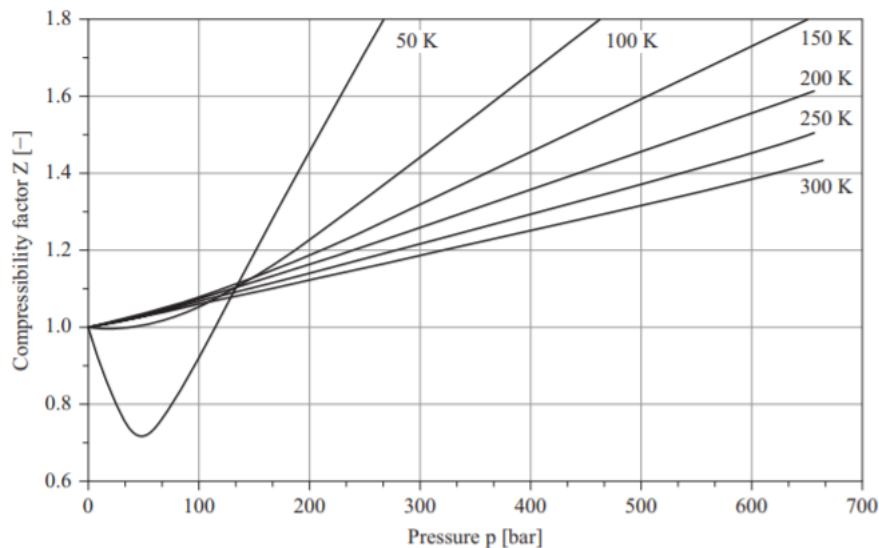


Figure 3-6: Compressibility factor for hydrogen at different pressures and temperatures [35].

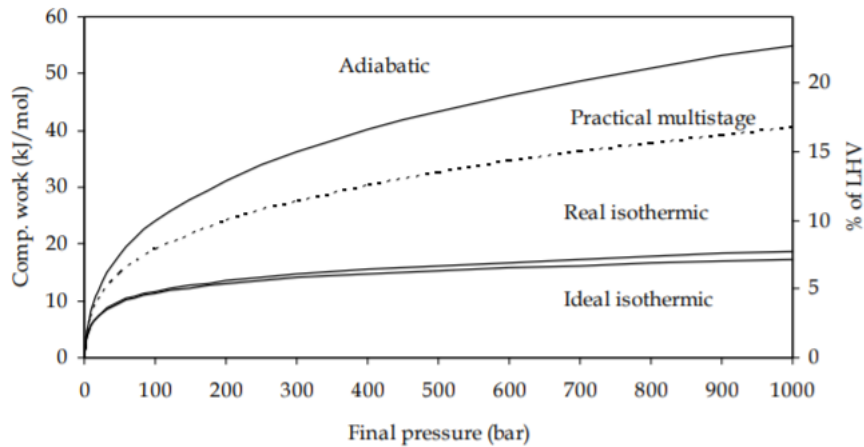


Figure 3-7: compression work and compression energy as percentage of LHV for adiabatic, multistage and isothermal processes. The process involves pressurizing hydrogen from 1 bar up to required pressure [36].

3.10 FUEL CELL BATTERY HYBRIDIZATION

For a VTOL UAV the power demand can vary significantly due different phases in the mission such as climb, hover and forward flight, as well as in cases of maneuvering, acceleration and under influence of wind. As earlier stated, the dynamic response of fuel cells can be very poor, where changing the power output could take from seconds to hours due to different lags in the system. By using batteries or capacitors as energy buffers, the response time is reduced to milliseconds. This is important in VTOL UAV applications, where the required power can vary significantly. In fact, investigation of fuel cell and battery hybridization shows that the battery plays a key role in a high performance system[37]. In addition to take the dynamic loads, the battery also protects the fuel cell for membrane dehydration and fuel starvation [38]. One hybridization scheme is to size the fuel cell to deliver the power needed in hover and to provide excess power to recharge the battery. The battery is sized to handle the peak power that occurs in the climb phase, and to take care of the transient peaks during the mission. In phases with higher power demands both the fuel cell and the battery provide power [37]. Battery hybridization can also be used to manage different power requirements resulting from varying payloads [20]. Figure 3-8 shows an example of a conventional fuel cell-battery hybridization scheme.

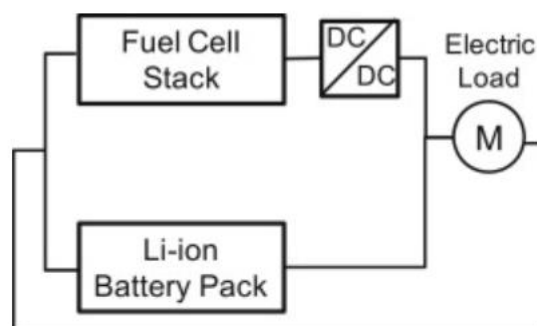


Figure 3-8: Conventional hybrid system [39].

A battery is connected to the output terminals of the DC-DC converter to provide additional power under start-ups and under dynamic loading to take care of the peak power. In low-load operation, excess energy from the fuel cell is used to charge the battery [17].

4 COMPOSITE HIGH PRESSURE VESSEL

This chapter will provide a discussion of different type of pressure vessels, and a brief comparison between spherical and cylindrical pressure vessel. Classical lamination theory which forms the basis for the later calculations of composite pressure vessels, is derived. Furthermore, a discussion of the safety factor used for composite pressure vessels are provided, and some issues regarding the liner.

4.1 PRESSURE VESSEL TYPES

A pressure vessel is a closed structure that contains fluids under pressure. The different types of pressure vessels are shown in Figure 4-1. Type I and II are mainly made of metal, but type II is reinforced with composite material in the hoop direction of the cylinder part. Type II, III and IV are known as composite overwrapped pressure vessels (COPV). The composite is wrapped around the liner in a filament winding process, where the fibers are embedded in a resin (most often epoxy). The composite material is either carbon, glass or synthetics. The difference between type III and IV is the liner material. Type III has metal liner, most often made by aluminum or sometimes titanium, whereas type IV has polymer liner. In both cases, the liner carries little or no load. From left to right in Figure 4-1 the pressure vessels are increasing in cost and decreasing in weight, also illustrated in Figure 4-2. Because of weight penalty, only type III and type IV are relevant in UAV applications. Table 4-1 summarize some of the characteristics of the of type III and IV pressure vessels.

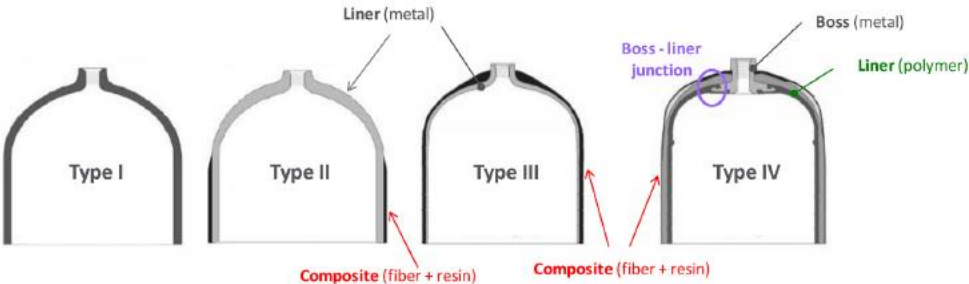


Figure 4-1: Representation of the different types of pressure vessels [33].

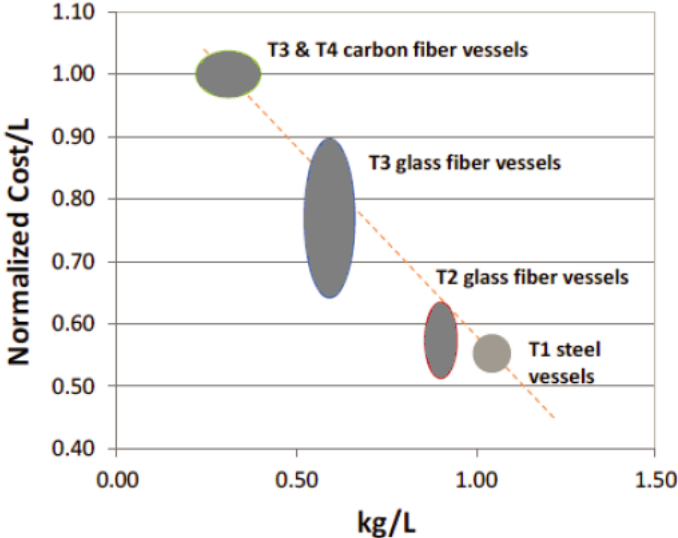


Figure 4-2: Shows the normalized cost versus weight for the different types of pressure vessels [40].

Table 4-1: Characteristics of type III and type IV pressure vessels [40].

	Type III	Type IV
Market share %	<2	<2
Common material	Aluminium liner with glass or carbon fiber overwrap	HDPE liner with carbon fibre overwrap
Indicative cost US\$/L	9 to 14	11 to 18
Indicative weight kg/L	0.4-0.5	0.3-0.4

4.2 SPHERICAL VS. CYLINDRICAL PRESSURE VESSEL

Pressure vessels have commonly the form of cylinders, spheres, ellipsoids, or a combination of these. Spheres are the ideal form as the stresses are evenly distributed, and there are no weak points. Furthermore, spheres have the maximum volume and minimum surface area, and thereby the material requirements are minimized. The major drawback of spherical pressure vessels compared to cylindrical pressure vessels is the manufacturing cost, which is significantly higher. In the aerospace industry, cylindrical pressure vessels are most commonly used because of the aerodynamics. Anyhow, in the case of a VTOL UAV which is potentially flying in all directions, the aerodynamics of a cylindrical pressure vessel is not necessarily better than the spherical pressure vessel. At high pressures, spherical pressure vessels are commonly used. There are no codes or standards that defines where “high pressure” begins, but pressure vessels designed for working pressures of over 3000 psi (206.8 bar) is normally considered as high pressure vessels. Constructing a pressure vessel requires stress analysis, material behavior and safety considerations, illustrated by the triangle in Figure 4-3 [41].

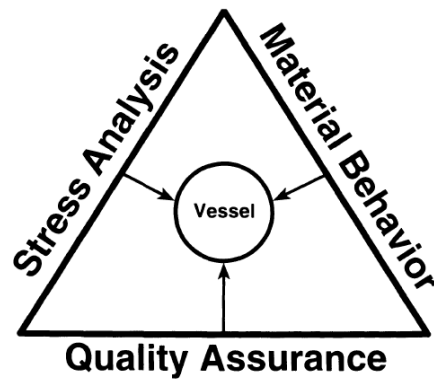


Figure 4-3: Requirements for construction of a pressure vessel [41].

4.2.1 Stresses in a thin sphere

Because of symmetry, the normal stresses, denoted by σ , are equal and constant over the entire vessel. The definition of a thin sphere requires that $R/t > 10$. Then the radial stress σ_r varies from $-p$ to 0 from the inner surface to the outer surface. Because the radial stress is small compared to the other stresses, it is neglected, and the sphere is modelled in the state of plane stress. Because of symmetry and the assumption of plane stress, all shear forces are zero. Figure 4-4 illustrates a thin-walled spherical pressure vessel with internal radius R and thickness t , subjected to an internal pressure p .

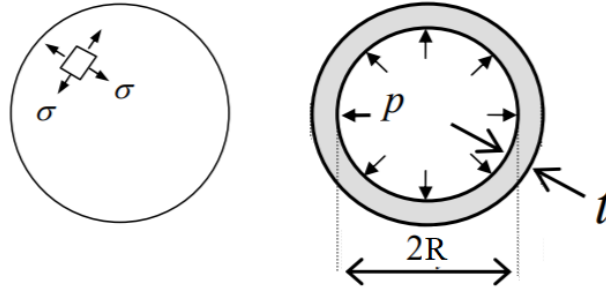


Figure 4-4: A thin-walled spherical pressure vessel (left) σ and cross-sectional view(right).

To find the stresses in terms of the internal pressure, the free body diagram in Figure 4-5 is used and force equilibrium yields:

$$\sigma(2\pi Rt) = p(\pi R^2) \quad (4.1)$$

The stresses are then:

$$\sigma = \frac{pR}{2t} \quad (4.2)$$

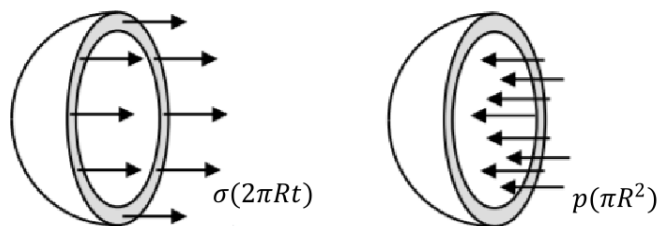


Figure 4-5: Free body diagram of a spherical pressure vessel.

4.2.2 Stresses in a thin cylinder

The same assumptions made for a thin spherical pressure vessel also apply for a thin cylindrical pressure vessel. The longitudinal stress σ_l for a cylinder with radius R , thickness t , and length L subjected to an internal pressure p , is derived from the FBD in Figure 4-6. Force equilibrium yields:

$$\sigma_l(2\pi Rt) = p(\pi R^2) \quad (4.3)$$

which lead to:

$$\sigma_l = \frac{pR}{2t} \quad (4.4)$$

The circumferential stress σ_c is derived from the FBD in Figure 4-7, and force equilibrium yields:

$$\sigma_c(2tL) = p(2RL) \quad (4.5)$$

and so

$$\sigma_c = \frac{pR}{t} \quad (4.6)$$

As for the spherical pressure vessel, the radial stress σ_r is taken to be zero.

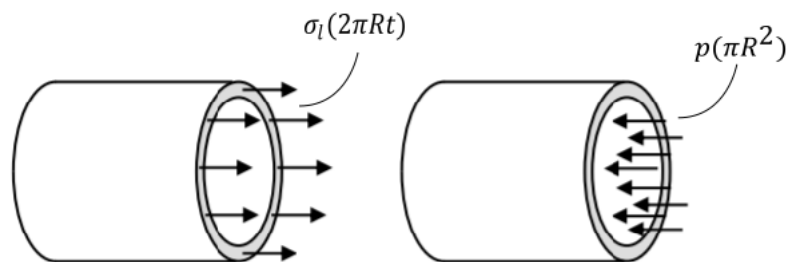


Figure 4-6: Free body diagram of a cylindrical pressure vessel in longitudinal direction.

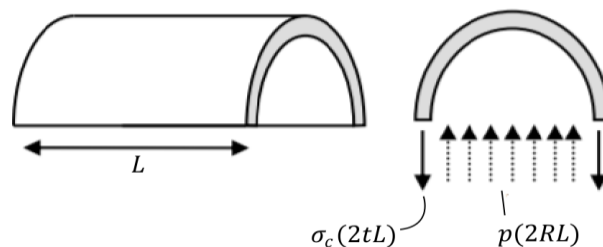


Figure 4-7: Free body diagram of a cylindrical pressure vessel in circumferential direction.

4.3 CLASSICAL LAMINATION THEORY

A composite structure is built up of layers of lamina. Composite material are heterogenous; the fiber and the matrix have different properties, and anisotropic; have different properties in different directions. Anyhow, the material is treated as macroscopically homogenous since the different properties between fibers and matrix is of no practical importance in design purposes [42].

A unidirectional lamina is an arrangement of parallel, continuous fibers, as shown in Figure 4-8. Because of symmetries, a unidirectional lamina is a so-called orthotropic material. As shown in Figure 4-8, the coordinate system is defined with respect to the fiber direction;

- Axis 1 is aligned with the fiber direction
- Axis 2 is perpendicular to axis 1, and lies in the plane of the layer
- Axis 3 is perpendicular to axis 1 and 2

The stress state of a 3D element is shown at Figure 4-9. The relationship between the stresses and strains for a unidirectional lamina are given by the generalized hooks law for orthotropic materials:

$$\begin{Bmatrix} \sigma_1 \\ \sigma_2 \\ \sigma_3 \\ \tau_{23} \\ \tau_{13} \\ \tau_{12} \end{Bmatrix} = \begin{bmatrix} C_{11} & C_{12} & C_{13} & 0 & 0 & 0 \\ C_{21} & C_{22} & C_{23} & 0 & 0 & 0 \\ C_{31} & C_{32} & C_{33} & 0 & 0 & 0 \\ 0 & 0 & 0 & C_{44} & 0 & 0 \\ 0 & 0 & 0 & 0 & C_{55} & 0 \\ 0 & 0 & 0 & 0 & 0 & C_{66} \end{bmatrix} \begin{Bmatrix} \varepsilon_1 \\ \varepsilon_2 \\ \varepsilon_3 \\ \gamma_{23} \\ \gamma_{13} \\ \gamma_{12} \end{Bmatrix} \quad (4.7)$$

$$\{\sigma\} = [C]\{\varepsilon\}$$

where [C] is called the stiffness matrix and contains the material constants. The above equation can be written in terms of strains:

$$\begin{Bmatrix} \varepsilon_1 \\ \varepsilon_2 \\ \varepsilon_3 \\ \gamma_{23} \\ \gamma_{13} \\ \gamma_{12} \end{Bmatrix} = \begin{bmatrix} \frac{1}{E_1} & -\frac{\nu_{21}}{E_2} & -\frac{\nu_{31}}{E_3} & 0 & 0 & 0 \\ -\frac{\nu_{12}}{E_1} & \frac{1}{E_2} & -\frac{\nu_{32}}{E_3} & 0 & 0 & 0 \\ -\frac{\nu_{13}}{E_1} & -\frac{\nu_{23}}{E_2} & \frac{1}{E_3} & 0 & 0 & 0 \\ 0 & 0 & 0 & \frac{1}{G_{23}} & 0 & 0 \\ 0 & 0 & 0 & 0 & \frac{1}{G_{13}} & 0 \\ 0 & 0 & 0 & 0 & 0 & \frac{1}{G_{12}} \end{bmatrix} \begin{Bmatrix} \sigma_1 \\ \sigma_2 \\ \sigma_3 \\ \tau_{23} \\ \tau_{13} \\ \tau_{12} \end{Bmatrix} \quad (4.8)$$

$$\{\varepsilon\} = [S]\{\sigma\}$$

where

E_1, E_2 and E_3 are the modulus of elasticity in the 1,2 and 3 directions

ν_{ij} are the Poisson's ratios given by $\nu_{ij} = -\frac{\varepsilon_j}{\varepsilon_i}$

G_{23}, G_{13}, G_{12} are the shear modulus in the 2-3, 1-3 and 1-2 planes.

Matrix $[S]$ in equation (4.8) is called the compliance matrix. From (4.7) and (4.8) we see that

$$[C] = [S]^{-1} \quad (4.9)$$

By use of Betti-Maxwell Reciprocal theorem, it can be shown that

$$S_{ij} = S_{ji} \quad (4.10)$$

From equations (4.8)-(4.10) the elements in the stiffness matrix are found:

$$\begin{aligned} C_{11} &= \frac{S_{22}S_{33} - S_{23}^2}{S}, & C_{12} &= \frac{S_{13}S_{23} - S_{12}S_{33}}{S}, & C_{13} &= \frac{S_{12}S_{23} - S_{13}S_{22}}{S}, \\ C_{21} &= C_{12}, & C_{22} &= \frac{S_{33}S_{11} - S_{13}^2}{S}, & C_{23} &= \frac{S_{12}S_{13} - S_{23}S_{11}}{S}, \\ C_{31} &= C_{13}, & C_{32} &= C_{23}, & C_{33} &= \frac{S_{11}S_{22} - S_{12}^2}{S}, \\ C_{44} &= \frac{1}{S_{44}}, & C_{44} &= \frac{1}{S_{44}}, & C_{44} &= \frac{1}{S_{44}} \end{aligned} \quad (4.11)$$

where

$$S = S_{11}S_{22}S_{33} - S_{11}S_{23}^2 - S_{22}S_{13}^2 - S_{33}S_{12}^2 + 2S_{12}S_{23}S_{13} \quad (4.12)$$

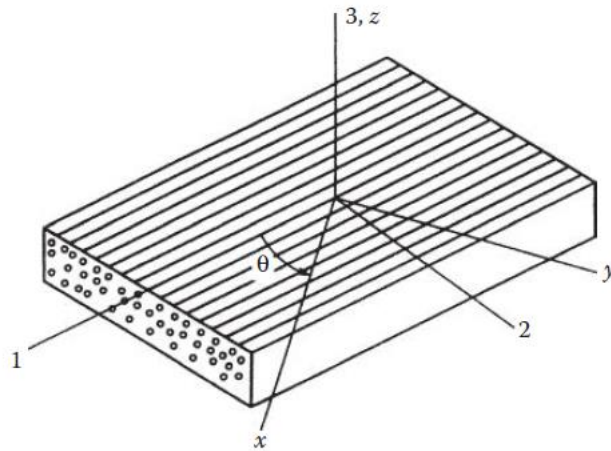


Figure 4-8: Unidirectional lamina with principal (123) and global (xyz) coordinate systems [43].

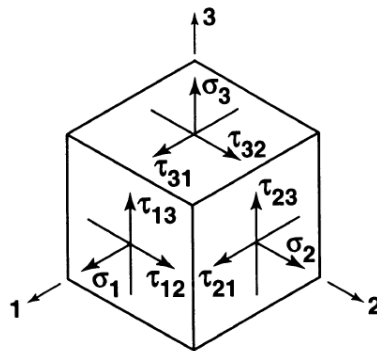


Figure 4-9: 3D-state of stress.

4.3.1 Plane stress

The laminas building up the laminate can often be assumed to be in the state of plane stress, which simplifies the analysis by letting $\sigma_3 = \tau_{13} = \tau_{23} = 0$. Equation (4.8) can now be simplified to

$$\begin{Bmatrix} \varepsilon_1 \\ \varepsilon_2 \\ \gamma_{12} \end{Bmatrix} = \begin{bmatrix} S_{11} & S_{12} & 0 \\ S_{21} & S_{22} & 0 \\ 0 & 0 & S_{66} \end{bmatrix} \begin{Bmatrix} \sigma_1 \\ \sigma_2 \\ \tau_{12} \end{Bmatrix} \quad (4.13)$$

where

$$\begin{aligned} S_{11} &= \frac{1}{E_1}, & S_{22} &= \frac{1}{E_2}, & S_{66} &= \frac{1}{G_{12}} \\ S_{12} &= S_{21} = -\frac{\nu_{12}}{E_1} = -\frac{\nu_{21}}{E_2} \end{aligned} \quad (4.14)$$

The lamina stresses in terms of strains can thus be written as

$$\begin{Bmatrix} \sigma_1 \\ \sigma_2 \\ \tau_{12} \end{Bmatrix} = \begin{bmatrix} Q_{11} & Q_{12} & 0 \\ Q_{21} & Q_{22} & 0 \\ 0 & 0 & Q_{66} \end{bmatrix} \begin{Bmatrix} \varepsilon_1 \\ \varepsilon_2 \\ \gamma_{12} \end{Bmatrix} \quad (4.15)$$

The elements Q_{ij} are called the reduced stiffnesses, and are given by

$$\begin{aligned} Q_{11} &= C_{11} - \frac{C_{13}^2}{C_{33}} = \frac{E_1}{1 - \nu_{12}\nu_{21}} \\ Q_{22} &= C_{22} - \frac{C_{23}^2}{C_{33}} = \frac{E_2}{1 - \nu_{12}\nu_{21}} \\ Q_{12} &= Q_{21} = C_{12} - \frac{C_{13}C_{23}}{C_{33}} = \frac{\nu_{12}E_1}{1 - \nu_{12}\nu_{21}} \\ Q_{66} &= G_{12} \end{aligned} \quad (4.16)$$

Now we have derived the stress-strain relationship with respect to the principal coordinate system (123-axes). As earlier stated, a laminate consists of multiple laminas (or layers), with potentially different orientations. Load subjected to the laminate have the same direction for all layers, and therefore the principal stresses and strains need to be expressed in terms of the global coordinate system (xyz-axes). The in-plane transformation matrix relating principal stresses to global stresses, and principal strains to global strains can easily be shown to be:

$$[T] = \begin{bmatrix} c^2 & s^2 & 2cs \\ s^2 & c^2 & -2cs \\ -cs & cs & c^2 - s^2 \end{bmatrix} \quad (4.17)$$

where $c = \cos \theta$ and $s = \sin \theta$, and θ is the angle between the principal axes of the layer and the global axes.

The principal stresses expressed in terms of global stresses are as follows:

$$\begin{Bmatrix} \sigma_1 \\ \sigma_2 \\ \tau_{12} \end{Bmatrix} = [T] \begin{Bmatrix} \sigma_x \\ \sigma_y \\ \tau_{xy} \end{Bmatrix} \quad (4.18)$$

And similarly for the strains:

$$\begin{Bmatrix} \varepsilon_1 \\ \varepsilon_2 \\ \frac{1}{2}\gamma_{12} \end{Bmatrix} = [T] \begin{Bmatrix} \varepsilon_x \\ \varepsilon_y \\ \frac{1}{2}\gamma_{xy} \end{Bmatrix} \quad (4.19)$$

With matrix algebra, and the aid of equations (4.15),(4.18) and (4.19) it can be shown that

$$\begin{Bmatrix} \sigma_x \\ \sigma_y \\ \tau_{xy} \end{Bmatrix} = [T]^{-1}[Q][T] \begin{Bmatrix} \varepsilon_x \\ \varepsilon_y \\ \gamma_{xy} \end{Bmatrix} \quad (4.20)$$

or written as

$$\begin{Bmatrix} \sigma_x \\ \sigma_y \\ \tau_{xy} \end{Bmatrix} = \begin{bmatrix} \bar{Q}_{11} & \bar{Q}_{12} & \bar{Q}_{16} \\ \bar{Q}_{21} & \bar{Q}_{22} & \bar{Q}_{26} \\ \bar{Q}_{16} & \bar{Q}_{26} & \bar{Q}_{66} \end{bmatrix} \begin{Bmatrix} \varepsilon_x \\ \varepsilon_y \\ \gamma_{xy} \end{Bmatrix} \quad (4.21)$$

where the elements \bar{Q}_{ij} are called the transformed reduced stiffnesses, and are given by

$$\begin{aligned} \bar{Q}_{11} &= Q_{11}c^4 + Q_{22}s^4 + 2(Q_{12} + 2Q_{66})c^4s^4 \\ \bar{Q}_{12} &= (Q_{11} + Q_{22} - 4Q_{66})c^2s^2 + Q_{12}(c^4 + s^4) \\ \bar{Q}_{22} &= Q_{11}s^4 + Q_{22}c^4 + 2(Q_{12} + 2Q_{66})c^4s^4 \\ \bar{Q}_{16} &= (Q_{11} - Q_{12} - 2Q_{66})c^3s - (Q_{22} - Q_{12} - 2Q_{66})cs^3 \\ \bar{Q}_{26} &= (Q_{11} - Q_{12} - 2Q_{66})cs^3 - (Q_{22} - Q_{12} - 2Q_{66})c^3s \\ \bar{Q}_{66} &= (Q_{11} + Q_{22} - 2Q_{12} - 2Q_{66})c^2s^2 + Q_{66}(c^4 + s^4) \end{aligned} \quad (4.22)$$

4.3.2 Mechanical behavior of composites

Until now, the derivation has only considered one layer. A composite structure is most often composed of N layers, and equation (4.21) can be seen as the stress-strain relation in the k^{th} layer, and can thus be written as:

$$\{\sigma\}_k = [\bar{Q}]_k \{\varepsilon\}_k \quad (4.23)$$

The layers composing the composite can have different orientations and thickness, and the stacking sequence can be varied, which are all influencing factors of the strength of the structure. To describe the mechanical behavior of a composite structure, classical lamination theory (CLT) will be used. The deformation hypothesis, equilibrium equations and strain-displacement relationships assumed in CLT are the same as for classical plate theory.

Deformation of the laminate is assumed to follow Kirchhoff deformation hypothesis, which states that normals to the middle plane remains straight under deformation. By use of this assumption, with aid of Figure 4-10, it can be shown that the deformation of a point located at a distance z from the mid surface in the x-z plane is:

$$u = u^0 - z \frac{\partial w^0}{\partial x} \quad \text{in } x - \text{direction} \quad (4.24)$$

where u^0 and w^0 is the horizontal and vertical displacement of the reference point O located on the mid surface, respectively, and $\frac{\partial w^0}{\partial x}$ are of the slope of the mid surface in x-direction.

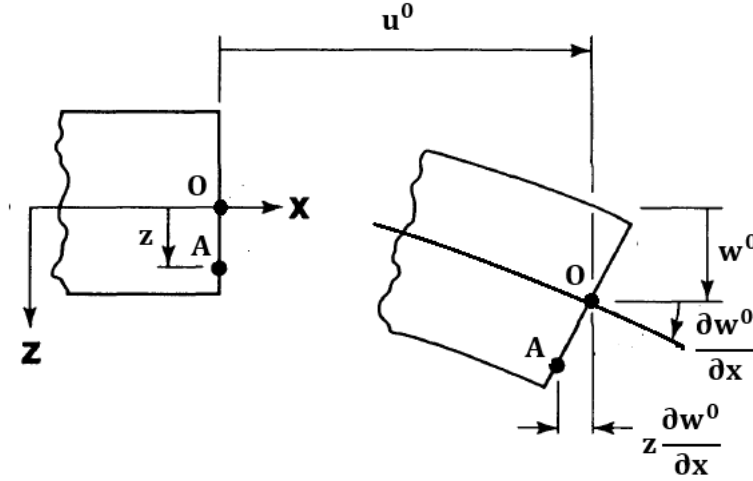


Figure 4-10: Deformation of a laminated plate in the x - z plane

Similarly, it can be shown that the deformation of a point in y - z plane can be expressed as:

$$v = v^0 - z \frac{\partial w^0}{\partial y} \quad \text{in } y \text{ - direction} \quad (4.25)$$

where v^0 is the horizontal displacement of a point on the mid surface and $\frac{\partial w^0}{\partial y}$ is the slope of the mid surface in y -direction.

Kirchhoff deformation theory also implies that $\gamma_{xz} = \gamma_{yz} = \varepsilon_z = 0$, and the relevant strain-deformation relations are given by:

$$\begin{aligned} \varepsilon_x &= \frac{\partial u}{\partial x} \\ \varepsilon_y &= \frac{\partial v}{\partial y} \end{aligned} \quad (4.26)$$

$$\gamma_{xy} = \frac{\partial u}{\partial y} + \frac{\partial v}{\partial x}$$

Substituting the displacement expressions given by (4.24) and (4.25) into the above equations (4.26), the laminate strains can be expressed as follows:

$$\begin{aligned} \varepsilon_x &= \frac{\partial u}{\partial x} = \varepsilon_x^0 + z\kappa_x \\ \varepsilon_y &= \frac{\partial v}{\partial y} = \varepsilon_y^0 + z\kappa_y \\ \gamma_{xy} &= \frac{\partial u}{\partial y} + \frac{\partial v}{\partial x} = \gamma_{xy}^0 + z\kappa_{xy} \end{aligned} \quad (4.27)$$

where the midplane strains are given by:

The laminate global coordinate system and the forces and moments per unit length are shown in Figure 4-12. The force per unit length directed along x-axis is given by:

$$N_x = \int_{-\frac{t}{2}}^{\frac{t}{2}} \sigma_x dz \quad (4.31)$$

and the moment per unit length is given by:

$$M_x = \int_{-\frac{t}{2}}^{\frac{t}{2}} \sigma_x z dz \quad (4.32)$$

where t is the laminate thickness.

Equation (4.30) is substituted in the above equations and rearranged:

$$\begin{aligned} N_x = & \left(\int_{-\frac{t}{2}}^{\frac{t}{2}} \bar{Q}_{11} dz \right) \varepsilon_x^0 + \left(\int_{-\frac{t}{2}}^{\frac{t}{2}} \bar{Q}_{12} dz \right) \varepsilon_y^0 + \left(\int_{-\frac{t}{2}}^{\frac{t}{2}} \bar{Q}_{16} dz \right) \gamma_{xy}^0 + \left(\int_{-\frac{t}{2}}^{\frac{t}{2}} \bar{Q}_{11} z dz \right) \kappa_x \\ & + \left(\int_{-\frac{t}{2}}^{\frac{t}{2}} \bar{Q}_{12} z dz \right) \kappa_y + \left(\int_{-\frac{t}{2}}^{\frac{t}{2}} \bar{Q}_{16} z dz \right) \kappa_{xy} \end{aligned} \quad (4.33)$$

$$\begin{aligned} M_x = & \left(\int_{-\frac{t}{2}}^{\frac{t}{2}} \bar{Q}_{11} z dz \right) \varepsilon_x^0 + \left(\int_{-\frac{t}{2}}^{\frac{t}{2}} \bar{Q}_{12} z dz \right) \varepsilon_y^0 + \left(\int_{-\frac{t}{2}}^{\frac{t}{2}} \bar{Q}_{16} z dz \right) \gamma_{xy}^0 \\ & + \left(\int_{-\frac{t}{2}}^{\frac{t}{2}} \bar{Q}_{11} z^2 dz \right) \kappa_x + \left(\int_{-\frac{t}{2}}^{\frac{t}{2}} \bar{Q}_{12} z^2 dz \right) \kappa_y + \left(\int_{-\frac{t}{2}}^{\frac{t}{2}} \bar{Q}_{16} z^2 dz \right) \kappa_{xy} \end{aligned} \quad (4.34)$$

By using the notation:

$$A_{ij} = \int_{-\frac{t}{2}}^{\frac{t}{2}} \bar{Q}_{ij} dz \quad (4.35)$$

$$B_{ij} = \int_{-\frac{t}{2}}^{\frac{t}{2}} \bar{Q}_{ij} z dz \quad (4.36)$$

$$D_{ij} = \int_{-\frac{t}{2}}^{\frac{t}{2}} \bar{Q}_{ij} z^2 dz \quad (4.37)$$

the force N_x and moment M_x per unit length can be written:

$$N_x = A_{11}\varepsilon_x^0 + A_{12}\varepsilon_y^0 + A_{16}\gamma_{xy}^0 + B_{11}\kappa_x + B_{12}\kappa_y + B_{16}\kappa_{xy} \quad (4.38)$$

$$M_x = B_{11}\varepsilon_x^0 + B_{12}\varepsilon_y^0 + B_{16}\gamma_{xy}^0 + D_{11}\kappa_x + D_{12}\kappa_y + D_{16}\kappa_{xy} \quad (4.39)$$

Equations (4.35)-(4.37) can be written in a simpler form:

$$A_{ij} = \sum_{k=1}^N \left(\int_{z_{k-1}}^{z_k} (\bar{Q}_{ij})_k dz \right) = \sum_{k=1}^N (\bar{Q}_{ij})_k (z_k - z_{k-1}) \quad (4.40)$$

$$B_{ij} = \sum_{k=1}^N \left(\int_{z_{k-1}}^{z_k} (\bar{Q}_{ij})_k z dz \right) = \frac{1}{2} \sum_{k=1}^N (\bar{Q}_{ij})_k (z_k^2 - z_{k-1}^2) \quad (4.41)$$

$$D_{ij} = \sum_{k=1}^N \left(\int_{z_{k-1}}^{z_k} (\bar{Q}_{ij})_k z^2 dz \right) = \frac{1}{3} \sum_{k=1}^N (\bar{Q}_{ij})_k (z_k^3 - z_{k-1}^3) \quad (4.42)$$

The other forces and moments per unit length are derived in the same manner. The equations are assembled in what is called the ABD-matrix or laminate stiffness matrix, which relates the forces and moments per unit length to the midplane strains and curvatures, respectively. The ABD-matrix is expressed as follows:

$$\begin{Bmatrix} N_x \\ N_y \\ N_{xy} \\ M_x \\ M_y \\ M_{xy} \end{Bmatrix} = \begin{bmatrix} A_{11} & A_{12} & A_{16} & B_{11} & B_{12} & B_{16} \\ A_{12} & A_{22} & A_{26} & B_{12} & B_{22} & B_{26} \\ A_{16} & A_{26} & A_{66} & B_{16} & B_{26} & B_{66} \\ B_{11} & B_{12} & B_{16} & D_{11} & D_{12} & D_{16} \\ B_{12} & B_{22} & B_{26} & D_{12} & D_{22} & D_{16} \\ B_{16} & B_{26} & B_{66} & D_{16} & D_{16} & D_{66} \end{bmatrix} \begin{Bmatrix} \varepsilon_x^0 \\ \varepsilon_y^0 \\ \gamma_{xy}^0 \\ \kappa_x \\ \kappa_y \\ \kappa_{xy} \end{Bmatrix} \quad (4.43)$$

or in reduced form as

$$\begin{Bmatrix} N \\ M \end{Bmatrix} = \begin{bmatrix} [A] & [B] \\ [B] & [D] \end{bmatrix} \begin{Bmatrix} \varepsilon^0 \\ \kappa \end{Bmatrix} \quad (4.44)$$

The extensional stiffness matrix [A] relates the forces to the midplane strains, the bending stiffness matrix [D] relates the moments to the curvatures and the coupling stiffness matrix [B] relates the forces to the curvatures, and the moments to the midplane strains.

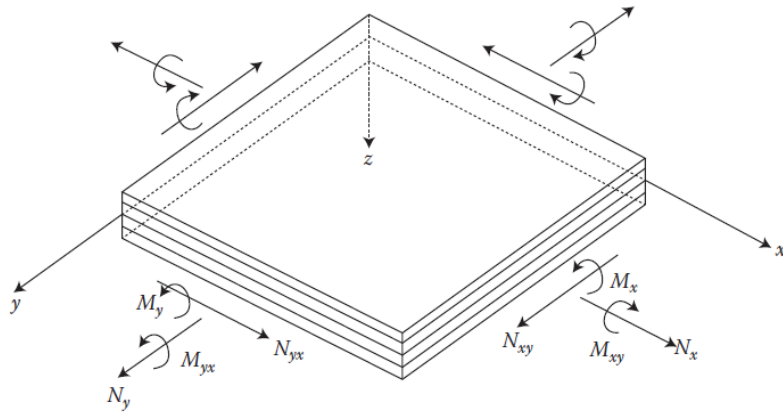


Figure 4-12: Applied forces and moments per unit meter in global coordinate system [43].

4.4 TSAI-WU FAILURE CRITERION

As with the elastic properties, the strength of a lamina varies with orientation. The strength for a unidirectional lamina is characterized by 5 strength parameters:

- σ_1^T : Tensile strength along the fibers (in the direction of axis 1)
- σ_1^C : Compressive strength along the fibers (in the direction of axis 1)
- σ_2^T : Tensile strength transverse of the fibers (in the direction of axis 2)
- σ_2^C : Compressive strength transverse of the fibers (in the direction of axis 2)
- τ_{12}^F : Shear strength (in the 1-2 plane)

There exist many failure criteria for composite materials, but for design purposes, the Tsai-Wu criterion seems like one of the most popular [42]. For the case of plane-stress, the Tsai-Wu criterion is given by the following expression:

$$F_1\sigma_1 + F_2\sigma_2 + F_{11}\sigma_1^2 + F_{22}\sigma_2^2 + F_{66}\tau_{12}^2 - \sqrt{F_{11}F_{22}}\sigma_1\sigma_2 \leq 1 \quad (4.45)$$

where

$$F_1 = \frac{1}{\sigma_1^T} - \frac{1}{\sigma_1^C} \quad (4.46)$$

$$F_2 = \frac{1}{\sigma_2^T} - \frac{1}{\sigma_2^C} \quad (4.47)$$

$$F_{11} = \frac{1}{\sigma_1^T \sigma_1^C} \quad (4.48)$$

$$F_{22} = \frac{1}{\sigma_2^T \sigma_2^C} \quad (4.49)$$

$$F_{66} = \frac{1}{\tau_{12}^F{}^2} \quad (4.50)$$

The compressive strengths in the above equations are assumed to be positive. The model predicts failure when the left-hand side of equation (4.45) is larger than 1.

4.5 SAFETY FACTOR

Design of most structures are based on approximate formulas, material properties that varies within a range, and environmental behavior that is somewhat uncertain. The lacking knowledge must be compensated for by a safety factor, which for a pressure vessel is the ratio between the burst pressure and the design pressure [41]:

$$SF = \frac{p_{burst}}{p_{design}} \quad (4.51)$$

If a low safety factor is to be used, increased knowledge is necessary. Knowledge is expensive, but so are also the increased material cost because of a higher safety factor. Most often a balance between knowledge and safety factor is found. But in the case of a pressure vessel designed for a UAV where weight is critical, very low safety factors are needed. In this case the cost of additional knowledge is essential. ASME pressure vessel code, Section VIII, Division 3: Alternative rules for construction of high pressure vessels, shows that a safety factor of 2 can be justified if certain requirements are fulfilled:

- In addition to static analysis, also fracture mechanics and fatigue analyses are made
- Extended material qualifications are performed
- Fabrication quality control
- Periodic in-service examination

This design code has no upper or lower pressure limits but are normally used for design pressure of 10000 psi. Composite materials are not included in this code though[41].

There are several standards prescribed by American National Standards Institute (ANSI) and International Organization for Standardization (ISO) that can be used to design a composite pressure vessel [40]:

- ANSI NGV2: Compressed natural gas vehicle fuel containers
- ISO 11439: Gas cylinders – high pressure cylinders for the onboard storage of natural gas as fuel for automotive vehicles
- ISO 11119-3: Gas cylinders – refillable composite gas cylinders and tubes. Part 3: fully wrapped fiber reinforced composite gas cylinders and tubes up to 450 L with non-load sharing metallic or non-metallic liners.

The safety factors from the above-mentioned standards for different materials are given in Table 4-2.

Table 4-2: Safety factors for COPV pressure vessels in different standards

	Type III			Type IV		
	ANSI NGV2	ISO 11439	ISO 11119-3	ANSI NGV2	ISO 11439	ISO 11119-3
Carbon	2.25	2.35	2.00	2.25	2.35	2.00
Glass	3.50	3.65		3.50	3.65	
Aramid	3.00	3.10		3.00	3.10	

The safety factor influences the thickness, weight and cost of the pressure vessel. In the industry the safety factor in current standard ISO 11119-3 is perceived as too high. A problem is that there are no scientific reasoning behind the safety factor, and therefore the use of a lower safety factor is difficult to evaluate for larger pressure vessels at higher pressure.

Another method that can be used to find the right safety factor is by a probabilistic approach. A study by Echtmeyer and Lasn [44, 45] describes such a method by extending the methods used in DNV Offshore Standard DNV-05-C501 “composite components”. The study is based on road transport of hydrogen, and the safety factor is calculated from the annual probability of failure and the coefficient of variance (COV) of the material properties.

The acceptable probability of failure must agree with the maximum consequence of an accident. For a pressure vessel, burst failure due to laminate failure is the most critical failure mechanism. In a burst, all the hydrogen is almost immediately released. Hydrogen has a buoyant nature, and disperses quickly, but due to the very low ignition energy, it can ignite and explode in the worst case. The consequence of a severe accident increases with hydrogen mass. In the study by Echtmeyer and Lasn, the acceptable probability of failure is determined based on the stored hydrogen mass, and a social criterion. They conclude that an acceptable annual probability of failure is 10^{-7} for small pressure vessels containing a few kilograms of hydrogen. In comparison, acceptable probability of failure in other industries such as aerospace, marine or civil engineering structures varies from 10^{-4} to 10^{-6} per year.

The coefficient of variance of material properties is defined as the standard deviation divided by the mean strength, and is a measure of the quality of the material and the production. The choice of safety factor is largely influenced by the COV. The COV is lowered when high material quality is used, and the production parameters are well known. To determine the COV, extensive testing is needed. In the case of static burst, burst tests are performed by internally pressurizing the vessel at a constant rate until it fails. The more pressure tests that are performed, the lower the COV. For static burst the safety factors for different values of COV are shown in Table 4-3.

Table 4-3: Safety factors for different values of COV, with an annual probability of failure of 10^{-7}

Probability of failure	COV≤5%	COV=10%	COV=12.5%	COV=14%
10^{-7}	1.22	1.67	2.16	3.21

4.6 FAILURE MECHANISMS

Above only the static burst failure was considered in the determined safety factors. This is the most critical failure mode, but in a full design analysis of a composite pressure vessel other failure modes must also be considered:

- Fatigue
- Static stress rupture
- Matrix cracking
- Delamination
- Liner and boss failure

4.7 LINER

In a type IV pressure vessel the liner’s function is to prevent gas leakage, but it does not carry any structural load. The liner material must be compatible with the other materials of the pressure vessel and the gas that is stored in the pressure vessel. ISO 11114-2: *Transportable gas cylinders - Compatibility of cylinder and valve materials with gas contents* shows which materials are suitable for hydrogen storage. For type IV pressure vessels high density polyethylene (HDPE) is a commonly used liner material. A frequently used manufacturing method for the liner is the rotomolding technique. This method allows production of complex shapes at a low cost, and the liner

reaches high impact strength compared to injection or blow molding methods [46], and hence seems ideal for the manufacturing of a spherical liner.

The liner thickness must be determined according to the permeation rate. ISO 11439 requires that the permeation rate shall be less than 0.25 ml of natural gas per hour per liter water capacity of the pressure vessel. Permeation and diffusion coefficients can be determined through experimental tests, and leak rate can be predicted by Fick's law, as described in ref. [47]. Anyhow, this is beyond the scope of this thesis.

In two studies of performance assessment of compressed hydrogen storage by Hua et. al [48, 49], a HDPE liner thickness of 5 mm was used for a 350 and 700 bar type IV pressure vessel. This was based on inputs from the industry and U.S Department of Energy (DOE). Anyhow, the tanks considered in that study was of several hundred liters.

Another important aspect of determining liner thickness is depressurization-induced blistering that can occur in plastic liners. Hydrogen is absorbed by the liner material at high pressures, and if the depressurization rate exceeds the rate of which hydrogen can escape the material, blistering occurs. Blistering is characterized by liner cracking and /or whitening. In design of a plastic liner there is a balance between wanting a thin enough liner to avoid blistering and a thick enough liner to prevent permeation and liner buckling. In a study by Yersak et al. [50] where a predictive model for depressurization-induced blistering where developed, they found that a liner thickness of 2 mm or less is needed to avoid blistering at depressurization rates of 30 MPa/h or lower for HDPE liner. For a 3 mm liner, blistering was possible at this depressurization rate. The developed model agreed well with experiments.

5 FUEL CELL – BATTERY HYBRID SYSTEM COMPONENT SIZING AND SELECTION

In the coming sections, a justification for the selection of technology for the different subsystems is made. The mission profile is represented and forms the basis for the power requirement calculations. The selection of fuel cell and battery is based upon these power estimates. But first the existing system is represented.

5.1 EXISTING SYSTEM

The Camflight FX8 (Figure 5-1) is actuated by 8 propellers arranged in 4 coaxial pairs and has energy storage in the form of LiPo batteries. The current technical specifications for the Camflight are as follows:

Physical dimensions

Size: 140 cm width and 50.5 cm high
MTOW: 25 kg
Maximum velocity: 40 km/h
Primary equipment: LIDAR

Components

8xBrushless motors

Type: KDE7215XF-135 Kv
Configuration: Coaxial
Maximum continuous power: 4405 W

Propellers

Diameter: 29"
Slope: 9.5L

4xLiPO batteries

Nominal voltage: 29.6 V
Fully charged voltage: 32.8 – 33.6 V
Capacity per battery: 11000 mAh

Flight time (weather dependent)

50 min with 1.5 kg payload
25 min with 5 kg payload

Environmental limitations:

Maximum wind: 10 - 12 m/s
Humidity/rain: Drizzling rain (0,1-0,5 mm/h)
Temperature: -20 °C to 40 °C

Operating crew

Compulsory: Operator/pilot
If demanded: Additional ground personnel for observation



Figure 5-1: Camflight FX8HL multirotor UAV.

As seen from the technical specifications the flight time of 50 min with 1.5 kg payload is not very impressive. When the payload increases the flight time goes further down, and at MTOW the flight time is between 20-25 min. With replacing the current LiPo batteries with a fuel cell-battery hybrid system, Nordic Unmanned wants to reach a flight time of 3 hours at MTOW. The target specifications for the design process are given in Table 5-1.

Table 5-1: Target specifications.

MTOW	25 kg
- System weight	10 kg
-Payload	5 kg
-Fuel cell/battery hybrid system	10 kg
Flight time	3 h

The system weight includes the weight of the frame, motors, and propellers. The payload of 5 kg is of the LIDAR system which is intended for the UAV. The LIDAR system is stand-alone, and the weight includes the batteries which are used to power the LIDAR.

From Table 5-1 we see that the fuel cell-battery hybrid system has a weight limitation of 10 kg in order to stay within the MTOW. From this we can formulate a preliminary goal for the design process:

Implement a fuel cell – battery hybrid solution to the Camflight FX8. The propulsion system should be maximum 10 kg and provide 3 h flight time.

5.2 PROPULSION SYSTEM COMPONENTS

The fuel cell - battery hybrid propulsion system consists of several components; motors, propellers, fuel cell, battery, hydrogen storage and different monitoring and control systems. The focus in this thesis was to select the best solution for the different components based on the technology that is available. Figure 5-2 shows a concept tree of the components/subsystems that make up the propulsion system. Below is a short review of the selection of technology for different components/subsystems, before a detailed review and calculations will be given in the subsequent sections.

5.2.1 Type of fuel cell

In section 3.3 the different type of fuel cells for UAV applications was represented. It is quite obvious that the PEMFC is the only fuel cell that is currently suited for propulsion of a VTOL UAV because of the high power demand. PEMFC is the fuel cell with the highest specific power and it have additional advantages such as low operating temperature, high efficiency, fast start and compactness. The other types of fuel cells (SOFC and DMFC) have been implemented on fixed-wing UAVs with variable luck.

For UAV applications, the PEMFC should be made of lightweight and compatible materials, and BOP components should be kept simple to minimize weight without sacrificing much of the efficiency.

5.2.2 Hydrogen storage

Selecting hydrogen storage method is more difficult because all the three methods described in section 3.7 can potentially be used. The three storing methods considered have different advantages and drawbacks. To make the decision easier, a concept-scoring matrix is made, shown in Table 5-2. The concepts are evaluated by specific energy, practicality, maturity of technology, simplicity of system and safety. The different criteria are weighted with relative importance.

The storage method with the highest score is compressed gas. This seems reasonable as the method compromises between specific energy and practicality, which were the criteria with highest weighting. It is also the most frequently used method for storing hydrogen in UAV applications. Compressed gas is therefor selected as hydrogen storage method.

Table 5-2: Concept scoring-matrix for hydrogen storage. The criteria are weighted with relative importance.

Criterion	Weight	Compressed gas		Liquid		Chemical	
		Rating	Weighted score	Rating	Weighted score	Rating	Weighted score
Specific energy[Wh/kg]	40 %	4	1,6	5	2	1	0,4
Practicality	30 %	3	0,9	1	0,3	5	1,5
Technology maturity	20 %	5	1	2	0,4	3	0,6
System simplicity	10 %	5	0,5	4	0,4	3	0,3
Safety	10 %	3	0,3	4	0,4	4	0,4
Total score			4,3		3,5		3,2

5.2.3 Battery type

Based on the discussion of different battery types in chapter Table 2-1, the currently most suited battery for this application is the LiPo battery. The LiPo battery offers relative high specific energy, and it can also withstand many cycles, which is necessary for this use because it is continuously going to be charged and discharged during operation.

5.2.4 Motor and propellers

The motor used for this application is the brushless DC motor, which offers high efficiency (typically 85-90 %), high specific power and quick response. Regarding the propellers, the incentives are high for large propellers because the generated thrust is increasing with propeller size.

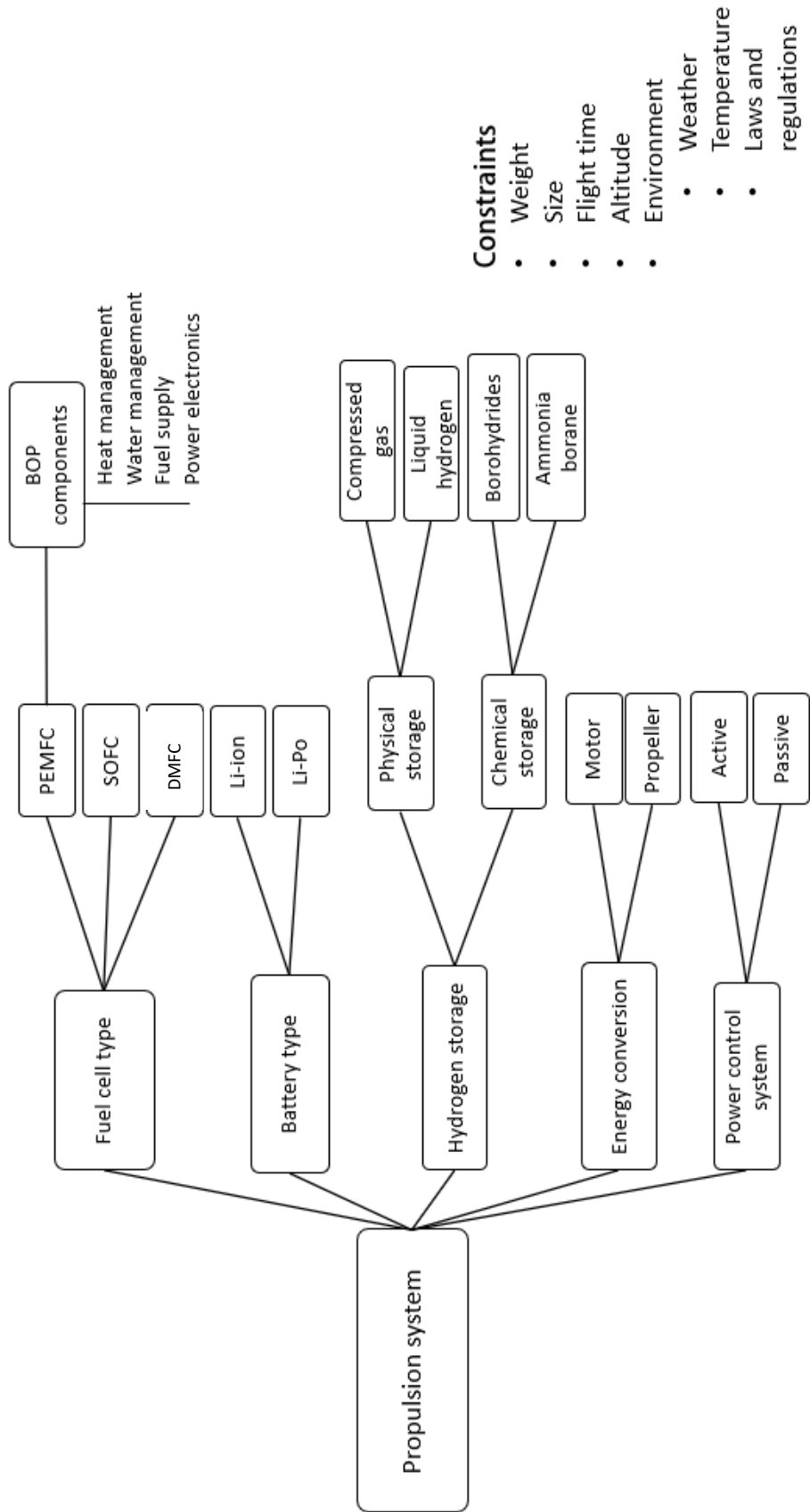


Figure 5-2: Concept tree of propulsion system.

5.3 MISSION PROFILE

A mission profile is needed to do further calculations. According to pilots at Nordic Unmanned, typical flight altitude for the Camflight is between 60-120 meters, normally 60 meters when equipped with LIDAR. For a smooth climb phase, the vertical velocity is around 3-4 m/s. When doing missions with LIDAR the forward speed is approximately 5-6 m/s, because the quality of the collected data gets poor when forward speed is higher. For simplicity, the air is assumed to be still, and the UAV is flying in one direction only. Additionally, the acceleration is assumed to be zero during the whole mission. This gives the mission profile shown in Figure 5-3, which is the basis for calculations of power requirements in the subsequent chapters. The descent phase is not considered in the calculations because the power requirement during this phase are less than in the climb phase.

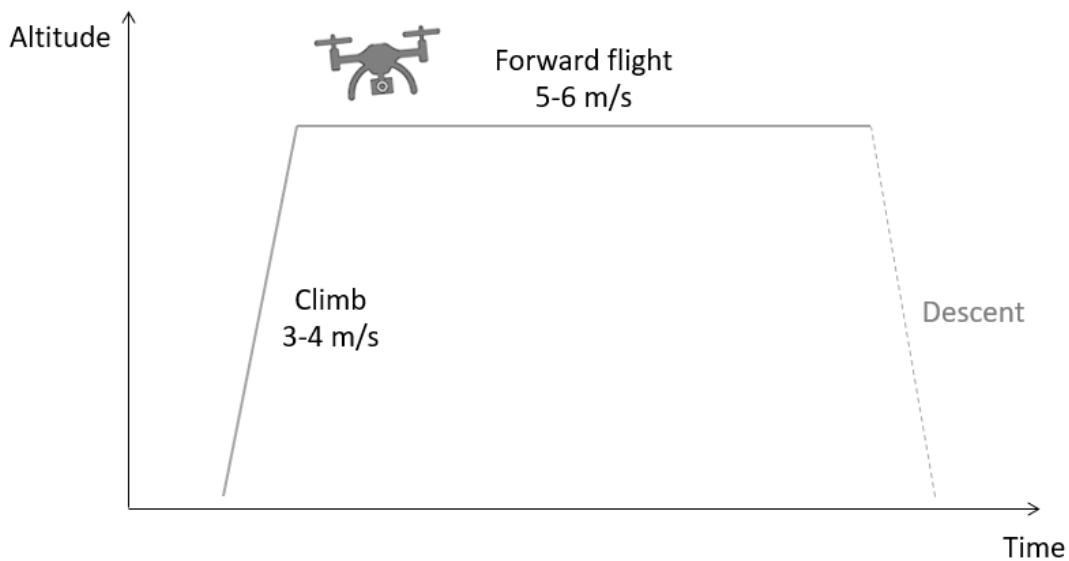


Figure 5-3: Mission profile.

5.4 SELECTION OF MOTORS

The brushless motors that is already installed on the Camflight come from a leading supplier of high quality motors for UAVs, namely KDE direct, and are correct dimensioned for a MTOW of 25 kg. Anyhow, since the marginals are small for successfully integrate a fuel cell system, a comparison between the current installed motor and comparable motors from the same supplier and from T-motor, will be done. T-motor is another well-known company for producing high quality motors. The comparison will be made on the basis of the technical data available at the companies' websites [51, 52]. Table 5-3 shows the key specifications of the four considered motors. Both KDE motors are in a higher price range than the two T-motors, and KDE 8218 and T-motor U12 are larger than the other two motors that is considered.

The efficiency of the motor and propeller is often expressed in generated thrust per power consumed [g/W]. Figure 5-4 shows thrust vs. power for the four motors. All the motors are tested at approximately 30 V, the KDE motors are tested with 30.5" propeller blades, while T-motor U10 are tested with 30" propeller blades, and T-motor U12 with 32" propeller blades. The lifting force needed per motor is $25\text{kg}/8=3125\text{ g}$. In the lower range (below approximately 5000 g thrust), Figure 5-4 shows that both KDE motors have better performance than the T-motors. It is in the lower range that the UAV will spend most of the time, which makes the KDE motors most suited.

Table 5-3: Specifications of the considered brushless DC motors

Motor	KDE 7215	KDE 8218	T-motor U10 plus	T-motor U12
Kv [Rpm/V]	135	120	100	100
Weight [g]	555	760	500	789
Voltage range [V]	22.2-60.9	22.2-60.9	22.2-51.8	22.2-51.8
Propeller blade size [inch]	24.5-30.5	27.5-30.5	26-30	26-34
Max continous power (180s) [W]	4405	5695	1700	2500
Max continous current (180s) [A]	55	110	36	50
Configuration	24S22P	24S28P	36N40P	36N40P
Maximum Efficiency, %	>93	>94		
Price (\$)	373.95	596.95	339.9	349.9

When selecting motors, it is common to select one that can hover at 50 % throttle, such that the propulsion system has excess resources for the climb phase, maneuvering and wind. Figure 5-5 shows thrust vs throttle, and we see that at thrust of 3125 g, the KDE motors are at about 45 % throttle and the T-motors are at about 60 % throttle, which also favor the KDE motors. Furthermore, Table 5-4 shows the efficiency of the motors in hover, and the KDE 7215 have the highest efficiency of all. The difference between the performance of KDE 7215 and KDE 8218 are small, but considering the extra cost and weight of KDE 8218, the current installed motors (KDE 7215) seems by far as the best choice. It is therefore decided to keep the current installed motors.

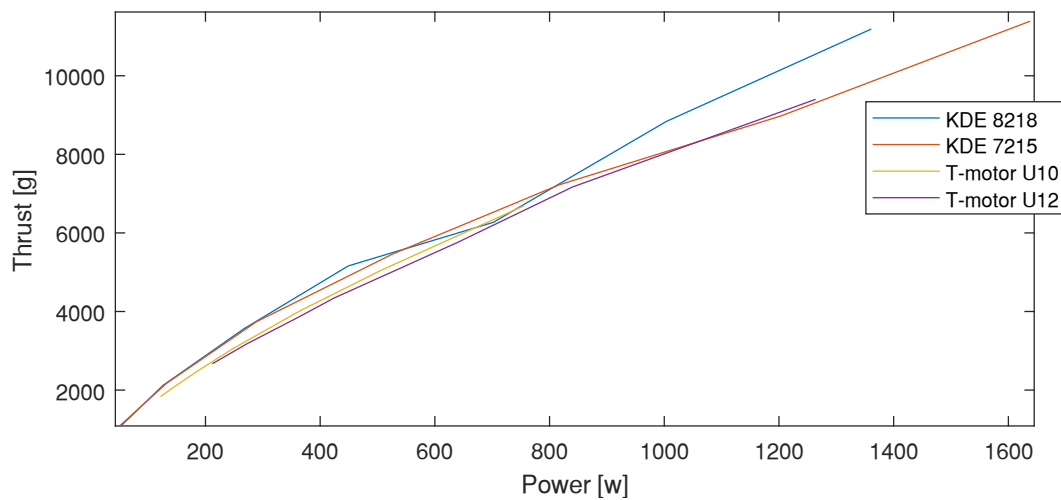


Figure 5-4: Motor performance - thrust vs. power.

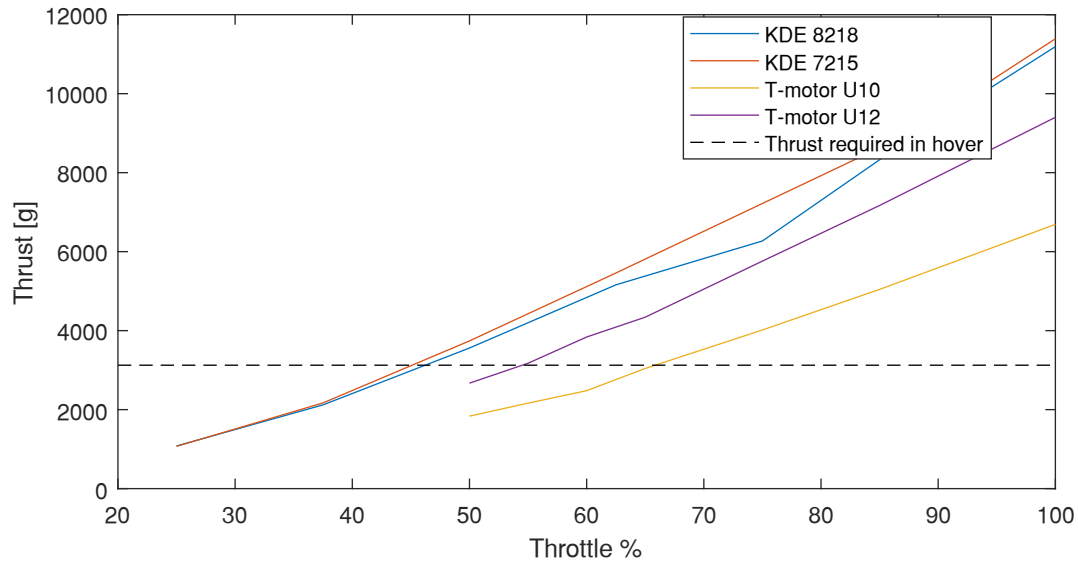


Figure 5-5: Thrust vs. throttle.

Table 5-4: Efficiency in hover at thrust of 3125 g per motor.

	KDE 7215	KDE 8218	T-motor U10 plus	T-motor U12
Efficiency in hover [g/W]	13.9	13.7	12.2	12.55

5.4.1 Electric speed controllers (ESC)

ESCs are needed to control and regulate the speed of the motors. The speed is controlled by changing the timing of the ampere pulses that is delivered to the motor windings. It is decided to stick with KDE ESCs to avoid any interface issues. For KDE 7215 motor the recommended ESC is KDEXF-UAS95HVC. This ESC is optimized and tuned for the KDE motor, which allows simple plug-and-play operation. The specifications of the ESC are given in Table 5-5.

Table 5-5: Specifications of KDEXF-UAS95HVC ESC

Voltage Range	11.1 V - 52.2 V
Maximum Efficiency	> 98%
Maximum RPM	360,000 rpm
ESC Size	37 mm (W) x 82 mm (L)
ESC Weight	78 g
Maximum Continuous Current (180 s)	95 A
Maximum Continuous Power (180 s)	4,220 W

5.5 POWER REQUIREMENT CALCULATIONS

In this section, the power required in hover, vertical climb and forward flight is calculated based on momentum theory which was derived in section 2.2. The air density in all the calculations are taken to be 1.225 kg/m^3 , which is the air density at sea level at 15°C . The air density is decreasing with altitude, but at 60 m, the change is very small, and so is neglected in the calculations.

5.5.1 Power in hover

Since the MTOW is known, the first step is to calculate the power requirements. Figure 5-6 shows the relation between power and rotor diameter at a thrust of 25 kg according to equation (2.8).

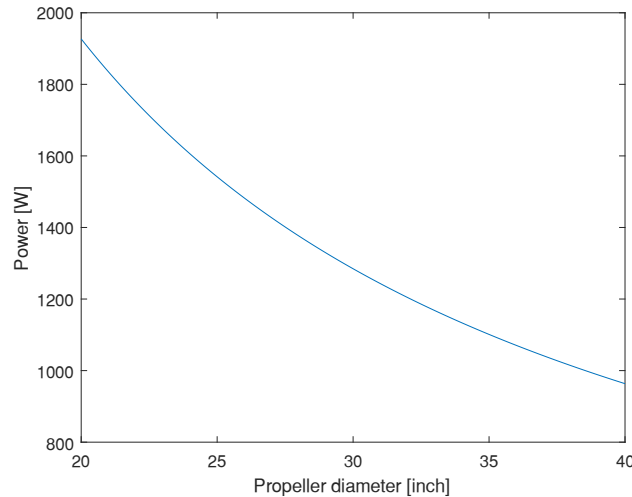


Figure 5-6: Theoretical power as a function of diameter at MTOW of 25 kg.

As seen from the figure, the power requirement decreases with increasing propeller diameter. By doubling the propeller diameter from 20 to 40 inches, the power requirement is approximately halved. For successfully implementing a fuel cell system to the high power demanding device that a VTOL is, the incentives are high to keep the propeller diameter large. Large propeller diameter goes at the expense of maneuverability and response, but as the Camflight X8 is a quite large UAV, and missions with LIDAR will not require quick movements, this is not a big issue. For the selected motor (KDE 7215), the largest possible diameter is 30.5 inches. This is also approximately the largest possible diameter with the current design of the Camflight considering the length of the arms which supports the rotors. The theoretical power requirement in hover with thrust of 25 kg, and 30.5 inches propeller blades is calculated according to equation (2.8) which yields 1264 W. This is without any losses in the propeller blades or the motors. Figure 5-7 shows the thrust output vs power input for the KDE 7215 motor. The graph is linear interpolated between data points from the supplier. At thrust of 25 kg, each of the eight motors plus propellers supplies 3125 g. By linear interpolation between the two data points, we get that each motor requires 223 W, which gives 1784 W in total for the eight motors. Now the efficiency of the motors plus propellers can be calculated:

$$\eta_{motor+propeller} = \frac{\text{Theoretical power requirement}}{\text{Actual power requirement}} = \frac{1264 \text{ W}}{1784 \text{ W}} = 0.71$$

where

$$\eta_{motor+propeller} = \eta_{motor} \cdot \eta_{propeller}$$

The efficiency of the motor + propeller is 71 %. Compared to values of efficiency of well-designed motors of 85 to 90%, and maximum figure of merit between 0.74 to 0.78 for well-designed propeller, the calculated efficiency of 71% seems reasonable.

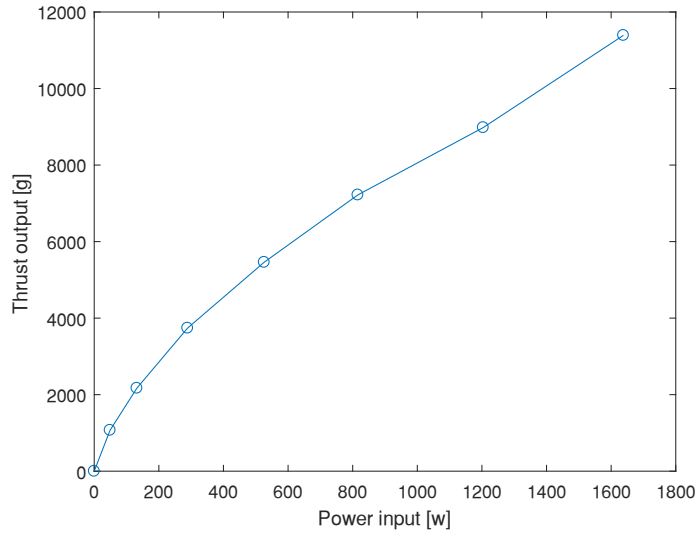


Figure 5-7: Thrust output vs. power input for the KDE 7215 motor.

Furthermore, as explained in section 2.2.4, propellers in coaxial configuration requires additional power. The additional power requirement for the same amount of thrust is taken to be 22 %, which is the theoretical additional power for coaxial propellers when the lower propeller is in the ‘far wake’ of the upper. With this additional power requirement, the total power needed in hover is 2176 W:

$$1784 \text{ W} \cdot 1.22 = 2176 \text{ W}$$

5.5.2 Power consumption in vertical climb

The power required in vertical climb is given by equation (2.14) and (2.15). With a climb speed of 3 m/s, and assuming a motor plus propeller efficiency of 0.7 as for hover and additional power requirements of 22 % for the coaxial configuration, the power requirement in climb is 2894 W. If the climb speed increases to 4 m/s the power requirement is 3172 W. Figure 5-8 shows the total power, the induced power and the climb power as a function of climb speed. As the climb speed increases, the induced power reduces, and approaches zero at high climb speeds. At high speeds the required power approaches the climb power given by $P_c = TV_c$.

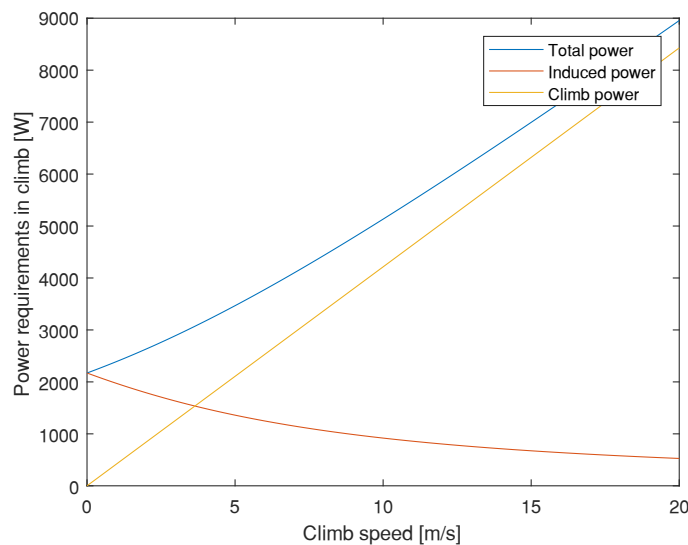


Figure 5-8: Power required in climb as a function of climb speed

5.5.3 Power consumption in forward flight

For calculating the required power in forward flight, an estimate of the drag needs to be made. Most preferably would be to do a CFD analysis to find the drag coefficient of the Camflight and/or wind tunnel testing. Currently, there are no 3D-models of the Camflight suited for CFD analysis, so the drag force is estimated according to the method with finding the equivalent wetted or flat plate area described in section 2.2.5. Wind-tunnel testing of the different components is beyond the scope of this thesis, so the UAV is simplified to geometries which have known drag coefficient, as shown in Figure 5-9. The dimensions of the different parts that make up the UAV together with associated drag coefficients and reference areas are given in Table 5-6. The drag coefficients are found in ref. [53]. By equation (2.27) the equivalent flat plate area f is calculated to 0.2736 m². With a forward flight speed of 5 m/s the drag force is calculated according to equation (2.28) to be 4.2 N.

Table 5-6: Drag coefficients for the components that make up the UAV

Component	Number of parts	Shape	Reference area, S [cm]	Drag coefficient, Cd
Fuel cell	1	Rectangular box	20x12	2.1
Platform	1	Rectangular box	35x3	2.1
Lidar	1	Rectangular box	20x10	2.1
Arms	4	Finite cylinder	36x3	0.9
Legs	4	Finite cylinder	48x1.8	0.95
Motors	4	Square	10x10	1.05
Pressure vessel	1	Sphere	$\pi 17^2$	0.5

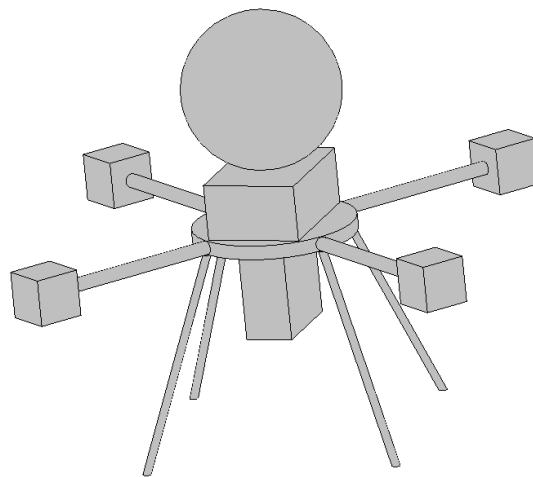


Figure 5-9: Simplified model of the UAV used as a basis for estimation of drag coefficient, the different components are to scale.

The only forces acting on the UAV in vertical flight are the drag force and the gravitational force, as shown in Figure 5-10. The required thrust to overcome these forces are calculated by vector addition. When the thrust is known, the induced velocity can be calculated with the aid of equation (2.20). A forward speed of 5 m/s gives a power requirement of 1755 W, and a forward speed of 6 m/s gives 1630 W, according to equation (2.21). These numbers assume the same efficiency for the motor plus

propeller as in hover, and that the coaxial configuration gives additional power requirement of 22%. The total power is probably a little higher than calculated, because the profile power is slightly increasing with forward speed. But the forward speeds considered here is relatively small, so the same profile power as in hover is assumed.

The power requirement was also calculated for different forward speeds, as shown on Figure 5-11. At zero forward speed the power requirement is the same as in hover. We see that the induced power is decreasing with forward speed. This is explained by the increased air flow through the rotor disc at higher speeds. We also see that the parasitic power increases with forward speed. The reason is that the drag force increases with the cube of the forward speed. From the figure we see that the minimum power requirement is at approximately 11 m/s. Compared to Figure 2-5 of power for helicopter in forward flight, this minimum happens at a lower speed. The reason is the higher drag coefficient of the multirotor UAV compared to the aerodynamic design of a typical helicopter.

Ideally the best would be to fly at 11 m/s. In practical missions with LIDAR however, this is not possible because the LIDAR cannot do terrain mapping at such speeds.

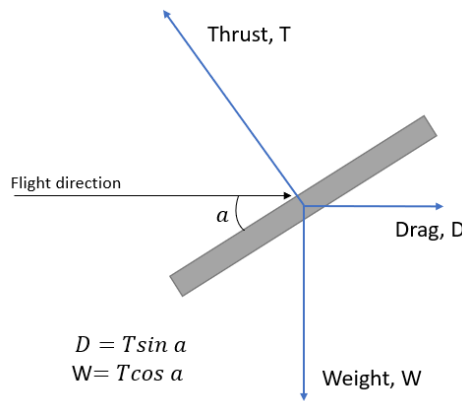


Figure 5-10: Forces acting on a rotor disc in forward flight.

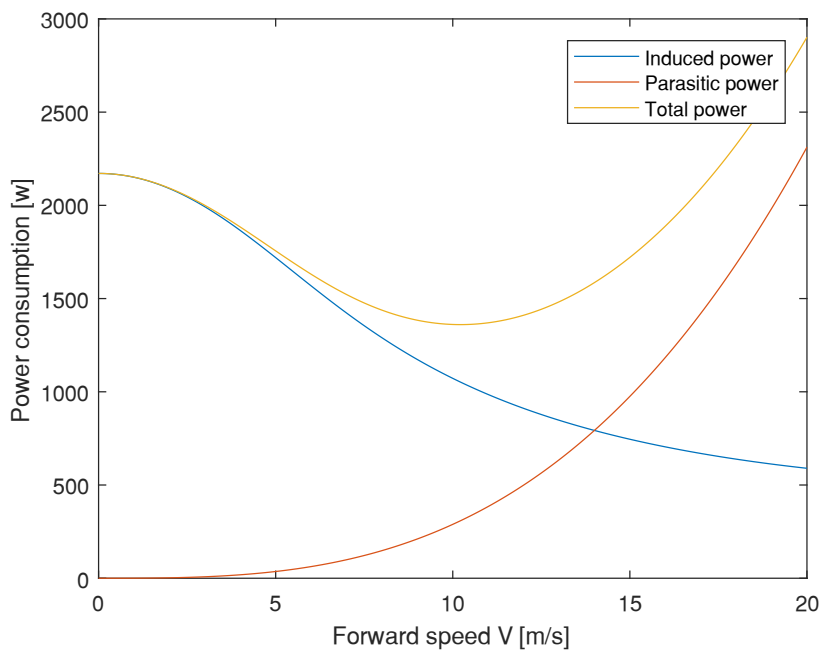


Figure 5-11: Power consumption as a function of forward speed

5.5.4 Summary of power requirements

The power required in hover, climb and forward flight is summarized in Table 5-7.

Table 5-7: Summary of power requirements according to the mission profile

	Hover	Climb		Forward flight	
Speed [m/s]	0	3	4	5	6
Power [W]	2175	2894	3172	1755	1630

As discussed in chapter 3.10, a common hybridization scheme is to size the fuel cell according to the power needed in hover. In a mission with lidar though, the UAV spends most of the time in forward flight and doing maneuvers to change flight direction. The required power in forward flight is therefore used as the basis when sizing the fuel cell.

Since the forward flight power is probably a little higher than predicted, and that the fuel cell must provide some additional power to charge the battery after peak powers such as in the climb phase and in maneuvering, the power requirement of the fuel cell is set to 2000 W. This gives approximately 10 % excess power in forward flight at 5 m/s.

To check if this power is realistic we can compare with the currently installed LiPo batteries. The total stored energy is calculated according to equation (2.30):

$$44 \text{ Ah} \cdot 29.9 \text{ V} = 1316 \text{ Wh}$$

The batteries are discharged 70 % to prevent damage to the batteries, which gives a usable energy of 921 Wh.

With a power consumption of 2000 W, the flight time will be:

$$\frac{921 \text{ Wh}}{2000 \text{ W}} = 0.46 \text{ h} = 27.6 \text{ min}$$

Compared to the reported flight time of 20-25 min, this seems reasonable as the additional power for hover, climb, maneuvers and wind is not considered in the calculated value of 27.6 min, as well as the efficiency of the battery. Anyhow, since the performance of the coaxial propulsion is an assumption, experimental tests should be performed before settling on a system. Especially since correct sizing of the fuel cell system is very important because of the loss in efficiency an under-dimensioned system would result. This is because of the voltage efficiency (see section 3.1). Additionally, a fuel cell system is quite expensive, so you don't want to get the sizing wrong.

5.6 PRELIMINARY FUEL CELL SIZING

Now that the total power requirement is known, a preliminary fuel cell sizing can be done. The operating voltage of the motors is 30.8 V. The motors can be run at both higher and lower voltages, but at higher voltages the efficiency [g/W] is reduced, and at lower voltages the thrust output is reduced, and the motor would need to run at a higher throttle to produce the same amount of thrust. Equation (3.14) gives the voltage of the fuel cell stack as the product of the cell voltage and the number of cells. The cell voltage is a function of current density, and as discussed in section 3.1, the higher operating cell voltage, the higher efficiency. As stated in ref. [27] an operating cell voltage of 0.8 V can be achieved for a fuel cell if correct design, materials, balance-of-plant components, and electronics are selected. Since the incentives to keep the balance of plant components as simple as possible to reduce weight, and simpler will possibly yield a loss in system efficiency, the operating cell voltage is taken to be 0.75 V. This gives required number of cells of:

$$\frac{30.8V}{0.75V} = 42 \text{ cells}$$

With the power requirement of 2000 W at normal operating conditions and fuel cell stack voltage V_{st} of:

$$V_{st} = 0.75V \cdot 42 = 31.5V$$

the current is calculated by equation (3.8) to be 63 A. The current density at operating cell voltage of 0.75 V can be taken to be approximately 0.5 A/cm² based on the typical i-V curve shown in Figure 5-12. From equation (3.15) the cell active area can now be calculated to 126 cm². A summary of the calculated values is given in Table 5-8. Design of an entire fuel cell system would require extensive research and is beyond the scope of this thesis. The next step is therefore to select a COTS fuel cell system which satisfy the constraints.

Table 5-8: Preliminary fuel cell sizing.

Rated power [W]	2000
Operating voltage [V]	30.8
Rated current[A]	63
Number of cells	42
Cell active area [cm²]	126

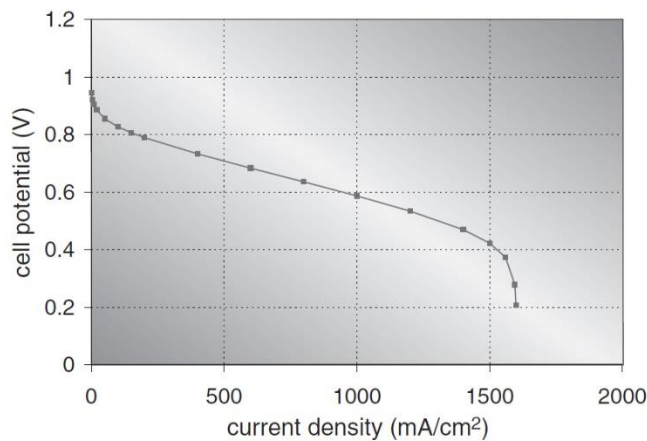


Figure 5-12: Typical i-V curve for a PEMFC [18].

5.7 SELECTION OF COTS FUEL CELL SYSTEM

There is a range of commercial fuel cell systems available suited for UAV applications, but until recently, most of the systems was mainly suited for fixed-wing configurations, which is much less power demanding than VTOL configurations. A list of fuel cell system for UAVs can be found in ref.[30], where most of the fuel cells are in the range from 100-1000 W. Anyhow, in this case the power demand is about 2000 W, and the amount of available systems are scarce. Still, there are some and those are listed in Table 5-9. We see that the system with the lowest weight, and highest specific power is the Aerostak 2000. This system weighs 650 g less than the second lightest system, namely Protium 2000. Additionally, the Aerostak 2000 has the least fuel consumption of those two. The other metrics are quite comparable between the systems, but the H1-fuel cell is the only system with operating ambient temperature below zero. This could certainly be an important factor when operating in the north. Anyhow, the fuel cell system of choice is the Aerostak 2000 because of the weight savings.

Table 5-9: Fuel cell systems in the 2000 W range

	Available		Concepts	
	Spectronik	MMC	HES	Intelligent Energy
Vendor				
Model	Protium 2000	H1-fuel cell	Aerostak 2000	N/A
Rated power [W]	2000	1800	2000	2000
Voltage output [V]	30-40	33.3-60	30-60	-
Rated current [A]	67	-	50	-
Weight [g]	3650	5200	3000	4200
Specific power [W/kg]	548	346	667	476***
Dimension [mm]	345x190x130	278x218x129	270x200x120	-
Fuel	Hydrogen gas	Hydrogen gas	Hydrogen gas	Hydrogen gas
Fuel consumption [L/min]	30	-	22.2	-
Delivery pressure, bar	0.4-0.7	0.5-0.7	0.5-0.7	-
Operating ambient temperature [°C]	0 to 45	-10 to 40	0 to 35	-
Price (\$)	33500	41000*	36000**	-

*includes 9L hydrogen tank

**Includes development fee

***Includes 6L hydrogen tank

5.8 AEROSTAK 2000 DETAILS

Horizon energy systems (HES), the manufacturer of Aerostak 2000, reports that the system is air-cooled and that the BOP components are included in the weight of 3 kg. The rated current is 50 A and the maximum power is 2500 W. Furthermore, the voltage efficiency is 57-60 % based on the HHV of hydrogen combustion. HES also claim a system efficiency of 50-54 % without stating whether it is based on LHV or HHV. Sometimes the LHV efficiency is used because it gives a higher efficiency number than the HHV efficiency, even though it is misleading. For a PEMFC the most correct is to use the HHV because the product of reaction is liquid water. Equation (3.6) can be used to check if the efficiency is based on LHV or HHV. Remember that the thermodynamic efficiency is 83 % based on HHV. If the fuel utilization efficiency is assumed to be 1, the system efficiency with a voltage efficiency of 57 % would be:

$$\varepsilon_{system} = 0.83 \cdot 0.57 \cdot 1 = 47 \%$$

or similarly with voltage efficiency of 60 %, the system efficiency would be 50 %. A system efficiency of 47-50 % is certainly lower than the reported efficiency of 50-54 %, even though the fuel utilization efficiency was set to 1 in the calculations of those values. This means that the reported system efficiency must be based on LHV.

Since we know the system efficiency and the voltage efficiency, the fuel utilization efficiency can be calculated. But first the thermodynamic efficiency based on LHV is found from equation (3.4):

$$\varepsilon_{thermo} = \frac{\Delta g_{LHV}}{\Delta h_{LHV}} = \frac{-228.5 \text{ kJ/mol}}{-241.8 \text{ kJ/mol}} = 0.945$$

The values for Δg_{LHV} and Δh_{LHV} is found in Appendix D. The average operating voltage E_{ave} can be calculated according to equation (3.7), where the reversible voltage is 1.23 V based on HHV:

$$\varepsilon_{voltage,HHV} = \frac{E_{ave}}{E_{0,HHV}} = \frac{E_{ave}}{1.23 \text{ V}} = 57 \text{ to } 60 \%$$

This results in an average operating voltage E_{ave} of 0.70 to 0.74 V per cell, which is very good because the system is extremely lightweight which require that the BOP components are kept simple. The reversible voltage based on LHV can be found from equation (3.5):

$$E_{0,LHV} = \frac{-\Delta g}{nF} = - \frac{-\left(-228.5 \frac{\text{kJ}}{\text{mol}}\right)}{\left(2 \text{ mol } e^{-} \text{ per mol reactant}\right) \left(96485 \frac{\text{C}}{\text{mol}}\right)} = 1.184 \text{ V}$$

The fuel utilization efficiency can now be calculated according to equation (3.6):

$$\varepsilon_{system} = 0.945 \cdot \frac{0.7 \text{ V}}{1.184} \cdot \varepsilon_{fuel} = 50 \%$$

This yields a fuel utilization efficiency ε_{fuel} of 90 %. Using the upper bounds for system efficiency of 54 % and average operating voltage of 0.74, the fuel utilization efficiency is 91 %. The real fuel utilization efficiency will be somewhat higher than these values because some of the energy is used to power the BOP components.

5.9 POWER CONTROL

As described in section 3.10 there are need for a power control system which ensures that the fuel cell is held at constant power delivery and that the battery takes the additional power requirements in relation to the climb phase, maneuvering, and wind gusts. This is because the fuel cell has relatively poor dynamic response, and because the life-time of the fuel cell is reduced when operating with dynamic loads.

The Aerostak 2000 comes with an integrated hybrid card. This passive system works on the principle of voltage matching; the output voltage of the fuel cell is measured, and the battery is connected when the voltage drops below a certain value.

5.10 SELECTION OF BATTERY

The battery should take the additional power demand in the climb phase. Based on the calculations in section 5.5.2, the peak power is 3172 W if the climb rate does not exceed 4 m/s. The battery then needs to take care of 1172 W.

Regarding capacity, the battery needs to provide approximately 5 Wh for the climb phase at climb rate of 4 m/s to an altitude of 60 m:

$$1172 \text{ W} \cdot \frac{60 \text{ m}}{4 \frac{\text{m}}{\text{s}}} \cdot \frac{1 \text{ h}}{3600 \text{ s}} = 4.88 \text{ Wh}$$

5 Wh seems very low, but the reason is that the duration of the climb phase is short (15 seconds). For an altitude of 120 m at a climb speed of 4 m/s, the needed battery capacity would be 10 Wh.

Anyhow, the battery should have larger capacity to provide energy to handle wind, maneuvers, hover and so on. Without knowing the power profile with its transient behavior during a normal mission, it is difficult to size the battery correctly. One can set a criterion such that the battery should be large enough to provide energy for 15 min in hover. The calculated power demand in hover is 2175 W,

which leaves 175 W to the battery. Accounting for the state of discharge of 70 %, the battery needs to have capacity of 62.5 Wh:

$$\frac{175W \cdot \frac{15 \text{ min}}{60 \text{ min/h}}}{0.70} = 62.5 \text{ Wh}$$

With a voltage of 29.6 (8S), the capacity of 62.5 Wh is converted to 2111.5 mAh. This should be ok since sizing the battery pack wrong is not critical; batteries are relatively cheap and can easily be replaced. Note that these calculations are based on that the fuel cell is not exceeding 2000 W in power output. The maximum power of the Aeropak 2000 is 2500 W, and it is not known at which voltage the hybrid card connects the battery, but the system is most efficient when the power output of the fuel cell is held at the rated power of 2000 W.

The battery should also have a high discharge rate (C-rate) to handle a range of power demands, and a high charge rate to recharge quickly. Another advantage with a high C-rate is that the IR-losses are less than for a battery with low C-rating, but a high C-rating also results in higher weight of the battery. There are a range of LiPo batteries available on the market. In this case a 3250 mAh 29.6 V battery from Maxamps is selected. Maxamps is a leading supplier of high quality LiPo batteries for the UAV market. This battery provides a high discharge rate (150 C) and high charge rate (5C). Detailed specifications are given in Table 5-10.

Table 5-10: Specifications of Maxamps LiPo battery.

Capacity	3250 mAh
Voltage (8S)	29.6 V
Discharge rate	150 C
Charge rate	5 C
Dimensions	(138x45x48) mm
Weight	639 g

The 150 C rate means that the battery theoretically can provide an ampere burst of $150 \cdot 3.25 \text{ A} = 585 \text{ A}$. With state of discharge of 70 %, the available capacity is 2275 mAh. Without considering IR losses, the maximum continuous current (180 s) the battery can provide is:

$$\frac{2276 \text{ mAh}}{180 \text{ s}} \cdot 3600 \frac{\text{s}}{\text{h}} = 45.5 \text{ A}$$

With an operating voltage of 29.6 V, the maximum continuous power of the battery is $29.6\text{V} \cdot 45.5 = 1347 \text{ W}$. The fuel cell – battery hybrid system thus has a maximum continuous power of $2500 \text{ W} + 1347 \text{ W} = 3847 \text{ W}$. This is considerably lower than the maximum continuous power for the KDE 7215 motor of 4405 W per motor. The relatively low maximum continuous power puts restrictions to the flight speeds. Anyhow, this is probably not an issue since the type of missions the Camflight is intended for does not involve high speeds and quick maneuvers. If the UAV is carrying another, lighter payload, the battery could be replaced by a larger battery which can support higher power.

For estimating the charge time, it is assumed that the fuel cell can provide about 200 W to the battery in forward flight, based on the power consumption in forward flight calculated from momentum theory. With 200 W the battery would go from fully discharged to fully charged in approximately 30 min (2 C rate). The high charge rate of 5 C cannot be utilized when the excess power available from the fuel cell is that low. Greater attention should be given to optimize the size of the fuel cell and the size of the battery such that both systems can perform their best.

6 HYDROGEN STORAGE ANALYSIS: COMPOSITE PRESSURE VESSELS

This chapter provides the sizing of the hydrogen storage, a comparison of the performance of spherical and cylindrical pressure vessels based on CLT, and the preliminary design of a spherical pressure vessel.

6.1 SIZING OF HYDROGEN STORAGE

The target flight time is 3 hours. The assumption of an average power consumption of 2000 W gives an energy requirement of 6000 Wh. With an efficiency of the fuel cell system of 50 % based on LHV (see section 5.8), the required energy is 12000 Wh. The next step is to find how many moles of hydrogen needed to provide that amount energy. Because the efficiency is based on LHV, this value also needs to be used when calculating the required number of moles of hydrogen. The enthalpy of reaction of hydrogen based on LHV is $\Delta h_{LHV} = 241 \text{ kJ/mol}$. As described in section 3.9, there is a loss of energy in the compression process. From Figure 3-7 we see that the energy loss for multistage compression of hydrogen from 0 to 300 bar is approximately 12 % of LHV. Now the required amount of hydrogen needed for 3 hours flight time can be calculated:

$$n \cdot (\Delta h_{LHV} - 0.12\Delta h_{LHV}) = 12000Wh = 43200 \text{ kJ} \quad (6.1)$$

Solving for n gives 204 moles of H₂. The real gas law in equation (3.18) can be used to calculate the required volume to store the hydrogen. The compressibility factor Z of hydrogen gas at 300 bar STP is approximately 1.2, as seen from Figure 3-7. The required volume of the pressure vessel is then:

$$V = \frac{1.2 \cdot 208 \text{ mol} \cdot 8.314 \frac{\text{m}^3 \text{Pa}}{\text{molK}} \cdot 293.15 \text{K}}{30 \text{MPa}} = 0.0203 \text{m}^3 = 20.3 \text{l}$$

6.2 COPV PRESSURE VESSEL DESIGN CONSIDERATIONS

The pressure vessel should be 20.3 l to provide a flight time of 3 h. The available weight for the pressure vessel is 6.36 kg:

Total weight	25 kg
-Frame (includes motors, ESCs and propellers)	10 kg
-Lidar	5 kg
-Fuel cell	3 kg
-Battery	0.64 kg
=Pressure vessel	6.36 kg

The pressure vessel is to be made of a lightweight composite material, and classical lamination theory is used to calculate the required dimensions of the pressure vessel. Common composite materials are carbon, Kevlar and glass fibers. Carbon and Kevlar fibers have higher specific strength than glass fibers and are therefore most suited for this application where weight are crucial. Carbon fiber are the most widely used for advanced composites and comes in a range of stiffnesses and strengths depending on the manufacturing process. Kevlar has very high strength and lower density than carbon

fiber but are susceptible to moisture absorption[54]. Since the pressure vessel is potentially going to be used in moist weather, carbon fiber is chosen as material for this pressure vessel. The carbon/epoxy composite material used in the further calculations have engineering constants and strength as shown in Table 6-1 and

Table 6-2, respectively.

Table 6-1: Elastic properties of carbon/epoxy composite material [55]

Specific mass	1.53 g/cm ³
Volume fraction fibers V_f	0.6
Longitudinal elastic modulus E₁	134 GPa
Transverse elastic modulus E₂	7 GPa
Shear modulus G₁₂	4.2 GPa
Poisson ratio ν₁₂	0.25

Table 6-2: Strength of carbon/epoxy composite material [55]

Longitudinal tensile fracture strength	1270 MPa
Longitudinal compressive fracture strength	1130 MPa
Transverse tensile fracture strength	42 MPa
Transverse compressive fracture strength	141 MPa
In plane shear strength	63 MPa

There are almost infinite solutions in design of a composite structure in regard to ply orientation and lay-up, ply thickness, and the number of plies. The abd-stiffness matrix of the laminate (equation (4.43)) is depended upon all these parameters. One cannot solve for all these unknowns using a single force-strain equation, and hence the optimization of a composite structure is a difficult task. To make it easier, the laminate can be characterized as symmetric, antisymmetric, balanced, angle-ply, cross-ply and combinations of these. As a general rule of thumb, it is recommended to use a balanced and symmetrical layup whenever it is possible. With this layup the bending/coupling stiffness is eliminated, and therefore warpage and unexpected distortions are avoided. The analysis then becomes considerably simpler. In addition, the thickness of the plies should be small to reduce interlaminar stresses [54].

Based on the above discussion, the pressure vessel is decided to be made of a balanced angle-ply laminate. An angle-ply laminate consists of layers oriented in $-\theta$ and $+\theta$ where $0^\circ < \theta < 90^\circ$ with respect to the global coordinate axes. A balanced laminate has the same amount of $-\theta$ and $+\theta$ plies with identical thickness on both sides of the mid-plane. With this layup the only unknowns are the winding angle θ and the number of layers. The thickness of each layer is set to a typical minimum thickness of a carbon/epoxy lamina which is 0.13 mm [43].

The goal is to design a spherical pressure vessel because this is the optimal shape with the least surface area per volume. The spherical pressure vessel is more difficult to manufacture than a typical cylindrical pressure vessel so a comparison between the two is carried out in the next section to find the relative performance.

It is decided to make a type IV pressure vessel, because this type has normally a lower weight per liter storage than a type III pressure vessel (see Table 4-1 for indicative weight). A polymer liner would also be easier to manufacture than an aluminum liner of spherical shape. The liner is made of HDPE material, with properties shown in Table 6-3.

Table 6-3: Properties of HDPE liner [56]

Tensile modulus	650 Mpa
Yield stress	19 Mpa
Yield strain	11 %
Density	0.94 g/cm ³

6.3 COMPARISON OF SPHERICAL AND CYLINDRICAL PRESSURE VESSEL

Classical lamination theory together with the Tsai-Wu failure criterion described in section 4.3 and 4.4 respectively, equations (4.15) through (4.50), are modelled in MATLAB, with the program given in Appendix A.6. The safety factor of the pressure vessels is set to 2.35 based on the discussion in section 4.5. Before the comparison is made, the optimum winding angle for spherical and cylindrical pressure vessels is calculated in the next two sections.

6.3.1 Spherical

An illustration of the spherical pressure vessel is shown in Figure 6-1. The internal volume of a spherical pressure vessel is given by:

$$V = \frac{4}{3}\pi r^3 \quad (6.2)$$

where r is the internal radius. The forces per unit length is calculated according to equation (4.2):

$$N_x = \frac{pr}{2} = \frac{30MPa \cdot r}{2} = 15rMPa$$

$$N_y = \frac{pr}{2} = \frac{30MPa \cdot r}{2} = 15rMPa$$

$$N_{xy} = N_{yx} = 0$$

There are no applied moments to the pressure vessel ($M_x = M_y = M_{xy} = 0$).

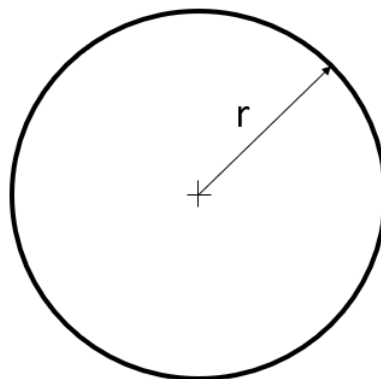


Figure 6-1: Geometry of spherical pressure vessel

The optimum winding angle θ to minimize the laminate thickness is calculated with the MATLAB code given in Appendix A.6. The result is seen in Figure 6-2. The angle which gives the lowest Tsai-Wu failure criterion value, and thus the minimum thickness for the pressure vessel, is 45° . This seems reasonable because the loading is symmetric.

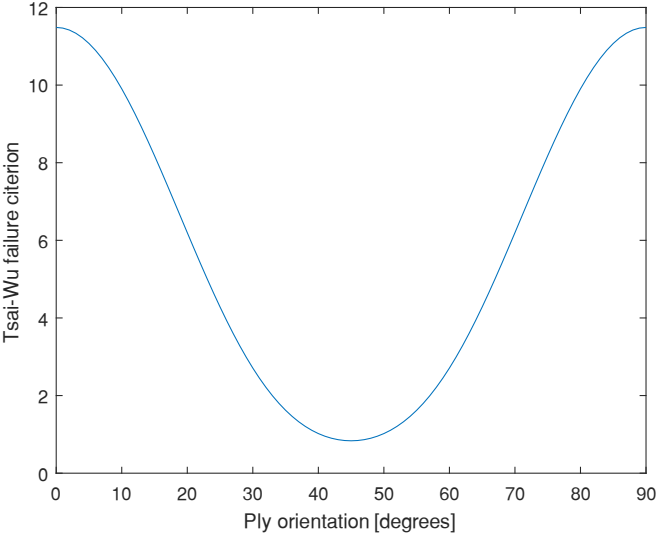


Figure 6-2: Shows the Tsai-Wu failure criterion value for different ply orientations for spherical pressure vessel, and hence the optimum winding angle.

Since the optimum winding angle is $\pm 45^\circ$, the lamina is characterized as a cross-ply lamina, i.e. it consists of layers oriented 90° relative to each other. The $\pm 45^\circ$ layer orientation is equivalent to orientation an of 0 and 90 degrees because the reference axis of the laminate can be rotated by 45° . The cross-ply lamina configuration is also known as a balanced orthotropic lamina. Because of symmetry, the elastic properties are equal in the principle directions 1 and 2 ($E_1 = E_2, S_{11} = S_{22}$). Two layers of unidirectional lamina are replaced by one balanced orthotropic layer (see Figure 6-3) in the modelling. Then the transformed reduced stiffnesses for the cross-ply layer is calculated from [57]:

$$\bar{Q}_{ij}^{\pm 45} = \frac{1}{2}(\bar{Q}_{ij}^{+45} + \bar{Q}_{ij}^{-45}) \tag{6.3}$$

where \bar{Q}_{ij}^{+45} and \bar{Q}_{ij}^{-45} is the transformed reduced stiffnesses for the $+45^\circ$ and -45° layers, respectively.

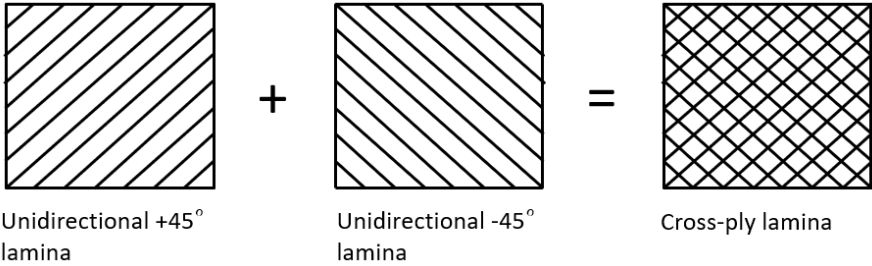


Figure 6-3: Two unidirectional layers with 90 degrees relative rotation make up a cross-ply layer.

Now that the two layers are replaced by one, the strength in the principal directions changes from the values given in Table 6-2. The strengths for a layer consisting of 50 % $+45^\circ$ degrees layers and 50 % -45° degrees layers are found in the figures in Appendix B and are summarized in Table 6-4.

Table 6-4: Strength of a cross-ply lamina with fiber volume fraction V_f of 0.6, in the global coordinate system.

Tensile fracture strength in x-direction	425 MPa
Compressive fracture strength in x-direction	595 MPa
Tensile fracture strength in y-direction	425 MPa
Compressive fracture strength in y-direction	595 MPa
In plane shear strength	63 MPa

6.3.2 Cylindrical

The cylindrical pressure vessel considered, with $L/D=3$, is shown on Figure 6-4. The internal volume of the pressure vessel is given by:

$$V = \frac{4}{3}\pi r^3 + \pi r^2(L - 2r) = \frac{16}{3}\pi r^3 \quad (6.4)$$

The forces per unit length in a cylindrical pressure vessel is calculated with aid of equation (4.8) and (4.10):

$$N_x = \frac{pr}{2} = \frac{30MPa \cdot r}{2} = 15rMPa$$

$$N_y = pr = 30rMPa$$

$$N_{xy} = N_{yx} = 0$$

The MATLAB code in Appendix A.6 is used to calculate the optimal winding angle, and the result is shown in Figure 6-5. We see that the angle which gives the lowest failure criterion value, and hence the minimum required thickness, is 50° . The cylindrical pressure vessel will have a balanced layup consisting of $+50^\circ$ and -50° oriented layers. This configuration is known as an angle-ply laminate. The laminate is modelled as a composition of unidirectional laminas with different transformed reduced stiffness matrices for the $+50$ layers and -50 layers.

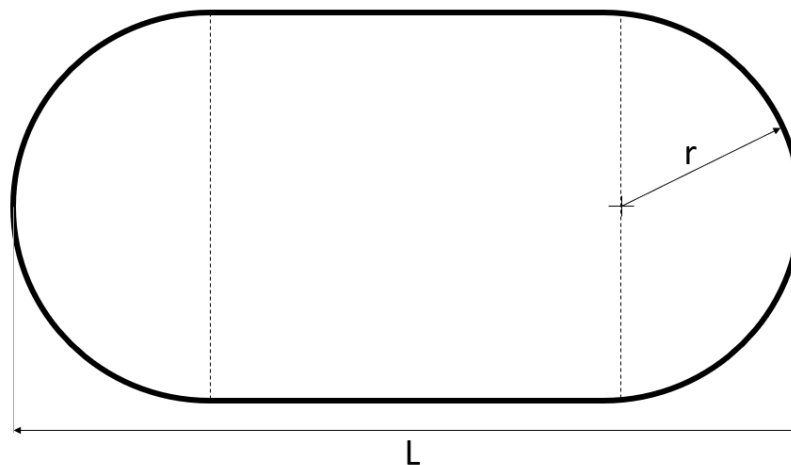


Figure 6-4: Geometry of cylindrical pressure vessel.

In an illustration of the design process of a cylindrical pressure vessel in ref. [58], different balanced symmetric layups were compared, showing that the angle-ply layup was the optimum layup.

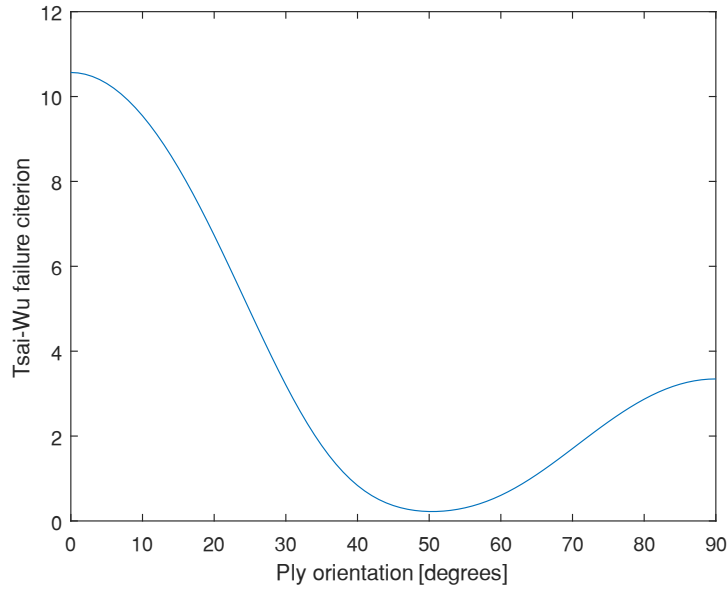


Figure 6-5: Shows the Tsai-Wu failure criterion value for different ply orientations for a cylindrical pressure vessel, and hence the optimum winding angle.

6.3.3 Performance of spherical vs. cylindrical pressure vessel

Now that the optimum winding angle is known, the next step is to find how many layers is needed to satisfy the failure criterion for both the spherical and cylindrical pressure vessel. The Tsai-Wu failure criterion should be satisfied for each layer. Since both pressure vessels consists of symmetric laminates, the coupling stiffness matrix B is zero in both cases, and thus the stresses do not depend on the distance z . For the spherical pressure vessel all the layers are identical, and thus the Tsai-Wu failure criterion is the same for all layers. For the cylindrical pressure vessel, the Tsai-Wu failure criteria value is the same for the +50 and -50 degrees layers because of symmetry. This results in that all the plies will fail simultaneously, for both the spherical and cylindrical pressure vessels.

To get a good comparison of the cylindrical and spherical pressure vessels, the number of required layers is calculated for internal volumes from 5 to 25 liters with a step of 1 liter. The MATLAB program is given in Appendix A.7. When the required number of layers are known, the volume of the resulting composite shell can be calculated with the aid of equation (6.2) and (6.4) for the spherical and cylindrical shell, respectively. The total weight (composite overwrap plus liner) of the pressure vessels is calculated from:

$$M_{total} = M_{composite} + M_{liner} = \rho_{carbon/epoxy}V_{composite} + \rho_{HDPE}V_{liner} \quad (6.5)$$

The total weight of the spherical and cylindrical pressure vessels with internal volume of 5 to 25 liters are shown in Figure 6-6. Note that the weight of other BOP components and the extra carbon/epoxy material needed to deal with stress concentrations around the outlet hole is not included in the total weight. The weight of these components is assumed to be small, and thus have small impact on the results. Figure 6-6 clearly shows that the cylindrical pressure vessel is heavier than the spherical pressure vessel. It also shows that the data points deviate slightly from the trendline for both cases. This is because the Tsai-Wu failure value varies slightly between 0.94 to 0.99, and thus the actual safety factor varies between 2.5 and 2.37. The reason is that the layers have fixed thickness. Also notice the step-wise increase of the data points in Figure 6-6. The steps are caused by that the same number of layers is used for several volumes.

The ratio R between the weight of the cylindrical and the spherical pressure vessels is given by:

$$R = \frac{M_{cylindrical}}{M_{spherical}}$$

Where $M_{cylindrical}$ and $M_{spherical}$ is the total weight of the cylindrical and spherical pressure vessel, respectively. In Figure 6-7, R is plotted against the internal volume. It is seen that the mean ratio is approximately 1.18, which implies that the cylindrical pressure vessel is 18 % heavier than the spherical pressure vessel, or reversely, the spherical pressure vessel weighs 15 % less than the cylindrical counterpart. Notice that the trend shows that the ratio is reduced as the pressure vessels gets larger. This is probably since the liner thickness is the same for all the sizes. For the larger pressure vessels, the volume of the liner is a minor portion of the total volume than for the smaller pressure vessels, and the cylindrical pressure vessels are more affected by the thickness of the liner because they have a larger surface area compared to volume. See Appendix C for detailed results for both the spherical and cylindrical pressure vessels.

The weight savings of approximately 15 % by using a spherical pressure vessel make up for the more difficult manufacturing of a spherical pressure vessel compared to a cylindrical pressure vessel. Especially since it is to be used in a UAV application, where weight is the most severe constraint. It is therefore decided to go forth with the preliminary design of a spherical pressure vessel.

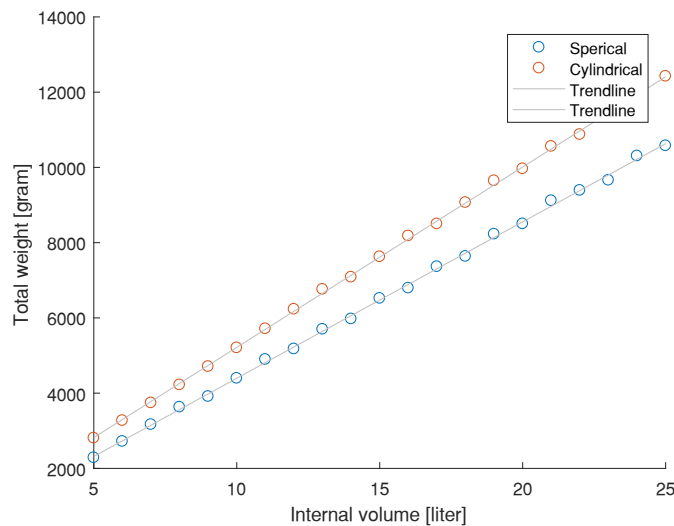


Figure 6-6: Total weight of spherical and cylindrical pressure vessels of different internal volumes

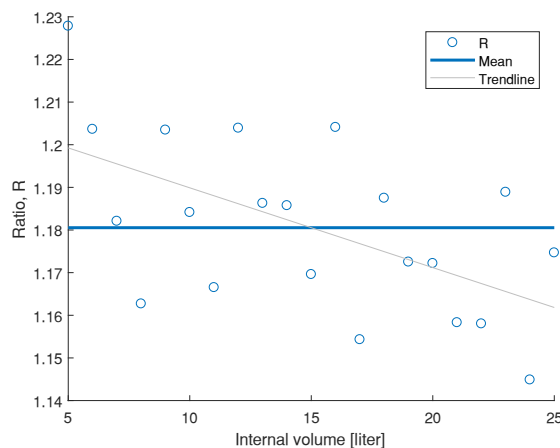


Figure 6-7: Ratio R between the weight of cylindrical and spherical pressure vessels for different internal volumes

6.4 COMPARISON TO COTS PRESSURE VESSELS

To validate the above results, the pressure vessels are compared to COTS lightweight pressure vessels usable in UAV applications. Currently there are no COTS lightweight spherical pressure vessels. This is probably because the use of fuel cells in VTOL UAV applications is quite new, and in fixed-wing UAVs it is more convenient to use a cylindrical tank, mainly because of the aerodynamics. There exist several COTS COPV cylindrical pressure vessels suited for UAV applications. Two 9-liter hydrogen tanks with $L/D \approx 3$ are shown in Table 6-5, together with the 9-liter cylindrical tank computed in the section above. The data is from the vendors' websites [32, 59]. The table shows that the calculated cylindrical pressure vessel weighs significantly more than the COTS pressure vessels from HES and MMC. The reason may be that the COTS pressure vessels are designed with a lower safety factor and/or that the carbon/epoxy material has higher strength than the material used in the calculations. Remember that the carbon/epoxy material properties are highly dependent on the manufacturing process. There is a reason to think that the material used in the calculations is not the strongest because the volume fraction of carbon fiber is only 0.6. Commonly the volume fraction of carbon fiber is between 0.6-0.85 for the filament winding manufacturing method. The strength of the composite material is approximately proportionate to the carbon fiber volume fraction[55]:

$$\sigma_{l,rupture} \approx \sigma_{f,rupture} V_f$$

Where $\sigma_{l,rupture}$ is the longitudinal strength of lamina, $\sigma_{f,rupture}$ is the strength of the carbon fiber, and V_f is the volume fraction of fibers.

The reason why this particular material was used is that there existed strength properties for both angle-ply and cross-ply laminas, which were needed to do the comparison between cylindrical and spherical pressure vessels.

Another thing worth mentioning is that the outer dimensions of the calculated cylinder and the pressure vessel from HES are almost exactly the same, where the one from HES is just a bit larger than the calculated pressure vessel. Yet, the pressure vessel from HES weighs almost 1 kg less, which indicates that the material used for the pressure vessel from HES has higher specific strength than the material used in the calculations.

Table 6-5: Properties of two 9 L COTS cylindrical pressure vessels together with a 9 L calculated cylindrical pressure vessel.

Vendor	Type of pressure vessel	Internal volume [L]	Weight [kg]	Length [mm]	Diameter [mm]	Normalized Weight [kg/L]	Operating pressure [bar]
HES	Type III	9	3.8	543	182	0.42	Up to 300
MMC	N/A	9	3.1	520	167	0.34	Up to 350
Calculated cylindrical	Type IV	9	4.7	542	180.6	0.52	Up to 300

The weight of the calculated cylindrical pressure vessel of 0.52 kg/L is higher than for both the COTS pressure vessels, and also higher than the indicative weight for type IV pressure vessels of 0.3-0.4 kg/L (Table 4-1).

6.5 DESIGN OF SPHERICAL PRESSURE VESSEL

In the design of the spherical pressure vessel there is two contrary requirements; the pressure vessel should provide 3 hours flight time and weigh less than 6.36 kg. In this case the weight constraint trumps the desired flight time because of the need to stay within the maximum weight for a small UAV, and because the other components are dimensioned for a take-off weight of 25 kg. In addition to the HDPE liner and carbon fiber overwrap, the pressure vessel also needs other components such as:

- Aluminum boss
- Two-stage pressure regulator to reduce the internal pressure to the fuel cell working pressure
- Pressure relief device to vent if the tank is overheated
- Excess flow valve to prevent overfilling
- Pressure and temperature transducers to monitor pressure and temperature during refueling
- Solenoid valve to control hydrogen flow during operation
- Protective foam to protect from impact
- Other valves and safety devices

The design of the balance of plant components is beyond the scope of this thesis, but it is assumed that they constitute 25 % of the total weight. In a performance assessment of a 700 bar of a type IV hydrogen pressure vessel by Hua et al. [48] the BOP components constituted 13 % of the total weight, so an assumption of 25 % is conservative, but gives a relatively large design space in the further design process.

As mentioned, the available weight for the hydrogen tank is 6.36 kg. If the BOP components constitute 25 % (1.6 kg) of the total weight, it leaves 4.7 kg for the composite overwrap and the HDPE liner.

A challenge when designing a spherical pressure vessel with cross-ply laminate is that the available strength properties of such lamina is scarce. The results from the comparison between the designed cylindrical pressure vessel and the COTS pressure vessels indicates that the previous used carbon/epoxy material has relatively low strength. After extensive search, the biaxial strength of IM6/3501-6 carbon/epoxy cross-ply laminate was found in ref. [60]. IM6/3501-6 is commercial available from Hexcel, a world leader in advanced composite technology. IM6 is a high performance carbon fiber which offers high tensile strength, and is well suited for strength critical applications. The 3501-6 resin is a damage-resistant epoxy matrix well suited for general purpose structural applications. Table 6-6 shows the properties of IM6/3501-6 carbon/epoxy material. The biaxial strength in ref. [60] was experimentally determined by using cruciform specimens, which is a frequently used method to test the biaxial strength of composite materials. They managed to get a low COV which is a challenge in such experiments. The results from the experiments with equal loading in x- and y-direction is shown in Table 6-7. The strength in x- and y-direction should theoretically be identical. In the calculation of the spherical pressure vessel, lower bounds for the strengths of 600 MPa in tensile and 530 MPa in compression in both x- and y direction are therefor used. The shear strength of the material is not known, but is taken to be 40 MPa as for the previous used material. This should be ok since, as we will see later, there are no shear stress in the principle directions, and the term incorporating the shear strength in the Tsai-Wu failure criterion will disappear.

Table 6-6: Properties of IM6/3501-6 carbon/epoxy lamina with carbon fiber volume fraction V_f of 63.5 % [61].

Longitudinal modulus E_1	157 MPa
Transverse modulus E_2	9 MPa
Shear modulus G_{12}	5.7 MPa
Poisson's ratio ν_{12}	0.3
Density	1552 kg/m ³
Ply thickness	0.1335 mm

Table 6-7: Biaxial strength of IM6/3501-6 cross-ply laminate [60].

	Average x-direction		Average y-direction	
	Ultimate Strength	COV	Ultimate Strength	COV
Tensile	607 MPa	2.9	601 MPa	2.8
Compression	531 MPa	4.2	534 MPa	5.2

The resulting weight for the carbon overwrap and the HDPE liner for the spherical tank is shown in Figure 6-8. The figure shows that a 22 l spherical tank stays within the maximum weight of 4.8 kg for the composite overwrap and HDPE liner. Anyhow, it is decided to go forth with internal volume of 21 liter because the weight jump from 21 liter to 22 liter is quite high, which arise from the discrete thickness of the layers. The next subsection will provide detailed calculations of a 21 l spherical pressure vessel according to CLT.

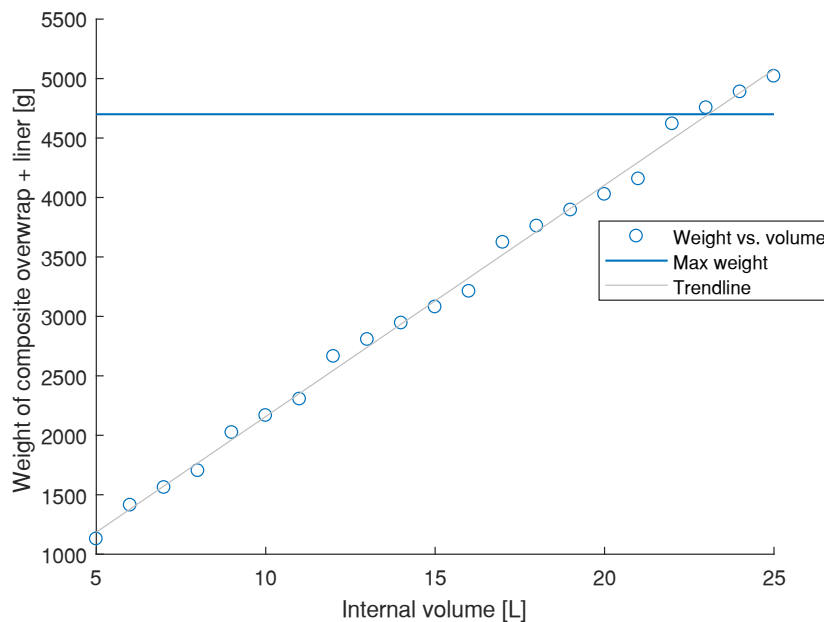


Figure 6-8: Weight of spherical pressure vessel for different volumes.

6.5.1 Calculations of a 21 liter spherical pressure vessel

The radius of the tank is calculated according to equation (6.2), which gives an inner radius r_1 of 171.1 mm. The inner radius of the composite layer is thus 173.1 mm with HDPE liner of 2 mm. The forces per unit meter can now be calculated:

$$N_x = \frac{pr}{2} = \frac{30MPa \cdot 0.1731m}{2} = 2.6 MPam$$

$$N_y = \frac{pr}{2} = \frac{30MPa \cdot 0.1731m}{2} = 2.6 MPam$$

$$N_{xy} = N_{yx} = 0$$

The forces per unit meter on an element is shown in Figure 6-9. The parameters used in the calculations are summarized in Table 6-8. Notice that the layer thickness is 2 times 0.13mm. The reason is that one layer is composed by 2 unidirectional layers with 90° relative rotation (see section 6.3.1, Figure 6-3). The MATLAB program is given in Appendix A.8.

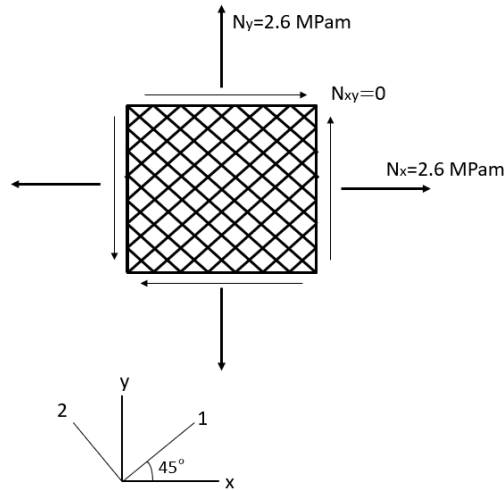


Figure 6-9: Force per unit meter acting on an element.

Table 6-8: 21 l spherical pressure vessel parameters.

Winding angle	45 degrees
Safety factor	2.35
Layer thickness	2*0.1335 mm
HDPE liner thickness	2 mm
Tensile strength in x- and y direction	600 MPa
Compressive strength in x- and y direction	530 MPa
Shear strength	40 MPa

The reduced stiffnesses are calculated according to equations (4.15) and (4.16) which gives:

$$Q_{ij} = \begin{bmatrix} 157.8 & 2.71 & 0 \\ 2.72 & 9.05 & 0 \\ 0 & 0 & 11.4 \end{bmatrix} GPa$$

The transformed reduced stiffnesses are calculated according to equations (2.21), (2.22) and (6.3):

$$\bar{Q}_{ij}^{\pm 45} = \frac{1}{2} \left(\begin{bmatrix} 48.7 & 37.4 & 37.2 \\ 37.4 & 48.7 & 37.2 \\ 37.2 & 37.2 & 40.4 \end{bmatrix}^{+45} + \begin{bmatrix} 48.7 & 37.4 & -37.2 \\ 37.4 & 48.7 & -37.2 \\ -37.2 & -37.2 & 40.4 \end{bmatrix}^{-45} \right) = \begin{bmatrix} 48.7 & 37.4 & 0 \\ 37.4 & 48.7 & 0 \\ 0 & 0 & 40.4 \end{bmatrix} GPa$$

The required number of layers needed to satisfy the Tsai-Wu failure criterion with safety factor of 2.35, is 22.

The laminate extensional stiffnesses are calculated with equation (4.40), which gives:

$$[A] = \begin{bmatrix} 286.5 & 219.5 & 0 \\ 219.5 & 286.5 & 0 \\ 0 & 0 & 237.1 \end{bmatrix} MPa$$

The laminate coupling stiffnesses are calculated with equation (4.41), which gives:

$$[B] = \begin{bmatrix} 0 & 0 & 0 \\ 0 & 0 & 0 \\ 0 & 0 & 0 \end{bmatrix} Pam^2$$

And similarly, the laminate bending stiffnesses are calculated with equation (4.42):

$$[D] = \begin{bmatrix} 823.7 & 631.2 & 0 \\ 631.2 & 823.7 & 0 \\ 0 & 0 & 681.6 \end{bmatrix} Pam^3$$

Since the coupling stiffnesses are zero and there are no applied moments, the midplane strains can be found from the inverse of the laminate extensional stiffness [A], according to equation (4.43):

$$\begin{Bmatrix} \varepsilon_x^0 \\ \varepsilon_y^0 \\ \varepsilon_{xy}^0 \end{Bmatrix} = [A]^{-1} \begin{Bmatrix} N_x \\ N_y \\ N_{xy} \end{Bmatrix} = \begin{bmatrix} 0.8455 & -0.6479 & 0 \\ -0.6479 & 0.8455 & 0 \\ 0 & 0 & 0.4218 \end{bmatrix} \cdot 10^{-8} (Pam)^{-1} \begin{Bmatrix} 2.6 \\ 2.6 \\ 0 \end{Bmatrix} MPam = \begin{Bmatrix} 0.0051 \\ 0.0051 \\ 0 \end{Bmatrix}$$

The midplane curvatures are zero, $\kappa_x = \kappa_y = \kappa_{xy} = 0$, and so the stresses do not vary with the distance z from the midplane. The stresses in each layer are calculated according to equation (4.30):

$$\begin{Bmatrix} \sigma_x \\ \sigma_y \\ \tau_{xy} \end{Bmatrix} = \begin{bmatrix} 48.7 & 37.4 & 0 \\ 37.4 & 48.7 & 0 \\ 0 & 0 & 40.4 \end{bmatrix} \begin{Bmatrix} 0.0051 \\ 0.0051 \\ 0 \end{Bmatrix} GPa = \begin{Bmatrix} 442 \\ 442 \\ 0 \end{Bmatrix} MPa$$

The stresses in the principal directions are equal to the stresses in x- and y-directions because of the symmetry that arise from modelling two unidirectional layers with 90° relative rotation as one balanced orthotropic layer, and because of the symmetric loading. In fact, the stresses are the same in all directions.

The last thing to do is to verify that the Tsai-Wu failure criteria is satisfied. With safety factor of 2.35, equations (4.45) through (4.50) yields:

$$2.35((-2.2 \cdot 10^{-10} \cdot 442 \cdot 10^6) + (-2.2 \cdot 10^{-10} \cdot 442 \cdot 10^6) + 3.145 \cdot 10^{-18}(442 \cdot 10^6)^2 + 3.145 \cdot 10^{-18}(442 \cdot 10^6)^2 + 6.25 \cdot 10^{-16}(0)^2 - \sqrt{3.145 \cdot 10^{-18} \cdot 3.145 \cdot 10^{-18} \cdot 442 \cdot 10^6 \cdot 442 \cdot 10^6}) = 0.99$$

The Tsai-Wu failure criterion is satisfied. The outer radius of the pressure vessel consisting of 22 layers, where each layer has thickness $2 \cdot 0.013$ mm, are:

$$r_o = 171.1mm + 2mm + 22 \cdot (2 \cdot 0.1335mm) = 179 mm$$

Now the volume of composite shell and the HDPE liner can be found, and the total weight of those components is calculated according to equation (6.5):

$$M = \frac{1.552g}{cm^3} \cdot 2289cm^3 + \frac{0.94g}{cm^3} \cdot 744.8cm^3 = 4253 g$$

With the additional weight of BOP components of 25 %, the total empty weight of the 21 l spherical pressure vessel is 5316 g, or 0.25 kg/L. Compared to the weight of the cylindrical 9 liter pressure vessel from MMC (Table 6-5) of 0.34 kg/L, this is very good. The ratio R between those two is 1.36, which means that the spherical pressure vessel from MMC is 36 % heavier than the custom designed

spherical pressure vessel. This is even more than what was predicted in section 6.3.3. The reason is most likely that the material used in the calculations above has higher strength than the material of the MMC pressure vessel. Anyhow, the results are dependent upon designing BOP components with weight of less than 25 % of the pressure vessel weight. The further design process should focus on design of lightweight BOP components, and experimental testing of IM6/3501-6 carbon/epoxy material should be done to verify the strengths. Furthermore, the thickness of the HDPE liner needs to be experimentally tested to check if it satisfies the permeation rate. The thickness may even be reduced.

The amount of hydrogen that can be stored in the pressure vessel is calculated according to equation (3.18) which yields 215.4 moles, or converted to grams:

$$215.4 \text{ mol } H_2 \cdot 2.016 \frac{\text{g}}{\text{mol } H_2} = 434.2 \text{ g}$$

The gravimetric capacity is 8.1 wt%, which is very good compared to the metrics in Table 3-3, but considerable lower than the Ion tiger team achieved with their type IV pressure vessel with gravimetric capacity of 13 wt%. The energy capacity is calculated with equation (6.1) which takes into account the energy loss during the compression process. The resulting energy capacity is 45682 kJ or 12689 Wh, which gives energy density of 2386 Wh/kg. Compared to the metrics in Table 3-1, this is good. The preliminary design parameters and properties of the spherical pressure vessel are summarized in Table 6-9.

Table 6-9: Spherical pressure vessel parameters

Operating pressure	300 bar
Outer diameter	358mm
Water capacity	21 l
Hydrogen mass	434 g
Energy capacity	12689 Wh
Thickness	
Carbon/epoxy overwrap	5.9 mm
HDPE liner	2 mm
Weight	
Composite overwrap	3553 g
HDPE liner	700 g
BOP components (25 %)	1063 g
Total weight	5316 g
Normalized weight	0.25 kg/L
Metrics	
Gravimetric capacity	8.1 wt%
Volumetric capacity	20.7 g-H ₂ /L
Specific energy	2386 Wh/kg

7 RESULTS: SYSTEM PERFORMANCE AND ENDURANCE ESTIMATES

A summary of the different components composing the propulsion system is found in Table 7-1, and a block diagram of the system is shown in Figure 7-1.

Table 7-1: Propulsion system components, see the other tables for detailed information.

Components	Detailed information	
Fuel cell system	Aerostak 2000	Table 5-9
Battery	Maxamps 3250 mAh 8S	Table 5-10
Motors	KDE 7215XF KV135	Table 5-3
ESCs	KDEXF-UAS95HVC	Table 5-5
Propellers	KDE Dual 30.5"	
Spherical pressure vessel	Custom	Table 6-9

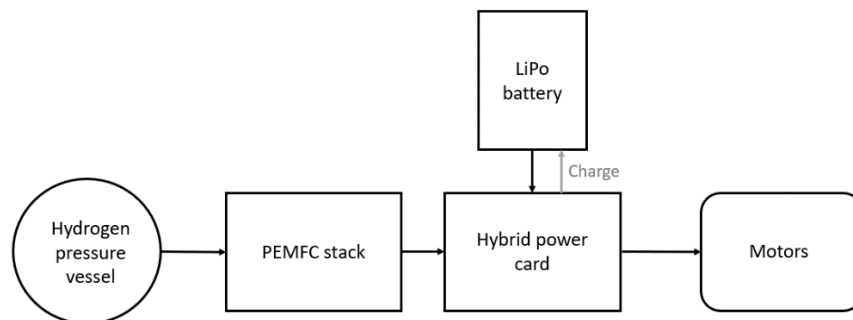


Figure 7-1: Block diagram of the propulsion system.

Remember that the preliminary goal was to design a propulsion system of maximum 10 kg that could provide 3 hours flight time. The weight of the fuel cell – battery hybrid system is:

Fuel cell	3000 g
+ Battery	639 kg
+Pressure vessel	5316 kg
=Propulsion system	8955 kg

The weight of the motors, propellers and ESCs are included in the original weight of the Camflight of 10 kg without payload and batteries. From the calculations above we see that the goal of 10 kg for the propulsion system is reached, and there are approximate 1 kg in excess for the mounting equipment. With an efficiency of the fuel cell system η_{FC} of 50 % (based on LHV) and an average power consumption of 2000 W, the flight time can be estimated as

$$Endurance = \eta_{FC} \frac{Capacity}{Average\ power\ consumption} = 50\% \cdot \frac{12689\ Wh}{2000\ W} = 3.17\ h$$

A flight time of 3.17 h (3 h and 10 min) is a 7-fold improvement of the original flight time of 25 min with 5 kg payload, which is impressive. This endurance is in ideal conditions, based on the mission profile in section 5.3, with no wind, acceleration or change in flight direction. The endurance in real conditions will be somewhat less. In a study by Donateo et al. [62] the fuel consumption was found to be about 5 % larger in a ‘rough’ mission, where the power curve had a lot of peaks. This value was

based on modelling of a fuel cell with PLA.N.E.S software, a simulation and optimization software for powertrains for aircrafts. This was for a fixed wing UAV, so further investigation must be done on how the fuel cell system works in real conditions for a VTOL UAV. But if the additional power in a rough mission is between 5 and 20 %, the resulting improvement of endurance would still be impressive.

The endurance is also estimated for different payloads. The average power consumption is estimated as the power needed in forward flight (see section 5.5.3) with adding 15 % of that power to make up for the climb phase, hovering etc. The efficiency of the motors and the fuel cell is taken to be the same as in previous calculations, even though the efficiency would be a bit higher for both the motors and the fuel cell at lower load. The estimated endurance for different payloads is represented in Figure 7-2. With 1.5 kg payload the flight time is estimated to 4.1 h, which is 5 times longer than the original flight time of 50 min. The flight time at lower loads will be a little higher because of the higher efficiency. Even though, it is unlikely that it will reach a 7-fold improvement, which shows that the largest improvement happens at the take-off weight the system is designed for.

Furthermore, the endurance is estimated for spherical pressure vessels of different sizes. The weight of the pressure vessels is taken to be 0.25 kg/L, which is the same as for the designed spherical pressure vessel. The average power consumption is estimated as the power needed for forward flight plus 15 % of that power to make up for the additional power needed in the climb phase. The result is represented in Figure 7-3. It is seen that the flight time is steadily increasing with tank size, which implies that the hydrogen storage should be as large as possible. Anyhow, the curve will reach a peak at one point because the efficiency of the system is decreasing with increasing power consumption resulting from the increased weight of the hydrogen tank. This is due to the shape of the i-V curve of the fuel cell (example of a i-V curve is found in Figure 3-3). If the i-V curve of Aerostak 2000, together with the cell-active area was known, the loss of efficiency could be modelled, and the peak could be found. The peak is certainly not reached in the interval from 5 to 21 liters because the power needed with a 21 liter tank is 2000 W, which is the rated power of Aerostak 2000.

The performance of the propulsion system is summarized in Table 7-2. The energy density of 1417 Wh/kg and the power density of 223 W/kg is based on the total weight of the fuel cell, the battery, and the hydrogen tank. Compared to the metrics of a LiPo battery (Table 2-1), the designed energy storage has considerably higher specific energy and lower specific power, as expected. As the size of the fuel storage increases, the specific power reduces and the specific energy increases. For a mission with LIDAR which does not require high speeds and quick maneuvers, the best solutions seems to be a system with high specific energy and low specific power. In other missions, the specific power may needs to be higher, and thus the specific energy will be less.

Table 7-2: Performance of the designed propulsion system

Rated power	2000 W
Maximum continuous power (180 s)	3840 W
Capacity	12689 Wh
Estimated endurance, 5 kg payload	3.17 h
Estimated endurance, 1,5 kg payload	4.1 h
Weight	8955 g
Specific power	223 W/kg
Specific energy	1417 Wh/kg
Ambient temperature	0 to 40°

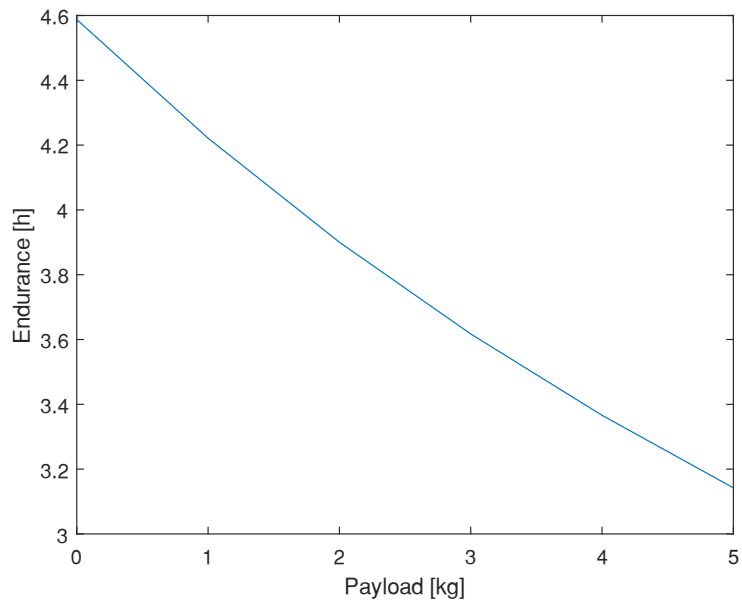


Figure 7-2: Estimated endurance for different payloads.

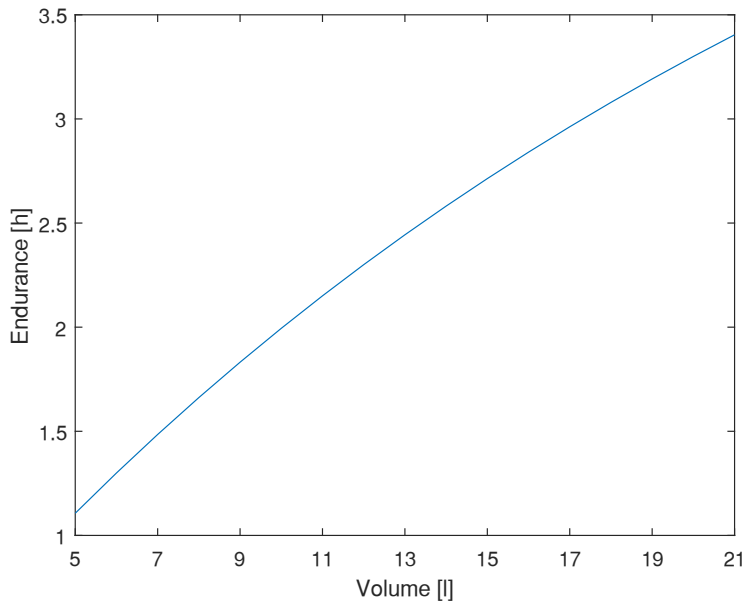


Figure 7-3: Estimated endurance for pressure vessels of varying size.

8 DISCUSSION

The main goal of this thesis was to implement a fuel cell system on an existing drone, namely the Camflight FX8HL. The work has primarily consisted of three parts:

- Investigation of technology for the components composing the propulsion system, with special focus on fuel cell and hydrogen storage technology
- Selection of concepts and components based on available technology and power requirements estimated by momentum theory
- Design of a composite overwrapped pressure vessel (COPV) with classical lamination theory (CLT)

The aim was to design a system of maximum 10 kg which provides 3 h flight time. To reach this goal the focus has been on selection of the best technology for the components composing the propulsion system and the most lightweight and efficient components. For a VTOL UAV of this size, which requires high power density, the most suitable solution is a PEMFC. The PEMFC is currently the most used fuel cell in portable applications, and thus has the most mature technology. Momentum theory was used to estimate the power requirements in hover, climb and forward flight, which showed that the fuel cell stack should be able to continuously deliver 2000 W when the efficiency of the motors and propellers are included. The power requirement is based on the power needed in forward flight, with about 10 % excess power to charge the battery. Often fuel cells are sized based on the power needed in hover, but as the Camflight will be mostly in forward flight during a normal mission with its primary payload, it was decided to use this power as a basis. The selected PEMFC from HES Energy systems, the Aeropak 2000, is currently the most lightweight system in the 2000 W-range, and it offers high efficiency as well of between 50 and 54 % based on LHV.

The Aeropak 2000 has maximum power output of 2500 W. The fuel cell is hybridized with a battery to take care of peak powers, and additional power requirements in hover and in climb. The hybridized system has maximum continuous power of 3840 W, which is relatively low. It is enough for the climb phase but restricts flight speeds during a mission. For missions with the Camflight's primary load, LIDAR, this is probably not an issue. But for other types of missions the current battery may be replaced with a larger battery which can provide higher continuous power. The system would then have higher specific power and lower specific energy. From this we can say that the size of the battery is mission dependent. The independent scaling of the power and energy storage is one of the great advantages with fuel cells.

Based on the available technology the best solution for the hydrogen storage was found to be gaseous hydrogen. As with the PEMFC, this solution has the most mature technology among the alternatives. Since the implementation of a fuel cell system on a VTOL UAV is new, the use of well-known technology seems like the best path to follow for a successful outcome. Among the types of pressure vessels, a composite overwrapped pressure vessel with HDPE liner (a type IV pressure vessel) was selected. This solution offers high specific energy, high reliability, and easy refueling of hydrogen which make the system readily available for missions. Classical lamination theory was used to do a comparison between spherical and cylindrical pressure vessels of the same sizes. The results showed that a cylindrical pressure vessel with length to diameter ratio of 3 is on average 18 % heavier than an equivalent spherical pressure vessel for capacities between 5 to 25 liters. Cylindrical pressure vessels have been seen as the best solution for hydrogen storage for UAVs since they are much easier to fit into the slender body of a fixed wing UAV. There are currently no COTS lightweight spherical pressure vessels suited for UAV applications. But for a VTOL UAV, a spherical pressure vessel seems like the best solution because of the potential weight savings, and because the aerodynamics are equal in all directions.

Preliminary design of a spherical type IV pressure vessel was done. The number of composite layers needed to withstand the internal pressure was calculated with CLT in MATLAB. Because of the

symmetric shape of the structure, and the symmetry which arise from cross-ply layup, two unidirectional layers had to be modeled as one cross-ply layer. The most challenging part was to find strength properties of a cross-ply laminate needed in the simulation. Eventually suitable strength properties were found for IM6/3501-6 carbon/epoxy cross-ply laminate. The strengths are based on experimental tests using cruciform specimens by Welsh et. al [60]. The available weight for the hydrogen storage allowed design of a 21 liter spherical pressure vessel. The designed pressure vessel reached a weight of 0.25 kg/L, which is impressive compared to COTS pressure vessels. Anyhow, this weight is dependent upon designing BOP components weighing less than 25 % of the total pressure vessel weight.

The amount of hydrogen that the pressure vessel can store was calculated by correction of the ideal gas law with the compressibility factor method to take into account the non-ideal behavior of hydrogen gas at high pressures. The 21 liter spherical pressure vessel can store 434 g hydrogen gas, which gives gravimetric capacity of 8.1 wt%. The endurance was estimated from the average power consumption and the available energy, which takes into account the energy loss in the compression process and the lower system efficiency of the Aeropak of 50 %. The estimated endurance is 3.2 hours at MTOW, which is 7x the endurance of the existing system using LiPo batteries. This is similar to the achievements of earlier work of implementing fuel cells on VTOL UAVs (see chapter 1). The results clearly demonstrate that replacing batteries with fuel cells for electric propulsion for a small VTOL UAV gives huge improvements in endurance, and hence is worth it considering the extra cost and more complicated work flow. The estimated flight time is in ideal conditions though, and will be somewhat less in real missions.

The proposed propulsion system came within the desired weight of maximum 10 kg and the goal of 3 h endurance was reached. In the future, the 3 h endurance will most likely be extended as the development of lightweight fuel cells and hydrogen storage continues. Furthermore, improvements can be done regarding optimization of the proposed system. It would be interesting to investigate the optimum sizing of the battery, fuel cell and hydrogen storage. This work has contributed to the knowledge of using fuel cells in VTOL UAVs as it provides all the formulas needed for preliminary design of a fuel cell – battery hybrid system, and it will be the basis for Nordic Unmanned's further work on fuel cell implementation.

Further work should include experimentally testing of the performance of the coaxial propellers, which is the largest uncertainty in the power calculations. If the power loss is higher than the 22 % considered in the calculations, an alternative design consisting of 6 separate propellers (hexacopter) should be evaluated. After the coaxial configuration performance has been settled, the proposed system should be bench tested as well as tested in real missions to validate the results. Regarding the spherical pressure vessel, further work should focus design of lightweight BOP components, which is crucial for a lightweight overall design. The weight savings the spherical design offers are very interesting, and further investigation should be done as a spherical pressure vessel seems like the ideal solution for hydrogen storage for a VTOL UAV. In the coming years we will most likely see many demonstrations of fuel cells systems in VTOL UAVs.

9 CONCLUSION

The goal of this work was to replace the batteries of an existing VTOL UAV with MTOW of 25 kg with a fuel cell – battery hybrid solution to increase the endurance. The outcome is a preliminary design of the entire propulsion system. The available technology was investigated, and the best solution for the hybrid fuel cell system was found to be a PEMFC hybridized with a LiPo battery, and energy storage in form of gaseous hydrogen. The proposed system weighs less than 10 kg and can provide 3.2 h flight time in ideal conditions, which is a 7-fold improvement compared to the current installed batteries. To reach this endurance, the most lightweight and efficient components available on the market was used. The estimated flight time is based on power consumption calculated from momentum theory, with incorporating the efficiencies of the fuel cell, motors and propellers. Based on an investigation of composite pressure vessels which showed that a cylindrical pressure vessel on average is 18 % heavier than a comparable spherical pressure vessel, the preliminary design of a spherical pressure vessel where done. The weight of the designed pressure vessel is 0.25 kg/L, but is dependent upon designing BOP components weighing less than 25 % of the total weight. A spherical pressure vessel seems ideal for a VTOL UAV regarding both the weight and the aerodynamics. The work has shown that a fuel cell hybrid system has the potential to multiply the endurance for VTOL UAVs, and is thus a very interesting path to follow to achieve extended missions.

10 REFERENCES

- [1] "EnergyOr shows off world's first fuel cell multirotor UAV," *Fuel Cells Bulletin*, vol. 2015, no. 4, pp. 5-6, 2015/04/01/ 2015.
- [2] "Horizon launches Hycopter fuel cell multirotor UAV," *Fuel Cells Bulletin*, vol. 2015, no. 6, p. 4, 2015/06/01/ 2015.
- [3] "Chinese UAV maker MMC flies hydrogen fuel cell drone for 4 h," *Fuel Cells Bulletin*, vol. 2016, no. 6, pp. 4-5, 2016/06/01/ 2016.
- [4] "Wirth Research unveils world's first VTOL drone, with HES power," *Fuel Cells Bulletin*, vol. 2017, no. 7, pp. 4-5, 2017/07/01/ 2017.
- [5] J. Gundlach, *Designing unmanned aircraft systems: a comprehensive approach*. American Institute of Aeronautics and Astronautics, 2012.
- [6] (2017). *FAA Aerospace Forecast*. Available: https://www.faa.gov/data_research/aviation/aerospace_forecasts/media/FY2017-37_FAA_Aerospace_Forecast.pdf
- [7] J. M. Seddon and S. Newman, *Basic helicopter aerodynamics*. John Wiley & Sons, 2011.
- [8] W. Johnson, *Rotorcraft aeromechanics*. Cambridge University Press, 2013.
- [9] G. J. Leishman, *Principles of helicopter aerodynamics with CD extra*. Cambridge university press, 2006.
- [10] Y. Lei, Y. Bai, Z. Xu, Q. Gao, and C. Zhao, "An experimental investigation on aerodynamic performance of a coaxial rotor system with different rotor spacing and wind speed," *Experimental Thermal and Fluid Science*, vol. 44, pp. 779-785, 2013/01/01/ 2013.
- [11] A. Bondyra, S. Gardecki, P. Gąsior, and W. Giernacki, "Performance of coaxial propulsion in design of multi-rotor UAVs," in *Challenges in Automation, Robotics and Measurement Techniques*: Springer, 2016, pp. 523-531.
- [12] I. Sharf *et al.*, "Ground effect experiments and model validation with Draganflyer X8 rotorcraft," in *Unmanned Aircraft Systems (ICUAS), 2014 International Conference on*, 2014, pp. 1158-1166: IEEE.
- [13] C. Simoes, "Optimizing a coaxial propulsion system to a quadcopter," Technical Report. <https://fenix.tecnico.ulisboa.pt/downloadFile/563345090412782/Resumo.pdf>2015.
- [14] D. Linden and T. B. Reddy, *Handbook of batteries*. McGraw-Hill, 2002.
- [15] C. Julien, A. Mauger, A. Vijh, and K. Zaghbi, *Lithium batteries: science and technology*. Springer, 2015.
- [16] O. Z. Sharaf and M. F. Orhan, "An overview of fuel cell technology: Fundamentals and applications," *Renewable and Sustainable Energy Reviews*, vol. 32, pp. 810-853, 2014.
- [17] R. O'hayre, S.-W. Cha, F. B. Prinz, and W. Colella, *Fuel cell fundamentals*. John Wiley & Sons, 2016.
- [18] F. Barbir, *PEM fuel cells: theory and practice*. Academic Press, 2012.
- [19] J. Larminie, A. Dicks, and M. S. McDonald, *Fuel cell systems explained*. J. Wiley Chichester, UK, 2003.
- [20] J. Sisco, P. Robinson, and P. Osenar, "New fuel cell technologies extend missions for vertical take-off and landing unmanned aerial vehicles," in *AUVSI XPONENTIAL 2017*, 2017.

- [21] A. Gong and D. Verstraete, "Fuel cell propulsion in small fixed-wing unmanned aerial vehicles: Current status and research needs," *International Journal of Hydrogen Energy*, vol. 42, no. 33, pp. 21311-21333, 2017/08/17/ 2017.
- [22] "University of Michigan students set new UAV record," in *Fuel Cell Today*, ed, 2008.
- [23] K. Kang, S. Park, S. O. Cho, K. Choi, and H. Ju, "Development of Lightweight 200-W Direct Methanol Fuel Cell System for Unmanned Aerial Vehicle Applications and Flight Demonstration," *Fuel Cells*, vol. 14, no. 5, pp. 694-700, 2014.
- [24] R. O. Stroman, M. W. Schuette, K. Swider-Lyons, J. A. Rodgers, and D. J. Edwards, "Liquid hydrogen fuel system design and demonstration in a small long endurance air vehicle," *International Journal of Hydrogen Energy*, vol. 39, no. 21, pp. 11279-11290, 2014/07/15/ 2014.
- [25] T. Bradley, B. A. Moffitt, D. Mavris, and D. E. Parekh, *APPLICATIONS – TRANSPORTATION / Aviation: Fuel Cells*. 2009, pp. 186-192.
- [26] S. T. Revankar and P. Majumdar, *Fuel cells: principles, design, and analysis*. CRC press, 2014.
- [27] C. Spiegel, *PEM fuel cell modeling and simulation using MATLAB*. Academic press, 2011.
- [28] Q. Cai, D. Brett, D. Browning, and N. Brandon, "A sizing-design methodology for hybrid fuel cell power systems and its application to an unmanned underwater vehicle," *Journal of Power Sources*, vol. 195, no. 19, pp. 6559-6569, 2010.
- [29] C. Red. (2014). *Pressure vessels for alternative fuels, 2014-2023*. Available: <https://www.compositesworld.com/articles/pressure-vessels-for-alternative-fuels-2014-2023>
- [30] K. Swider-Lyons, R. Stroman, G. Page, M. Schuette, J. Mackrell, and J. Rodgers, "Hydrogen Fuel Cell Propulsion for Long Endurance Small UAVs," in *AIAA Centennial of Naval Aviation Forum "100 Years of Achievement and Progress"*, 2011, p. 6975.
- [31] EnergyOR. (2016). *HPOD filling station*. Available: <http://www.energyor.com/products/detail/hpod>
- [32] *HES Energy Systems*. Available: <https://www.hes.sg/in-the-air>
- [33] H. Barthelemy, M. Weber, and F. Barbier, "Hydrogen storage: Recent improvements and industrial perspectives," *International Journal of Hydrogen Energy*, vol. 42, no. 11, pp. 7254-7262, 2017.
- [34] E. Okumus *et al.*, "Development of boron-based hydrogen and fuel cell system for small unmanned aerial vehicle," *International Journal of Hydrogen Energy*, vol. 42, no. 4, pp. 2691-2697, 2017/01/26/ 2017.
- [35] K. Hirose, *Handbook of hydrogen storage: new materials for future energy storage*. John Wiley & Sons, 2010.
- [36] J. O. Jensen, A. P. Vestbø, Q. Li, and N. Bjerrum, "The energy efficiency of onboard hydrogen storage," *Journal of Alloys and Compounds*, vol. 446, pp. 723-728, 2007.
- [37] A. Gong and D. Verstraete, "Role of battery in a hybrid electrical fuel cell UAV propulsion system," in *52nd Aerospace Sciences Meeting*, 2014.
- [38] D. Verstraete, K. Lehmkuehler, A. Gong, J. R. Harvey, G. Brian, and J. L. Palmer, "Characterisation of a hybrid, fuel-cell-based propulsion system for small unmanned aircraft," *Journal of power sources*, vol. 250, pp. 204-211, 2014.
- [39] A. Nishizawa, J. Kallo, O. Garrot, and J. Weiss-Ungethüm, "Fuel cell and Li-ion battery direct hybridization system for aircraft applications," *Journal of Power Sources*, vol. 222, pp. 294-300, 2013.

- [40] J. M. Stickel and M. Nagarajan, "Glass Fiber-Reinforced Composites: From Formulation to Application," *International Journal of Applied Glass Science*, vol. 3, no. 2, pp. 122-136, 2012.
- [41] D. M. Fryer and J. F. Harvey, "High pressure vessels," in *High Pressure Vessels*: Springer, 1998, pp. 1-10.
- [42] D. G. Pavlou, *Composite Materials in Piping Applications: Design, Analysis and Optimization of Subsea and Onshore Pipelines from FRP Materials*. DEStech Publications Incorporated, 2013.
- [43] R. F. Gibson, *Principles of composite material mechanics*. CRC press, 2016.
- [44] K. Lasn and A. T. Echtermeyer, "Safety approach for composite pressure vessels for road transport of hydrogen. Part 1: Acceptable probability of failure and hydrogen mass," *International Journal of Hydrogen Energy*, vol. 39, no. 26, pp. 14132-14141, 2014.
- [45] A. T. Echtermeyer and K. Lasn, "Safety approach for composite pressure vessels for road transport of hydrogen. Part 2: Safety factors and test requirements," *International Journal of Hydrogen Energy*, vol. 39, no. 26, pp. 14142-14152, 2014.
- [46] E. S. Barboza Neto, L. A. F. Coelho, M. M. d. C. Forte, S. C. Amico, and C. A. Ferreira, "Processing of a LLDPE/HDPE pressure vessel liner by rotomolding," *Materials Research*, vol. 17, no. 1, pp. 236-241, 2014.
- [47] B. R. Murray, S. B. Leen, C. O. Semprimoschnig, and C. M. Ó. Brádaigh, "Helium permeability of polymer materials as liners for composite overwrapped pressure vessels," *Journal of Applied Polymer Science*, vol. 133, no. 29, 2016.
- [48] T. Q. Hua, H.-S. Roh, and R. K. Ahluwalia, "Performance assessment of 700-bar compressed hydrogen storage for light duty fuel cell vehicles," *International Journal of Hydrogen Energy*, vol. 42, no. 40, pp. 25121-25129, 2017.
- [49] T. Hua *et al.*, "Technical assessment of compressed hydrogen storage tank systems for automotive applications," *International Journal of Hydrogen Energy*, vol. 36, no. 4, pp. 3037-3049, 2011.
- [50] T. A. Yersak *et al.*, "Predictive model for depressurization-induced blistering of type IV tank liners for hydrogen storage," *International Journal of Hydrogen Energy*, vol. 42, no. 48, pp. 28910-28917, 2017.
- [51] K. direct. *UAS MULTI-ROTOR BRUSHLESS MOTORS*. Available: <https://www.kdedirect.com/collections/uas-multi-rotor-brushless-motors>
- [52] T-motor. *Brushless motors U efficiency type*. Available: <http://store-en.tmotor.com/category.php?id=38>
- [53] A. C. Yunus and J. M. Cimbala, "Fluid mechanics fundamentals and applications," *International Edition, McGraw Hill Publication*, vol. 185201, 2006.
- [54] R. M. Jones, *Mechanics of composite materials*. CRC press, 2014.
- [55] D. Gay, S. V. Hoa, and S. W. Tsai, *Composite materials: design and applications*. CRC press, 2002.
- [56] J. C. Velosa, J. P. Nunes, P. Antunes, J. Silva, and A. Marques, "Development of a new generation of filament wound composite pressure cylinders," *Composites Science and Technology*, vol. 69, no. 9, pp. 1348-1353, 2009.
- [57] L. P. Kollár and G. S. Springer, *Mechanics of composite structures*. Cambridge university press, 2003.
- [58] I. M. Daniel, O. Ishai, I. M. Daniel, and I. Daniel, *Engineering mechanics of composite materials*. Oxford university press New York, 1994.
- [59] MMC. *H1- Fuel cell*. Available: <http://www.mmcuav.com/drones/h1-fuel-cell/>

- [60] J. S. Welsh and D. F. Adams, "An experimental investigation of the biaxial strength of IM6/3501-6 carbon/epoxy cross-ply laminates using cruciform specimens," *Composites Part A: Applied Science and Manufacturing*, vol. 33, no. 6, pp. 829-839, 2002.
- [61] S. Sapuan and I. M. Mujtaba, *Composite materials technology: neural network applications*. CRC Press, 2009.
- [62] T. Donato, A. Ficarella, L. Spedicato, A. Arista, and M. Ferraro, "A new approach to calculating endurance in electric flight and comparing fuel cells and batteries," *Applied energy*, vol. 187, pp. 807-819, 2017.

APPENDIX

APPENDIX A: MATLAB CODES

In this appendix, all the codes used for the calculations in the thesis are attached

A.1: Comparison of COTS MOTORS

```
clear all;clc;
```

```
%Test data 8218
```

```
t82=[1080 2120 3560 5160 6270 8840 11190]  
p82=[52 126 267 449 702 1004 1361]  
per82=[25 37.5 50 62.5 75.0 87.5 100]  
eff82=[20.77 16.83 13.33 11.49 9.93 8.8 8.22]
```

```
%test data 7215
```

```
t72=[1070 2170 3740 5460 7220 8980 11390]  
p72=[49 132 289 526 816 1204 1638]  
per72=[25 37.5 50 62.5 75.0 87.5 100]  
eff72=[21.84 16.44 12.94 10.38 8.85 7.46 6.95]
```

```
figure(1)  
plot(p82,t82)  
hold on
```

```
plot(p72,t72)
```

```
%test data U10
```

```
tU10=[1835 2164 2480 3042 4017 5045 6690]  
pU10=[121.6 153.6 185.6 246.4 364.8 505.6 755.2]  
perU10=[50 55 60 65 75 85 100]  
effU10=[15.09 14.10 13.36 12.35 11.01 9.98 8.86]
```

```
plot(pU10,tU10)
```

```
%test data U12
```

```
tU12=[2670 3175 3839 4341 5761 7169 9401]  
pU12=[212 272 360 424 640 840 1264]  
perU12=[50 55 60 65 75 85 100]  
effU12=[12.36 11.67 10.66 10.42 9.00 8.53 7.44]
```

```
plot(pU12,tU12)
```

```
xlabel('Power [w]')  
ylabel('Thrust [g]')  
legend('KDE 8218','KDE 7215','T-motor U10','T-motor U12')
```

```
%plot of thrust vs throttle  
figure(2)
```

```
plot(per82,t82)
hold on
plot(per72,t72)
plot(perU10,tU10)
plot(perU12,tU12)

x=20:100;
y=3125;
plot(x,y*ones(size(x)),'--k')
xlabel('Throttle %')
ylabel('Thrust [g]')
legend('KDE 8218','KDE 7215','T-motor U10','T-motor U12','Thrust required in hover')
```


A.2: Power in hover with KDE 7215 motors and 30.5" propellers

```
clear all;clc;
```

%% Weight

```
M=25 %Maximum takeoff weight (MTOW)
```

%% Propellers

```
np=8 %Number of propellers
```

```
di=30.5 %diameter in inches
```

```
r=(30.5*2.54*10^-2)/2 %radius in meters
```

%% KDE motor data

```
x=[0 49 132 289 526 816 1204 1638] %Power consumption
```

```
y=[0 1070 2170 3740 5460 7220 8980 11390] %Thrust generation
```

```
plot(x,y,'-o')
```

```
xlabel('Power input [w]')
```

```
ylabel('Thrust output [g]')
```

%% Power calculations according to momentum theory

```
rho=1.225 %Air density
```

```
%Required thrust per propeller
```

```
thp=M*1000/8 %in grams
```

```
thpn=thp*9.81*10^-3 %In newton
```

```
%Calculation of theoretical power per motor
```

```
P=((thpn)^(3/2))/sqrt(2*rho*pi*r^2)
```

%% Compared with KDE motor

```
%The graph of thrust vs. power from KDE motor data shows that each motor requires 223 W to generate 3125 g thrust
```

```
Pkde=223
```

```
%Efficiency of motor + propeller
```

```
n=P/Pkde
```

%% Total power requirements

```
P8=223*8
```

```
%According to literature on coaxial configuration, the power requirement is approximately 22 % larger compared to isolated propellers
```

```
Ptot=P8*1.22
```

A.3: Power in Vertical climb with KDE 7215 motors and 30.5" propellers

```
clear all;clc

m=25
n=0.71 %efficiency for motor + blades

%% Propellers
np=8 %Number of propellers
di=30.5 %diameter in inches
r=(30.5*2.54*10^-2)/2 %radius in meters

%% Thrust/Power calculations
rho=1.225 %Air density
%Required thrust per probeller
thp=m*1000/8 %in grams
T=thp*9.81*10^-3 %In newton

v0=sqrt(T/(2*rho*pi*r^2))
vc=0:0.1:20
vi=-(vc./2)+sqrt((vc./2).^2+v0^2)

% Ideal power
Pi=T.*vi %Induced power per motor
Pc=T.*vc %Climb power per motor
P=Pi+Pc %Total power per motor

%% Assume same efficiency as in hover and additional power
requirements of 22%
Pitot=Pi.*8*(1/n)*1.22 %Induced power
Pctot=Pc.*8*(1/n)*1.22 %Climb power
Ptot=Pitot+Pctot %Total power

plot(vc,Ptot)
hold on
plot(vc,Pitot)
hold on
plot(vc,Pctot)

xlabel('Climb speed [m/s]')
ylabel('Power requirements in climb [W]')
legend('Total power','Induced power','Climb power')
```

A.4: Estimation of drag Coefficient

```
clear all;clc;
%Cd is the drag coefficient for the different components
%A is the reference area

S=zeros(1,7)
%fuel cell
Af=0.2*0.12
Cd=2.1
S(1)=Af*Cd
%Platform
Ap=0.35*0.03
Cd=2.1
S(2)=Ap*Cd
%Lidar
Al=0.2*0.1
Cd=2.1
S(3)=Al*Cd
%4*Arms
Aa=4*0.36*0.03
Cd=0.9
S(4)=Aa*Cd
%4*legs
Ab=4*0.48*0.018
Cd=0.95
S(5)=Ab*Cd
%4*motor
Am=4*0.1*0.1
Cd=1.05
S(6)=Am*Cd
%Tank
At=pi*0.17^2
Cd=0.5
S(7)=At*Cd

drag_coeff=sum(S)
```

A.5: Power in horizontal flight with KDE 7215 motors and 30.5" propellers

clear all;clc;

%% Variables

f=0.2746 % Estimated drag coefficient

rho=1.225 % air density

V=6 % forward speed

%% Propellers

di=30.5 % diameter in inches

r=(30.5*2.54*10^-2)/2 % radius in meters

A=pi*r^2 % Propeller disc area

%% Drag force

D=0.5*rho*f*V^2/8

%% Gravitational force

W=25*9.81/8

%% angle

alpha=atan(D/W)

%% Needed thrust to overcome drag and gravity

T=sqrt(D^2+W^2)

%% Power calculations

syms vi % Create symbolic variable

% Solve for the induced velocity

s=solve(T == 2*rho*A*vi*sqrt(V^2 + 2*V*vi*sin(alpha) + vi^2), vi,'real',true)

vi=vpa(s) % The induced velocity. vpa uses variable-precision floating-point arithmetic (VPA) to evaluate each element of the symbolic input

Pp=T*V*sin(alpha) % Parasitic power

Pi=T*vi % Induced power

P=Pp+Pi % Total power per motor

PTOT=(P*8*1.22)/0.71 % Total power for the eight motors with the same efficiency as in hover and additional power requirement of 22%

A.6: Calculation of optimum winding angle

clear all

```

clc

%% Material properties
E1=134e9
E2=7e9
G12=4.2e9
v12=0.3
v21=v12*E2/E1

%% Material strength
s1t=1270e6
s1c=1130e6
s2t=42e6
s2c=141e6
s12=63e6
%% Other properties
N=40 %Number of layers(must be even) og i tillegg 4 +n*4
t=0.3e-3 %Layer thickness
p=30e6 %operating pressure Pa
r=170e-3 %radii of pressure vessel

%% Forces
Nx=(p*r)/2 %Loading in x direction [Pa*m]
Ny=(p*r)/2 %Loading in y direction [Pa*m]
txy=0
Mx=0
My=0
Mxy=0
F=[Nx; Ny; txy; Mx; My; Mxy]

tsaiwu1=zeros(1,91) %Create a vector for storage of values

for alpha=0:90 % Vary alpha between 0 and 90 degrees

%Generating z-vector containing the distances from the midplane to the layers
z=zeros(N+1,1)
for i=1:N+1
    if i<(N/2)+1
        z(i)=-((N/2)+i-1)*t

        elseif i>((N/2)+1)
            z(i)=(i-(N/2)-1)*t
        else z((N/2)+1)=0
        end
end

%Lamina stiffness matrix
%This is only based on material properties
Q11=E1/(1-v12*v21)
Q22=E2/(1-v12*v21)
Q12=(v21*E1)/(1-v12*v21)
Q66=G12

Q=[Q11 Q12 0;Q12 Q22 0;0 0 2*Q66]

```

```
% Transformed stiffness matrix
```

```
% +alpha layers
```

```
c=cosd(alpha)
```

```
s=sind(alpha)
```

```
q11=Q11*c^4+Q22*s^4+2*s^2*c^2*(Q12+2*Q66)
```

```
q12=(Q11+Q22-4*Q66)*s^2*c^2+Q12*(c^4+s^4)
```

```
q22=Q11*s^4+Q22*c^4+2*s^2*c^2*(Q12+2*Q66)
```

```
q16=(Q11-Q12-2*Q66)*c^3*s-(Q22-Q12-2*Q66)*c*s^3
```

```
q26=(Q11-Q12-2*Q66)*c*s^3-(Q22-Q12-2*Q66)*c^3*s
```

```
q66=(Q11+Q22-2*Q12-2*Q66)*s^2*c^2+Q66*(s^4+c^4)
```

```
q1=[q11 q12 q16; q12 q22 q26;q16 q26 q66]
```

```
% -alpha layers
```

```
c=cosd(-alpha)
```

```
s=sind(-alpha)
```

```
q11=Q11*c^4+Q22*s^4+2*s^2*c^2*(Q12+2*Q66)
```

```
q12=(Q11+Q22-4*Q66)*s^2*c^2+Q12*(c^4+s^4)
```

```
q22=Q11*s^4+Q22*c^4+2*s^2*c^2*(Q12+2*Q66)
```

```
q16=(Q11-Q12-2*Q66)*c^3*s-(Q22-Q12-2*Q66)*c*s^3
```

```
q26=(Q11-Q12-2*Q66)*c*s^3-(Q22-Q12-2*Q66)*c^3*s
```

```
q66=(Q11+Q22-2*Q12-2*Q66)*s^2*c^2+Q66*(s^4+c^4)
```

```
q2=[q11 q12 q16; q12 q22 q26;q16 q26 q66]
```

```
% Make a help vector which determines if the k'th layer is - alpha or
```

```
% +alpha degrees
```

```
xx=ones(1,N/2)
```

```
xx(2:2:end)=-xx(2:2:end)
```

```
xx=[fliplr(xx),xx]
```

```
% Extensional stiffness
```

```
A=zeros(3,3)
```

```
a=zeros(N,1)
```

```
for i=1:3
```

```
for j=1:3
```

```
    A(i,j)=(N/2)*q1(i,j)*t+(N/2)*q2(i,j)*t
```

```
end
```

```
end
```

```
% Coupling stiffness
```

```
% For symmetric laminates B=0
```

```
B=zeros(3,3)
```

```
zd=z.^2
```

```
a=zeros(N,1)
```

```
for i=1:3
```

```
for j=1:3
```

```
    for k=1:N
```

```

    if xx(k)>0
    a(k)=(1/2)*q1(i,j)*(zd(k+1)-zd(k))
    else
    a(k)=(1/2)*q2(i,j)*(zd(k+1)-zd(k))
    end
end
B(i,j)=sum(a)
end
end

```

%Bending stiffness

```
D=zeros(3,3)
```

```
zd=z.^3
```

```
a=zeros(N,1)
```

```
for i=1:3
```

```
for j=1:3
```

```
for k=1:N
```

```
    if xx(k)>0
```

```
    a(k)=(1/3)*q1(i,j)*(zd(k+1)-zd(k))
```

```
    else
```

```
    a(k)=(1/3)*q2(i,j)*(zd(k+1)-zd(k))
```

```
    end
```

```
end
```

```
D(i,j)=sum(a)
```

```
end
```

```
end
```

%Laminate Stiffness matrix

```
K=[[A] [B];[B] [D]]
```

%Compliance stiffness matrix

```
Kinv=inv(K)
```

%Midplane strains and curvatures

```
ek=Kinv*F
```

%Since curvatures vanish for symmetric problems, strains do not depend on the distance z from the midplane, and hence stresses do not depend on the distance z. ($\epsilon = \epsilon_0 + z\kappa$)

%Stresses along x,y

%For +alpha laminas

```
sigmaplus=q1*ek(1:3)
```

%For -alpha laminates

```
sigmaminus=q2*ek(1:3)
```

%Principal stresses in layers

```
c=cosd(alpha)
```

```
s=sind(alpha)
```

```
T1=[c^2 s^2 2*s*c;s^2 c^2 -2*s*c; -s*c s*c c^2-s^2]
```

```
c=cosd(-alpha)
```

```
s=sind(-alpha)
```

```
T2=[c^2 s^2 2*s*c;s^2 c^2 -2*s*c; -s*c s*c c^2-s^2]
```

```

ps1=T1*sigmaplus %Layers with positive alpha
ps2=T2*sigmininus %Layers with negative alpha

%Tsai-Wu failure criterion
f11=1/(s1t*s1c)
f22=1/(s2t*s2c)
f1=(1/s1t)-(1/s1c)
f2=(1/s2t)-(1/s2c)
f66=1/s1t^2

%Tsai-wu value for positive alpha
tsaiwu1(alpha+1)=f11*(ps1(1))^2+f22*(ps1(2))^2+f66*(ps1(3))^2+f1*ps1(1)+f2*ps1(2)-
sqrt(f11*f22)*ps1(1)*ps1(2)
%Tsai-wu value for negative alpha
tsaiwu2=f11*(ps2(1))^2+f22*(ps2(2))^2+f66*(ps2(3))^2+f1*ps2(1)+f2*ps2(2)-
sqrt(f11*f22)*ps2(1)*ps2(2)

end

alpha=0:90;
plot(alpha,tsaiwu1)
xlabel('Ply orientation [degrees]')
ylabel('Tsai-Wu failure citerion')

```


A.7: Comparison of spherical and cylindrical pressure vessel

```
clear all;clc;
%% SPHERE
% Create storage vectors
volume_sphere=zeros(21,1)
radius_sphere=zeros(21,1)
tsai_sphere=zeros(21,1)
nlayers_sphere=zeros(21,1)
for l=5:25
V=l*0.001 % Volume
r=(nthroot((3*V)/(4*pi),3))+0.002 % Radius

volume_sphere(l-4)=V
radius_sphere(l-4)=r

% Elastic properties
E1=134e9
E2=7e9
G12=4.2e9
v12=0.25
v21=v12*E2/E1

N=2 % Starting number of layers
t=2*0.13e-3 % Thicknees of layer
SF=2.35 % Safety factor
p=30e6 % operating pressure Pa

% Forces per unit length
Nx=(p*r)/2 % Loading in x direction [Pa*m]
Ny=(p*r)/2
txy=0
Mx=0
My=0
Mxy=0
F=[Nx; Ny; txy; Mx; My; Mxy] % Force vector

alpha=45 % Winding angle

Q11=E1/(1-v12*v21)
Q22=E2/(1-v12*v21)
Q12=(v21*E1)/(1-v12*v21)
Q66=G12

Q=[Q11 Q12 0;Q12 Q22 0;0 0 2*Q66]

c=cosd(alpha)
s=sind(alpha)

q11=Q11*c^4+Q22*s^4+2*s^2*c^2*(Q12+2*Q66)
q12=(Q11+Q22-4*Q66)*s^2*c^2+Q12*(c^4+s^4)
q22=Q11*s^4+Q22*c^4+2*s^2*c^2*(Q12+2*Q66)
q16=(Q11-Q12-2*Q66)*c^3*s-(Q22-Q12-2*Q66)*c*s^3
q26=(Q11-Q12-2*Q66)*c*s^3-(Q22-Q12-2*Q66)*c^3*s
q66=(Q11+Q22-2*Q12-2*Q66)*s^2*c^2+Q66*(s^4+c^4)
```

```
q1=[q11 q12 q16; q12 q22 q26;q16 q26 q66]
```

```
c=cosd(-alpha)
```

```
s=sind(-alpha)
```

```
q11=Q11*c^4+Q22*s^4+2*s^2*c^2*(Q12+2*Q66)
```

```
q12=(Q11+Q22-4*Q66)*s^2*c^2+Q12*(c^4+s^4)
```

```
q22=Q11*s^4+Q22*c^4+2*s^2*c^2*(Q12+2*Q66)
```

```
q16=(Q11-Q12-2*Q66)*c^3*s-(Q22-Q12-2*Q66)*c*s^3
```

```
q26=(Q11-Q12-2*Q66)*c*s^3-(Q22-Q12-2*Q66)*c^3*s
```

```
q66=(Q11+Q22-2*Q12-2*Q66)*s^2*c^2+Q66*(s^4+c^4)
```

```
q2=[q11 q12 q16; q12 q22 q26;q16 q26 q66]
```

```
%Crossply layer stiffness matrix
```

```
q=(1/2)*(q1+q2)
```

```
tsaiwu1=2
```

```
while tsaiwu1>1
```

```
N=N+2
```

```
z=zeros(N+1,1)
```

```
for i=1:N+1
```

```
if i<(N/2)+1
```

```
z(i)=(-(N/2)+i-1)*t
```

```
elseif i>(N/2)+1
```

```
z(i)=(i-(N/2)-1)*t
```

```
else z((N/2)+1)=0
```

```
end
```

```
end
```

```
%% Extensional stiffness A
```

```
A=zeros(3,3)
```

```
a=zeros(N,1)
```

```
for i=1:3
```

```
for j=1:3
```

```
for k=1:N
```

```
a(k)=q(i,j)*(z(k+1)-z(k))
```

```
end
```

```
A(i,j)=sum(a)
```

```
end
```

```
end
```

```
%% Coupling stiffness B
```

```
B=zeros(3,3)
```

```
zb=z.^2
```

```
a=zeros(N,1)
```

```

for i=1:3
  for j=1:3
    for k=1:N

      a(k)=(1/2)*q(i,j)*(zb(k+1)-zb(k))

    end
    B(i,j)=sum(a)
  end
end

%% Bending stiffness D

D=zeros(3,3)
zd=z.^3
a=zeros(N,1)

for i=1:3
  for j=1:3
    for k=1:N

      a(k)=(1/3)*q(i,j)*(zd(k+1)-zd(k))

    end
    D(i,j)=sum(a)
  end
end

%% Laminata stiffness matrix

K=[[A] [B];[B] [D]]
Kinv=inv(K)

%% Strain
ek=Kinv*F

%% Stress in global coordinates
sigma=q*ek(1:3)

%% Stress in principal coordinates
c=cosd(alpha)
s=sind(alpha)
T1=[c^2 s^2 2*s*c;s^2 c^2 -2*s*c; -s*c s*c c^2-s^2]
c=cosd(-alpha)
s=sind(-alpha)
T2=[c^2 s^2 2*s*c;s^2 c^2 -2*s*c; -s*c s*c c^2-s^2]
%%Principle stresses
ps1=T1*sigma
ps2=T2*sigma
%Strengths

```

```

s1t=425e6
s1c=595e6
s2t=425e6
s2c=595e6
s12=63e6

%Tsai_wu
f11=1/(s1t*s1c)
f22=1/(s2t*s2c)
f1=(1/s1t)-(1/s1c)
f2=(1/s2t)-(1/s2c)
f66=1/s1t^2

%Positive alpha
tsaiwu1=SF*(f11*(ps1(1))^2+f22*(ps1(2))^2+f66*(ps1(3))^2+f1*ps1(1)+f2*ps1(2)-
sqrt(f11*f22)*ps1(1)*ps1(2))

end
tsai_sphere(1-4)=tsaiwu1
nlayers_sphere(1-4)=N

end

%% CYLINDER
%Create storage vectors
volume_cyl=zeros(21,1)
radius_cyl=zeros(21,1)
tsai_cyl=zeros(21,1)
nlayers_cyl=zeros(21,1)
for l=5:25
V=l*0.001 % Volume in liters
r=(nthroot((3*V)/(16*pi),3))+0.002% Radius

volume_cyl(l-4)=V
radius_cyl(l-4)=r

%% Material properties
E1=134e9
E2=7e9
G12=4.2e9
v12=0.25
v21=v12*E2/E1

%% Material strength
s1t=1270e6
s1c=1130e6
s2t=42e6
s2c=141e6
s12=63e6
%% Other properies
N=4%Number of layers(must be even and 4+4*n)

```

```

t=0.13e-3 %Thickness of layer
alpha=50 %Angle
SF=2.35 %Safety factor

%Forces in cylinder
p=30e6 %operating pressure Pa
%radii of cylinder
Nx=(p*r)/2 %Loading in x direction [Pa*m]
Ny=p*r
txy=0
Mx=0
My=0
Mxy=0
F=[Nx; Ny; txy; Mx; My; Mxy] %Force vector

```

```

%% Lamina stiffness matrix
%This is only based on material properties
Q11=E1/(1-v12*v21)
Q22=E2/(1-v12*v21)
Q12=(v21*E1)/(1-v12*v21)
Q66=G12

```

```

Q=[Q11 Q12 0;Q12 Q22 0;0 0 2*Q66]

```

```

%% Transformed stiffness matrix
%+alpha degrees
c=cosd(alpha)
s=sind(alpha)

```

```

q11=Q11*c^4+Q22*s^4+2*s^2*c^2*(Q12+2*Q66)
q12=(Q11+Q22-4*Q66)*s^2*c^2+Q12*(c^4+s^4)
q22=Q11*s^4+Q22*c^4+2*s^2*c^2*(Q12+2*Q66)
q16=(Q11-Q12-2*Q66)*c^3*s-(Q22-Q12-2*Q66)*c*s^3
q26=(Q11-Q12-2*Q66)*c*s^3-(Q22-Q12-2*Q66)*c^3*s
q66=(Q11+Q22-2*Q12-2*Q66)*s^2*c^2+Q66*(s^4+c^4)

```

```

q1=[q11 q12 q16; q12 q22 q26;q16 q26 q66]

```

```

%-alpha degrees
c=cosd(-alpha)
s=sind(-alpha)

```

```

q11=Q11*c^4+Q22*s^4+2*s^2*c^2*(Q12+2*Q66)
q12=(Q11+Q22-4*Q66)*s^2*c^2+Q12*(c^4+s^4)
q22=Q11*s^4+Q22*c^4+2*s^2*c^2*(Q12+2*Q66)
q16=(Q11-Q12-2*Q66)*c^3*s-(Q22-Q12-2*Q66)*c*s^3
q26=(Q11-Q12-2*Q66)*c*s^3-(Q22-Q12-2*Q66)*c^3*s
q66=(Q11+Q22-2*Q12-2*Q66)*s^2*c^2+Q66*(s^4+c^4)

```

```

q2=[q11 q12 q16; q12 q22 q26;q16 q26 q66]

```

```

tsaiwu1=2

```

```

while tsaiwu1>1
N=N+2

%% Generating z-vector
z=zeros(N+1,1)
for i=1:N+1
    if i<(N/2)+1
        z(i)=-((N/2)+i-1)*t

    elseif i>((N/2)+1)
        z(i)=(i-(N/2)-1)*t
    else z((N/2)+1)=0
    end

end

%% Extensional stiffness
A=zeros(3,3)
a=zeros(N,1)

for i=1:3
    for j=1:3
        A(i,j)=(N/2)*q1(i,j)*t+(N/2)*q2(i,j)*t
    end
end

%% Lager en hjelpevektor som bestemmer om det k'te laget er - alpha eller +
%alpha

xx=ones(1,N/2)
xx(2:2:end)=-xx(2:2:end)
xx=[fliplr(xx),xx]

%% Coupling stiffness
% For symmetric laminates B=0
B=zeros(3,3)
zd=z.^2
a=zeros(N,1)

for i=1:3
    for j=1:3
        for k=1:N

            if xx(k)>0
                a(k)=(1/2)*q1(i,j)*(zd(k+1)-zd(k))
            else
                a(k)=(1/2)*q2(i,j)*(zd(k+1)-zd(k))
            end
        end
        B(i,j)=sum(a)
    end
end

```

```

end
end

%% Bending stiffness
D=zeros(3,3)
zd=z.^3
a=zeros(N,1)

for i=1:3
    for j=1:3
        for k=1:N

            if xx(k)>0
                a(k)=(1/3)*q1(i,j)*(zd(k+1)-zd(k))
            else
                a(k)=(1/3)*q2(i,j)*(zd(k+1)-zd(k))
            end
        end
        D(i,j)=sum(a)
    end
end

%% Laminate Stiffness matrix
K=[[A] [B];[B] [D]]

%% Compliance stiffness matrix

Kinv=inv(K)
%% Midplane strains and curvatures

ek=Kinv*F

%% Stresses in along x,y in plies
%%For +alpha laminas
sigmaplus=q1*ek(1:3)
%%For -alpha laminates
sigmaminus=q2*ek(1:3)

%% Principal stresses
%% %% %% trenger to transformasjonematriser!!!!!!!!!!!!!!!!!!!!!!T1 T2
c=cosd(alpha)
s=sind(alpha)
T1=[c^2 s^2 2*s*c;s^2 c^2 -2*s*c; -s*c s*c c^2-s^2]
c=cosd(-alpha)
s=sind(-alpha)
T2=[c^2 s^2 2*s*c;s^2 c^2 -2*s*c; -s*c s*c c^2-s^2]
%% In layers
ps1=T1*sigmaplus
ps2=T2*sigmaminus

%% Tsai-Wu failure criterion
f11=1/(s1t*s1c)

```

```

f22=1/(s2t*s2c)
f1=(1/s1t)-(1/s1c)
f2=(1/s2t)-(1/s2c)
f66=1/s1t^2

%Positive alpha
tsaiwu1=SF*(f11*(ps1(1))^2+f22*(ps1(2))^2+f66*(ps1(3))^2+f1*ps1(1)+f2*ps1(2)-
sqrt(f11*f22)*ps1(1)*ps1(2))
%Negative alpha
tsaiwu2=SF*(f11*(ps2(1))^2+f22*(ps2(2))^2+f66*(ps2(3))^2+f1*ps2(1)+f2*ps2(2)-
sqrt(f11*f22)*ps2(1)*ps2(2))

end
tsai_cyl(l-4)=tsaiwu1
nlayers_cyl(l-4)=N

end

%% Comparison

%% SPHERE
%Composite overwrap
r0=radius_sphere
h=nlayers_sphere*2*0.13e-3
r1=r0+h

V1=(4/3)*pi*r1.^3
V0=(4/3)*pi*r0.^3

Vcomp_sphere=(V1-V0)*1000000

%Liner
r1=radius_sphere
t=2e-3
r0=r1-t

V1=(4/3)*pi*r1.^3
V0=(4/3)*pi*r0.^3

Vliner_sphere=(V1-V0)*1000000

%% Cylinder
%Composite overwrap
r0=radius_cyl
h=nlayers_cyl*0.13e-3
r1=r0+h
V1=(16/3)*pi*r1.^3

V0=(16/3)*pi*r0.^3

Vcomp_cyl=(V1-V0)*1000000

%liner

```



```

r1=radius_cyl
t=2e-3
r0=r1-t
V1=(16/3)*pi*r1.^3

V0=(16/3)*pi*r0.^3

Vliner_cyl=(V1-V0)*1000000

%% Mass calculations
rho_c=1.530
rho_hdpe=0.94

mc_sphere=rho_c*Vcomp_sphere
mc_cyl=rho_c*Vcomp_cyl

mlin_sphere=rho_hdpe*Vliner_sphere
mlin_cyl=rho_hdpe*Vliner_cyl

Msphere=mc_sphere+mlin_sphere

Mcyl=mc_cyl+mlin_cyl

figure(1)
liter=5:25
scatter(liter,Msphere)

xlabel=('Pressure vessel volume [liter]')
ylabel=('Pressure vessel weight[gram]')
hold on
scatter(liter,Mcyl)

lsline
legend('Spherical','Cylindrical','Trendline','Trendline')

figure(2)
R=Mcyl./Msphere
scatter(liter,R,'O')

hold on

mu = mean(R);

line([5 25],[mu mu],'LineWidth',2)

lsline

legend('R','Mean','Trendline')

```

A.8: Calculation of spherical pressure vessel

```
clear all;clc;
```

```
N=2 %Initial number of layers  
t=2*0.1335e-3 %Layer thickness  
SF=1.5 %Safety factor/Scale factor  
alpha=45 %Winding angle  
liner=2e-3 %Liner thickness  
l=21 %Internal water capacity  
p=30e6 %operating pressure Pa  
rho_c=1.530%Carbon/Epoxy density  
rho_hdpe=0.94%HDPE density
```

```
% Volume and radius
```

```
V=l*0.001  
r=(nthroot((3*V)/(4*pi),3))+liner
```

```
%Elastic properties
```

```
E1=157e9  
E2=9e9  
G12=5.7e9  
v12=0.3  
v21=v12*E2/E1
```

```
Nx=(p*r)/2 %Loading in x direction [Pa*m]
```

```
Ny=(p*r)/2
```

```
txy=0
```

```
Mx=0
```

```
My=0
```

```
Mxy=0
```

```
F=[Nx; Ny; txy; Mx; My; Mxy] %Force vector
```

```
Q11=E1/(1-v12*v21)
```

```
Q22=E2/(1-v12*v21)
```

```
Q12=(v21*E1)/(1-v12*v21)
```

```
Q66=G12
```

```
Q=[Q11 Q12 0;Q12 Q22 0;0 0 2*Q66]
```

```
c=cosd(alpha)
```

```
s=sind(alpha)
```

```
q11=Q11*c^4+Q22*s^4+2*s^2*c^2*(Q12+2*Q66)
```

```
q12=(Q11+Q22-4*Q66)*s^2*c^2+Q12*(c^4+s^4)
```

```
q22=Q11*s^4+Q22*c^4+2*s^2*c^2*(Q12+2*Q66)
```

```
q16=(Q11-Q12-2*Q66)*c^3*s-(Q22-Q12-2*Q66)*c*s^3
```

```
q26=(Q11-Q12-2*Q66)*c*s^3-(Q22-Q12-2*Q66)*c^3*s
```

```
q66=(Q11+Q22-2*Q12-2*Q66)*s^2*c^2+Q66*(s^4+c^4)
```

```
q1=[q11 q12 q16; q12 q22 q26;q16 q26 q66]
```

```

c=cosd(-alpha)
s=sind(-alpha)

q11=Q11*c^4+Q22*s^4+2*s^2*c^2*(Q12+2*Q66)
q12=(Q11+Q22-4*Q66)*s^2*c^2+Q12*(c^4+s^4)
q22=Q11*s^4+Q22*c^4+2*s^2*c^2*(Q12+2*Q66)
q16=(Q11-Q12-2*Q66)*c^3*s-(Q22-Q12-2*Q66)*c*s^3
q26=(Q11-Q12-2*Q66)*c*s^3-(Q22-Q12-2*Q66)*c^3*s
q66=(Q11+Q22-2*Q12-2*Q66)*s^2*c^2+Q66*(s^4+c^4)

```

```

q2=[q11 q12 q16; q12 q22 q26;q16 q26 q66]

```

```

%Crossply layer stiffness matrix

```

```

q=(1/2)*(q1+q2)

```

```

tsaiwu1=2
while tsaiwu1>1

```

```

N=N+2

```

```

z=zeros(N+1,1)

```

```

for i=1:N+1

```

```

    if i<=(N/2)+1

```

```

        z(i)=-((N/2)+i-1)*t

```

```

    elseif i>((N/2)+1)

```

```

        z(i)=(i-(N/2)-1)*t

```

```

    else z((N/2)+1)=0

```

```

    end

```

```

end

```

```

%% Extensional stiffness A

```

```

A=zeros(3,3)

```

```

a=zeros(N,1)

```

```

for i=1:3

```

```

    for j=1:3

```

```

        for k=1:N

```

```

            a(k)=q(i,j)*(z(k+1)-z(k))

```

```

        end

```

```

        A(i,j)=sum(a)

```

```

    end

```

```

end

```

```

%% Coupling stiffness B

```

```

B=zeros(3,3)

```

```

zb=z.^2

```

```
a=zeros(N,1)
```

```
for i=1:3  
for j=1:3  
for k=1:N
```

```
    a(k)=(1/2)*q(i,j)*(zb(k+1)-zb(k))
```

```
    end  
    B(i,j)=sum(a)  
end  
end
```

```
%% Bending stiffness D
```

```
D=zeros(3,3)  
zd=z.^3  
a=zeros(N,1)
```

```
for i=1:3  
for j=1:3  
for k=1:N
```

```
    a(k)=(1/3)*q(i,j)*(zd(k+1)-zd(k))
```

```
    end  
    D(i,j)=sum(a)  
end  
end
```

```
%% Laminate stiffness matrix
```

```
K=[[A] [B];[B] [D]]  
Kinv=inv(K)
```

```
%% Strain  
ek=Kinv*F
```

```
%% Stress in global coordinates  
sigma=q*ek(1:3)
```

```
%% Stress in principal coordinates
```

```
c=cosd(45)  
s=sind(45)  
T1=[c^2 s^2 2*s*c;s^2 c^2 -2*s*c; -s*c s*c c^2-s^2]  
c=cosd(-alpha)  
s=sind(-alpha)  
T2=[c^2 s^2 2*s*c;s^2 c^2 -2*s*c; -s*c s*c c^2-s^2]  
%%Principle stresses  
ps1=T1*sigma  
ps2=T2*sigma
```

```
%STRENGTHS
```

```
s1t=600e6  
s1c=530e6  
s2t=600e6  
s2c=530e6  
s12=40e6
```

```
f11=1/(s1t*s1c)  
f22=1/(s2t*s2c)  
f1=(1/s1t)-(1/s1c)  
f2=(1/s2t)-(1/s2c)  
f66=1/s1t^2
```

```
%Positive alpha
```

```
tsaiwu1=SF*(f11*(ps1(1))^2+f22*(ps1(2))^2+f66*(ps1(3))^2+f1*ps1(1)+f2*ps1(2)-  
sqrt(f11*f22)*ps1(1)*ps1(2))
```

```
end
```

```
tsai_sphere=tsaiwu1  
nlayers_sphere=N
```

```
%% Weight calculations
```

```
%Composite overwrap
```

```
r0=r %Inner radius
```

```
h=nlayers_sphere*2*0.13e-3
```

```
r1=r0+h %Outer radius
```

```
V1=(4/3)*pi*r1.^3
```

```
V0=(4/3)*pi*r0.^3
```

```
Vcomp=(V1-V0)*1000000
```

```
%Liner
```

```
r1=r %Outer radius
```

```
r0=r1-liner %Inner radius
```

```
V1=(4/3)*pi*r1.^3
```

```
V0=(4/3)*pi*r0.^3
```

```
Vliner=(V1-V0)*1000000
```

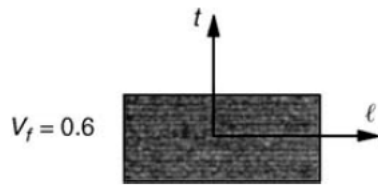
```
mc=rho_c*Vcomp
```

```
m1in=rho_hdpe*Vliner
```

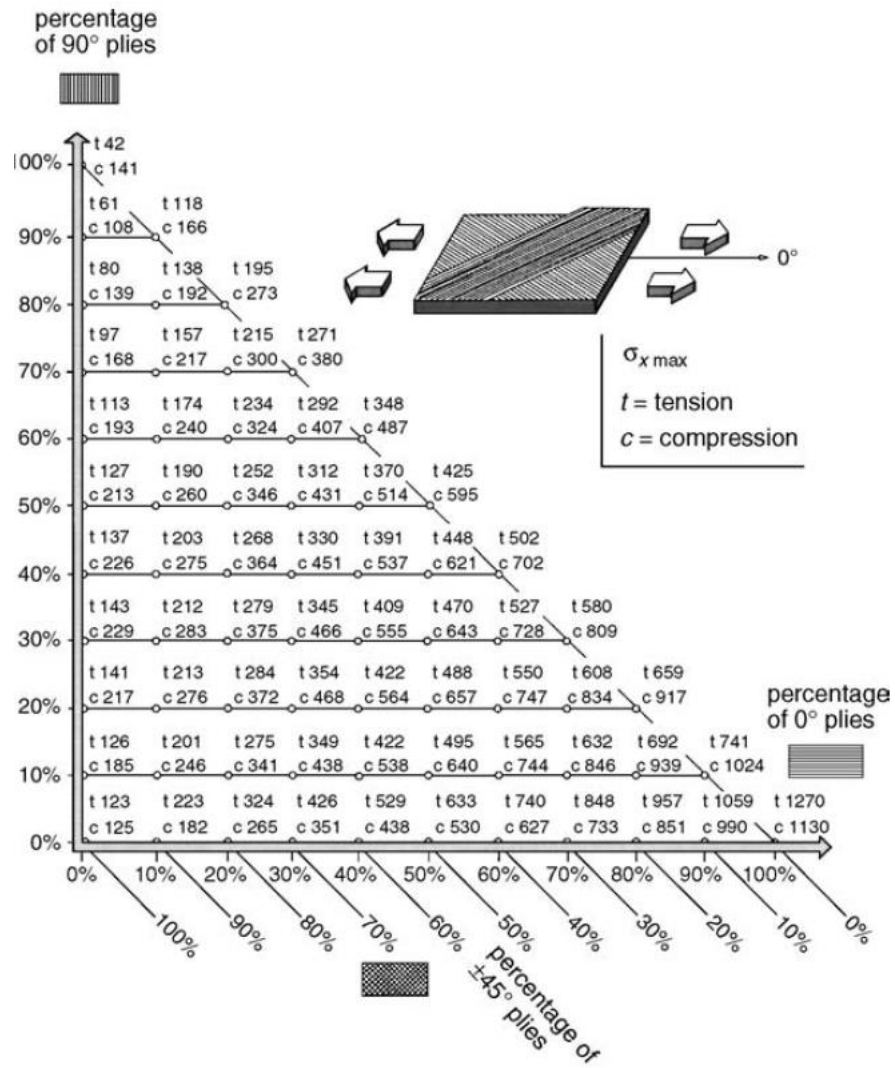
```
Mtot=mc+m1in %Total weight
```

APPENDIX B: LAMINA PROPERTIES AND STRENGTHS

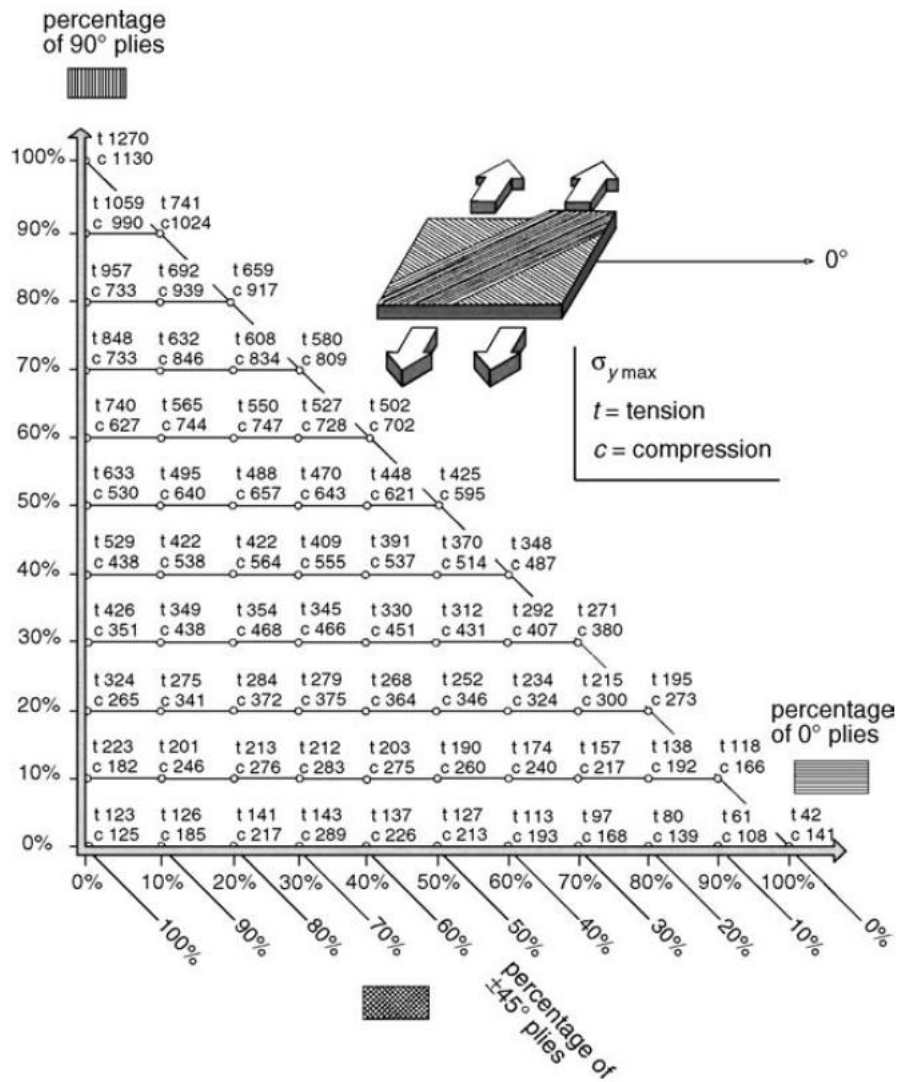
The properties are from the book Composite materials: design and applications ref. [55]



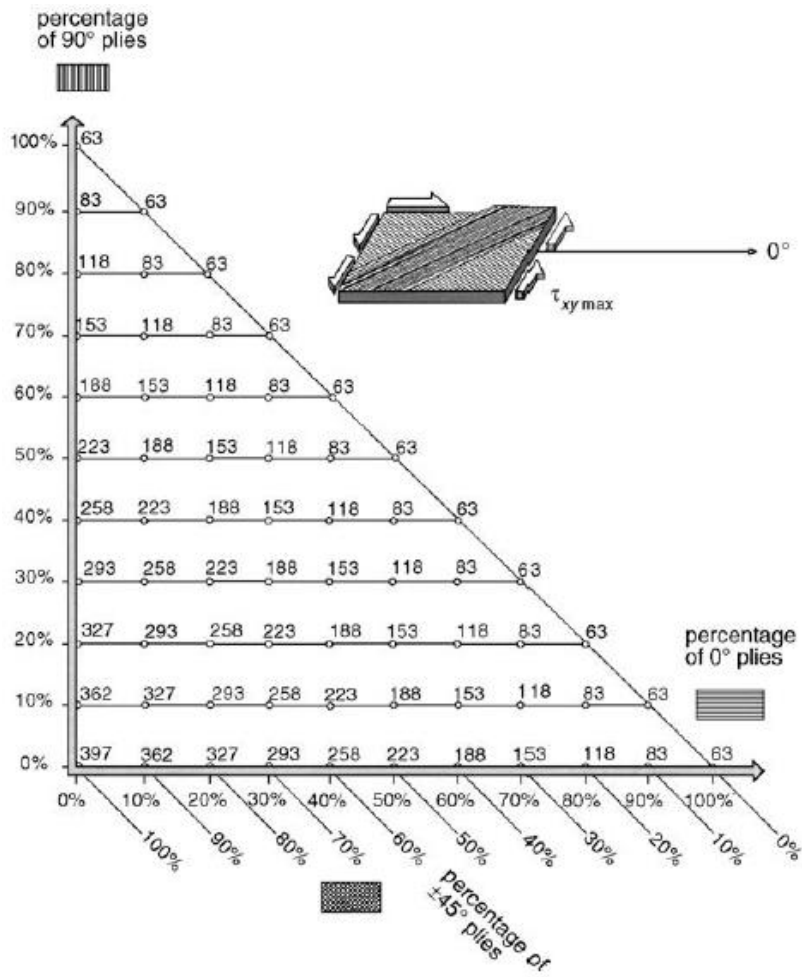
	<i>Carbon/epoxy</i>
Specific mass (kg/m^3)	1530
Longitudinal tensile fracture strength (MPa)	1270
Longitudinal compressive fracture strength (MPa)	1130
Transverse tensile fracture strength (MPa)	42
Transverse compressive fracture strength (MPa)	141
In plane shear strength (MPa)	63
Interlaminar shear strength (MPa)	90
Longitudinal elastic modulus E_l (MPa)	134,000
Transverse elastic modulus E_t (MPa)	7000
Shear modulus $G_{\ell t}$ (MPa)	4200
Poisson ratio $\nu_{\ell t}$	0.25
Longitudinal coefficient of thermal expansion at 20°C α_l ($^\circ\text{C}^{-1}$)	-0.12×10^{-5}
Transverse coefficient of thermal expansion at 20°C α_t ($^\circ\text{C}^{-1}$)	3.4×10^{-5}



Maximum stress $\sigma_{x \max}$ (MPa) as a function of the layer percentages in the directions 0° , $90^\circ + 45^\circ$, -45° . Volume fraction of fibers $V_f=0.6$. Layer thickness $t=0.13$



Maximum stress $\sigma_{y \max}$ (MPa) as a function of the layer percentages in the directions 0° , 90° , $+45^\circ$, -45° . Volume fraction of fibers $V_f=0.6$. Layer thickness $t=0.13$



Maximum shear stress $\tau_{xy \max}$ (MPa) as a function of the layer percentages in the directions 0° , $90^\circ + 45^\circ$, -45° . Volume fraction of fibers $V_f=0.6$. Layer thickness $t=0.13$

22	52	13,5	9392	0,97	72	9,36	10876	0,99
23	52	13,5	9661	0,99	74	9,62	11486	0,97
24	54	14,0	10306	0,96	74	9,62	11799	0,99
25	54	14,0	10577	0,98	76	9,88	12425	0,97
Mean				0,97				0,98

APPENDIX D: CONSTANTS USED IN CALCULATIONS

Universal gas constant, R 8.314 J/molK

Faradays constant, F 96485 C/mol

Properties of hydrogen gas (H₂)

The properties are at STP

Molar mass 2.016 kg/kmol
 Enthalpy of reaction HHV 285.8 kJ/mol H₂
 Enthalpy of reaction LHV 241.8 kJ/mol H₂
 Gibbs free energy HHV 237.2 kJ/mol H₂
 Gibbs free energy LHV 228.5 kJ/mol H₂